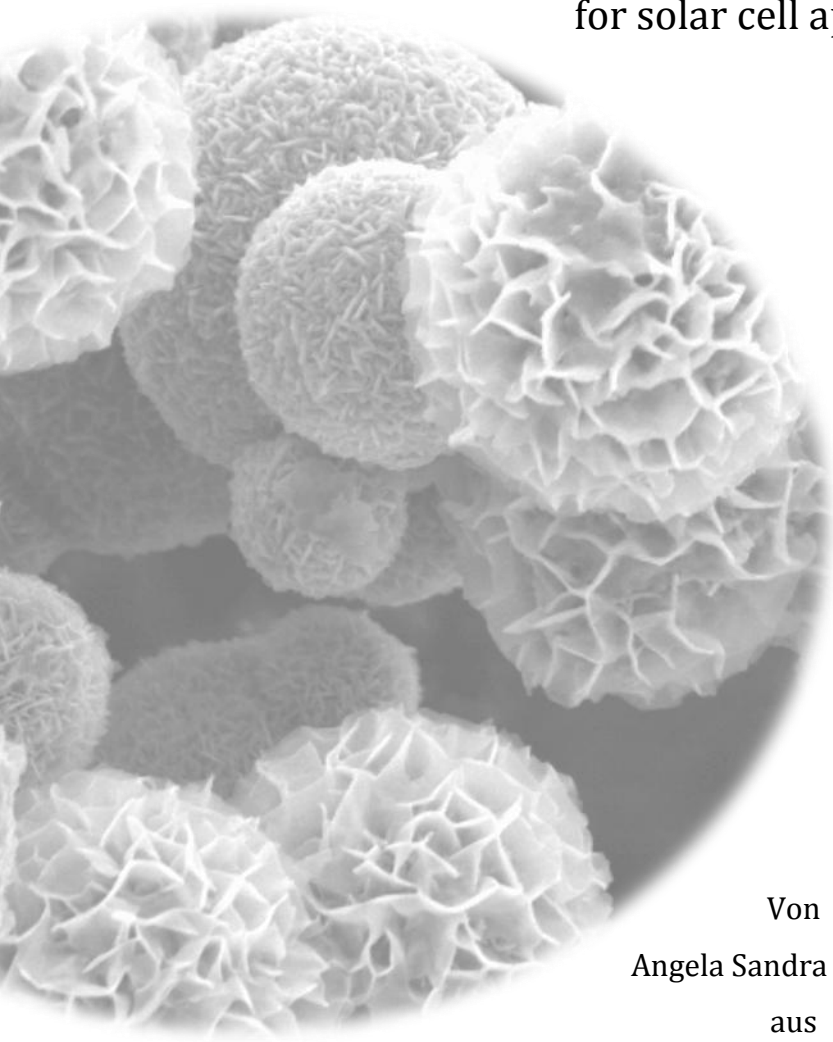


Dissertation zur Erlangung des Doktorgrades
der Fakultät für Chemie und Pharmazie
der Ludwig-Maximilians-Universität München

Synthesis and characterization of nanostructured
copperindiumdisulfide and titaniumdioxide thin films
for solar cell application



Von
Angela Sandra Wochnik
aus
Germering
2012



Erklärung

Diese Dissertation wurde in Sinne von § 7 der Promotionsordnung vom 28. November 2011 von Frau Professor Dr. Christina Scheu von der Fakultät für Chemie und Pharmazie betreut.

Ehrenwörtliche Versicherung

Diese Dissertation wurde selbständig, ohne unerlaubte Hilfe erarbeitet.

München, den

.....

(Unterschrift des Autors)

Dissertation eingereicht am 11.09.2012

1. Gutachter: Prof. Dr. Christina Scheu

2. Gutachter: Prof. Dr. Thomas Bein

Mündliche Prüfung am 30.10.2012

Table of contents

Table of contents	I
List of abbreviations.....	V
List of symbols.....	VII
List of figures.....	IX
List of tables.....	XIII
1 Introduction.....	1
1.1 Aim of the thesis.....	4
1.2 Chapter references	6
2 Theoretical background	7
2.1 Solar cells	7
2.1.1 Solar cell assembly and function.....	7
2.1.2 Solar cell types.....	9
2.2 Materials.....	12
2.2.1 Copperindiumdisulfide	12
2.2.2 Titaniumdioxide	15
2.2.3 Coppersulfide.....	17
2.2.4 Indium(III)sulfide.....	19
2.3 Chapter references	22
3 Synthesis and characterization methods.....	25
3.1 Solvothermal synthesis.....	25
3.2 Sol-gel method	27

Table of contents

3.3	X-ray diffraction.....	28
3.4	UV-Vis spectroscopy	30
3.5	Inductively coupled plasma atomic emission spectrometry	31
3.6	Electron microscopy	32
3.6.1	Scanning electron microscopy	34
3.6.2	Focused ion beam microscopy.....	35
3.6.3	Transmission electron microscopy.....	36
3.7	Energy dispersive X-ray spectroscopy	42
3.8	Electron energy loss spectroscopy.....	44
3.9	TEM sample preparation	44
3.10	Chapter references.....	48
4	Experimental details.....	49
4.1	Chemicals and substrates	49
4.1.1	Synthesis of Copperindiumdisulfide.....	50
4.1.2	Synthesis of Titaniumdioxide	50
4.2	Equipment	51
5	Synthesis and characterization of CuInS ₂ thin film structures	53
5.1	Introduction	53
5.2	Experimental	54
5.3	Characterization	55
5.4	Results and discussion.....	56
5.5	Summary	67
5.6	Chapter references	68

Table of contents

6	Systematic study of the reactant concentration and reaction times on CuInS ₂ films	69
6.1	Introduction	69
6.2	Experimental details.....	70
6.3	Characterization	71
6.4	Results.....	71
6.5	Discussion.....	83
6.6	Summary and Conclusion	85
6.7	Chapter references	86
7	Investigation of the growth of CuInS ₂ microspheres.....	87
7.1	Introduction	87
7.2	Experimental details.....	88
7.2.1	Synthesis.....	88
7.2.2	Characterization	88
7.3	Results.....	89
7.4	Discussion.....	97
7.5	Conclusion.....	103
7.6	Associated content.....	104
7.7	Chapter references	107
8	L-cysteine assisted growth of CuInS ₂ films	109
8.1	Introduction	109
8.2	Experimental details.....	110
8.3	Characterization	111
8.4	Results.....	112

Table of contents

8.5	Discussion	121
8.6	Conclusion.....	123
8.7	Chapter references	124
9	Optimization of sol-gel synthesized TiO ₂ blocking layers.....	125
9.1	Introduction	125
9.2	Experimental	126
9.3	Characterization	127
9.4	Results and discussion	128
9.5	Summary and Conclusion	133
9.6	Chapter references	134
10	Conclusion and Outlook.....	135
11	Appendix.....	139
12	Curriculum Vitae.....	143
13	List of Publications and Presentations.....	145
13.1	Publications	145
13.2	Oral Presentations.....	146
13.3	Poster Presentations	146

List of abbreviations

µm	Micro meter (10^{-6} m)
ADF	Annular dark field
ALD	Atomic layer deposition
BF	Bright field
CBD	Chemical bath deposition
CIGS	Copper, Indium, Gallium, Sulphide
CIGSSE	Copper, Indium, Gallium, Sulphide, Selenium
CIS	Copperindiumdisulfide, CuInS_2
CVD	Chemical vapor deposition
DSSC	Dye-sensitized solar cells
EDX	Energy dispersive X-ray spectroscopy
EELS	Electron energy loss spectroscopy
ETA	Extremely thin absorber
eV	Electron volt ($1,60 \cdot 10^{-19}$ kg · m ² · s ⁻²)
FIB	Focused ion beam
FTO	Fluorine-doped tin oxide
FWHM	Full width of half maximum
h	Hours
HAADF	High angle annular dark field
HRTEM	High-resolution TEM
ICP-AES	Inductively coupled plasma atomic emission
ILGAR	Ion layer gas reaction
ITO	Indium-doped tin oxide

List of abbreviations

keV	Kilo electron volt
min	Minutes
mm	Millimeter (10^{-3} m)
nm	Nanometer (10^{-9} m)
pA	Pikoampere
PCBM	Phenyl-C61-butansäure-methylester
PIPS	Precision ion polishing system
PVD	Physical vapor deposition
RTP	Rapid thermal processing
S	Seconds
SEM	Scanning electron microscopy
SILAR	Successive ion layer adsorption reaction
STEM	Scanning TEM
TCO	Transparent conductive oxide
TEM	Transmission electron microscopy
THF	Tetrahydrofuran
XPS	X-ray photoelectron spectroscopy
XRD	X-ray diffraction

List of symbols

A	Absorbance
Å	Angstrom
a, b, c	Cell parameters
c	Concentration of absorbing material or speed of light
C_A, C_B	Concentration of element A and B
C_s	Spherical aberration
d	Distance of lattice plane or thickness of absorbing material
E	Energy
E_g	Band gap energy
h	Planck constant
hkl	Miller indices
I	Current
I	Intensity of transmitted light
I_0	Intensity of incoming light
K	Shape factor
K_{AB}	Cliff-Lorimer factor
m_e	Effective electron mass
n	Amount of molecule or order of diffraction
p	Pressure or momentum
R	Resistance, gas constant or distance
T	Temperature
U	Voltage or inner energy

List of symbols

V	Volume
ν	Frequency
β	Line broadening at the half-maximum intensity
Δf	Defocus
ε	Extinction coefficient
θ	Bragg angle
λ	Wavelength
λL	Camera constant
τ	Domain size
ω	Angular frequency
\hbar	Reduced Planck constant

List of figures

Figure 2.1 Schematic drawing of the assembly and function of a typical solar cell.	8
Figure 2.2: Schematic drawing of a thin film solar cell based on CuInS ₂	11
Figure 2.3: Natural pure Roquesite crystal.....	12
Figure 2.4: Structures of the three modifications of CuInS ₂	13
Figure 2.5: Theoretical efficiencies as function of the band gaps.	14
Figure 2.6: The three modifications of TiO ₂	16
Figure 2.7: Three different modifications α -In ₂ S ₃ , β -In ₂ S ₃ and γ -In ₂ S ₃	20
Figure 3.1: Reaction equation of the three different reaction types, hydrolysis , alcohol condensation and water condensation distinguished during the sol-gel reaction.....	27
Figure 3.2: Acid catalyzed sol-gel mechanism used in this work.	28
Figure 3.3: Schematic illustration of the Bragg relation.....	29
Figure 3.4: Generated signals from interaction between incident electron beam and a thin specimen.....	33
Figure 3.5: Schematic diagram of a scanning electron microscope.....	34
Figure 3.6: Schematic of a dual-beam configuration with respect to the sample stage....	36
Figure 3.7: Optical path in a TEM.	38
Figure 3.8: Contrast transfer function.....	40
Figure 3.9: Schematic diagram of detector in a STEM instrument.....	41
Figure 3.10: Schematic of the relaxation of an inner-shell-excited atom.	42
Figure 3.11: Schematic diagram of the working steps of the TEM cross section sample preparation.	45
Figure 3.12: TEM grid with a diameter size of 3 mm.	46

Figure 3.13: Schematic drawing of a 3 mm diameter half-ring, used for mounting a thin TEM specimen lamella in the FIB TEM sample preparation.	47
Figure 5.1: SE images of CuInS ₂ films deposited on FTO.	57
Figure 5.2: EDX spectrum of film A measured in the SEM.....	58
Figure 5.3: XRD pattern of film A revealing the tetragonal roquesite crystal structure...	59
Figure 5.4: BF image and HAADF-STEM image of the CuInS ₂ film A.	61
Figure 5.5: BF image showing the edge of one crystal sphere.....	63
Figure 5.6: BF image of the TEM cross-section of film B.....	64
Figure 5.7: UV/Vis spectrum of film B.....	65
Figure 6.1: SE images of the CuInS ₂ films synthesized with reactant concentration A for different reaction times.	73
Figure 6.2: SE images of the CuInS ₂ films synthesized with reactant concentration B for different reaction times.	75
Figure 6.3: Graphical illustration of the chemical composition of the different synthesized films.	77
Figure 6.4: BF images of film 2A, film 5B and film 6A.	79
Figure 6.5: XRD pattern of film 3B.	80
Figure 6.6: HRTEM images of film 6A.....	82
Figure 7.1: SE images illustrating the morphology of microspheres synthesized at different reaction times.	90
Figure 7.2: XRD pattern of sample 1.	92
Figure 7.3: SE images from two sliced microspheres taken by FIB/SEM.....	94
Figure 7.4: ADF/HAADF-STEM image of the lamella from sample 1.	96
Figure 7.5: Schematically illustration of the different chemical compositions found for microspheres B in sample 1 and 2.....	98

Figure 7.6: Proposed growth mechanism of the microspheres in sample 1 and 2.....	100
Figure 7.7: XRD pattern of sample 3.	104
Figure 7.8: XRD pattern obtained from the reaction of InCl_3 and thioacetamide in ethanol for 18 h at 150 °C.....	104
Figure 7.9: Bright field TEM images of the reaction between CuSO_4 and thioacetamide in ethanol for 18 h at 150 °C.....	105
Figure 8.1: SE images of three CuInS_2 films synthesized with different concentrations of reactants on FTO substrates.	113
Figure 8.2: XRD pattern of film A and B.....	115
Figure 8.3: UV /Vis spectra of film A, B and C.....	116
Figure 8.4: BF image and ADF-STEM image of film B.....	117
Figure 8.5: XRD pattern of the grey reaction product of L-cysteine and CuSO_4	119
Figure 8.6: High resolution TEM image of the reaction product of L-cysteine and CuSO_4 in ethanol.....	120
Figure 8.7: EELS spectra taken from the product of L-cysteine and CuSO_4	120
Figure 8.8: Oxidation from L-cysteine to L-cystine.	121
Figure 9.1: Schematic of the different oven programs.....	127
Figure 9.2: (a) shows film 4 which was spin coated with higher speed.....	128
Figure 9.3: High resolution TEM images of film 1, film 2, film 3, film 4 and film 5.....	129
Figure 9.4: Addition of the grain size against the calcination temperatures.	130
Figure 9.5: I-U curves from the films 1 - 5.	131

List of tables

Table 2.1: Structural and material properties of CuInS ₂ possessing Chalcopyrite, Wurtzite and Zinblende modification.	14
Table 2.2: Structural and material properties of TiO ₂ in Rutile, Anatase and Brookite modification.....	17
Table 2.3: Structural and material properties of coppersulfide.....	19
Table 2.4: Structural and material properties of In ₂ S ₃	21
Table 4.1: Used chemicals and substrates	49
Table 4.2: Used equipment.	51
Table 6.1: Reactant concentration and used reaction times for all synthesized films.	70
Table 6.2: Film thicknesses of the films synthesized with reactant concentration A for different reaction times.	74
Table 6.3: Film thicknesses of the films synthesized with reactant concentration B for different reaction times.	76
Table 6.4: Average chemical composition of the films synthesized with reactant concentration A and B with reaction times between 0.5 – 9 h measured in the SEM.	77
Table 6.5: Calculated <i>d</i> values, <i>hkl</i> and particular angles between the reflections for CuInS ₂ in Chalcopyrite, Zinblende and Wurtzite structure.....	81
Table 6.6: Measured angles between the atomic plane distances obtained from FFT analysis.....	82
Table 7.1: 2θ and <i>d</i> values observed in the X-ray and electron diffraction patterns from CuInS ₂ in Roquesite and Wurtzite structure as well as CuS and In ₂ S ₃ compared to literature data.....	93
Table 7.2: 2θ and <i>d</i> values observed in the electron diffraction patterns from CuS and Cu ₂ S compared to literature data.....	106

List of tables

Table 8.1: Different concentrations of reactants of the three prepared films A, B and C.	111
Table 8.2: Observed d and 2θ values of the electron diffraction pattern of the grey solid.	121
Table 9.1: Average grain size observed in film prepared at different dwell times during calcination.	129
Table 9.2: Resistances of the measured films 1 - 5.....	131

1 Introduction

The energy economy, especially in the industrialized countries, is based on the use of stored energies. These are mainly fossil energies for example carbon, fossil oil and natural gas, but also nuclear energy in form of uranium isotopes such as U^{235} . Hereby, two main problems exist. On the one hand the reservoir of these energy resources is limited and the consumption has increased exponentially in the last years because of rising industrialization. On the other hand the use of these energy sources is associated with a vast environmental burden.^[1] Already in the 80's, national and international studies like „Global 2000“ (1980) or the Brundtland-Report (1987) documented the condition of the earth and the anthropogenic influence on the environment was scientifically proven. Consequently, the necessity in a global acting was clear. Further reasons for an increased environmentalism was the finding of the ozone hole in 1985, the nuclear disaster in Tschernobyl in 1986 and the evidence of the greenhouse effect through investigations of drillings in the Antarctic in 1985.^[2] Since then, especially the climate problematic is discussed. It has been proved, that a global warming of about 3 °C in the next 100 years is to be expected,^[3] whereby the cause of this temperature increase is the rising energy consumption. This is mainly because of the burning of fossil energy sources, whereby resulting carbon dioxide enters the atmosphere. The concentration of atmospheric CO_2 increased from 1959 to 1999 from 315 to 370 ppm, thus an upward trend can be observed. The consequence is that the carbon implemented in the earth's surface during millions of years by biological activity (geochemical cycle) is released rapidly and contributes significantly to the current climate situation. Because of these findings the CO_2 emissions has to be reduced, which is only realizable with the effort of renewable energy sources like sun-, water- or wind energy. These count as CO_2 -neutral and are infinitely available. One reason for their still low percentage in the energy supply is the inferior economic efficiency compared to the existing conventional systems.

Therefore, big efforts are necessary to make these energy forms able to compete economically and it is an active field in research and science. In the area of photovoltaic (direct conversion of sun light in electric energy) current aims are advancement of existing systems concerning higher efficiencies, better long term

stability and reduction of manufacturing costs. High production cost and low availability are the disadvantages for conventional Si-based solar cells. Therefore, research of alternative non Si-based semiconductor materials and the improvement of existing or development of novel structures and morphologies is an active field of research.^[4] An alternative absorber material for solar cell applications is Copperindiumdisulfide (CuInS_2). Because of its high absorption coefficient of 10^5 cm^{-1} , which enables it to absorb the majority of light quanta of the solar spectrum above the direct band gap of $E_g = 1.53 \text{ eV}$, only thin films of this absorber material are used in solar cells leading to good efficiencies. Factors like low cost educts as well as low cost and simple synthesis procedures and the less needed amount of material for thin films make CuInS_2 an ideal absorber material for economic and efficient solar cells. Already in 1993 the manufacturing of a thin film solar cell based on p- CuInS_2 /n-CdS with an efficiency of 10% was reported.^[5] This solar cell was built with a Mo-layer as back contact added by sputter deposition. The CuInS_2 absorber was deposited by physical vapor deposition (PVD) or by rapid thermal processing (RTP). Afterwards a thin CdS layer was deposited by chemical bath deposition (CBD). At the front side of the heterostructure a transparent Al doped ZnO layer was used as conductive electrode. The complete cell thickness was about $5 \mu\text{m}$. To increase the efficiency of this type of solar cell, a better adaption of the band gaps was performed by replacing CuInS_2 with CuInSe_2 . With these solar cells efficiencies of 16% were reached.^[6, 7] Also with the so called CIGSSE ($\text{CuIn}_x\text{Ga}_{1-x}\text{S}_{2y}\text{Se}_{2(1-y)}$) thin film solar cells, high efficiencies could be achieved. The band gap of this material can be adapted to the sun light by adding Ga and S to CuInSe_2 . This kind of solar cells is already industrially produced for example from AVANCIS.^[8]

The advantage of CuInS_2 however is the nontoxicity of S compared to Se and the higher amount of S available compared to the trace mineral Se.^[9] Therefore, a lot of research studies are dedicated to CuInS_2 solar cells with different built ups and structures and processed by varying manufacturing techniques. For example John et al.^[10] reported about $\text{CuInS}_2/\text{In}_2\text{S}_3$ thin film solar cells which were prepared by a spray pyrolysis technique and which achieved an efficiency of 9.5%. The cell was built on indium tin oxide (ITO) coated glass substrates and the cell structure was ITO/ CuInS_2 / In_2S_3 /Ag. Siemer et al.^[11] developed a CuInS_2 based solar cell

manufactured with the RTP process having 11.4% efficiency. Their solar cell structure was glass/Mo/CuInS₂/CdS/ZnO. Even hybrid solar cells based on CuInS₂ are already reported in literature. Bereznev et al.^[12] for example showed a solar cell built up of Cu/CuInS₂/Zn-phthalocyanin(ZnPc):fullerene/Cr/Au which gave an efficiency of 3.3%. The fabrication of an extremely thin absorber (ETA) solar cell based on CuInS₂ was reported by Lenzmann et al.^[13] This type of solar cell exhibits a 10 – 30 nm thin absorber layer. The solar cell structure was FTO/dense TiO₂ layer/nanostructured TiO₂/CuInS₂/Au. The deposition of the CuInS₂ was done by atomic layer deposition (ALD) and spray pyrolysis. With this solar cell they reached an efficiency of 3%. Further synthesis procedures are investigated to obtain CuInS₂ solar cells, for example the chemical vapor deposition (CVD)^[14], sulfurization of metallic precursors^[15], co-evaporation^[16], electro deposition^[17, 18], and ion layer gas reaction^[19] were developed. Besides these expensive methods, also low cost synthesis routes were explored such as CBD^[20, 21], successive ionic layer adsorption and reaction (SILAR)^[22] and mild solvothermal synthesis routes.^[23, 24] Peng et al.^[23] fabricated CuInS₂ based solar cells using a mild solvothermal synthesis route. They obtained CuInS₂ films with a high surface density consisting of flower-like nanoplates. This is advantageous for solar cell applications because of the possibility to create and separate a high amount of charge carriers at occurring interfaces when combined with a suitable semiconductor. They used fluor doped tin oxide (FTO) as conductive, transparent electrode. In their work they showed two solar cell structures Ag/CdS/CuInS₂/FTO and FTO/TiO₂/CuInS₂/Au possessing 0.33% and 0.29% efficiency. The low efficiency of the cells is reasoned by the poor contact between the CuInS₂ absorber, the CdS layer, and the electrode. Additionally, the high thickness of the films could have a negative influence on the efficiency.

Transparent conductive oxides (TCO) like ITO and FTO coated on glass are common used electrodes in novel organic and inorganic solar cells. In addition, TiO₂ is often applied as electron conductor in inorganic or hybrid solar cells but is also used as blocking layer, to prevent short circuits and reduce recombinations. These films are directly coated on the TCO as shown in the publication of Peng et al.^[23] and Lenzmann et al.^[13] Various investigations were done to obtain thin homogenous TiO₂ films on ITO layers or FTO.^[25, 26] Also the influence of these blocking layers was investigated

regarding the solar cell performance. Cho et al.^[27] for example studied the effect of sol-gel formed TiO₂ blocking layers on the efficiency of dye-sensitized solar cells. They used FTO as working electrode on which the TiO₂ film was deposited. With the use of the blocking layer they obtained an increase of efficiency of 16%. The short circuit current density and the open circuit voltage were also increased because of the decreasing recombination rate at the TCO/electrolyte interface. Similar results were obtained from Cameron et al.^[28] using spray pyrolysis as deposition method. Peng et al.^[29] reported about the role of compact TiO₂ layers in solid state dye-sensitized TiO₂ solar cells. They prepared solar cells with the structure FTO/blocking TiO₂/hole conductor/Au. Among others they investigated the influence of the TiO₂ blocking layer on the solar cell's performance. They obtained the best results with a film thickness of 150 nm.

1.1 Aim of the thesis

Within the scope of this thesis a synthesis strategy should be developed to obtain homogeneous and reproducible CuInS₂ thin films on FTO substrates exhibiting a high surface area, which is an essential property for solar cells. Regarding the aspect of a low cost manufacturing process a mild solvothermal synthesis route is applied. Two different sulfur sources are used for the synthesis of the films. Beside the toxic thioacetamide, the non toxic amino acid L-cysteine is used to minimize the toxicity of the synthesis process. For both sulfur sources experiments at different reaction times and concentrations of the reactants are performed and the influence on the film thickness and morphology is studied. Additionally, the growth mechanisms, chemical compositions and structures of the various films are investigated.

Furthermore, TiO₂ thin films, applicable as blocking layer in solar cells are synthesized in the present work via a sol-gel method, optimized and characterized regarding the influence of different calcination times on the grain size in the films. The effect of the grain size on the conductivity is studied. A large increase in the conductivity of the synthesized layers should have a positive effect on the solar cell performance.

Detailed investigations of the different CuInS₂ and TiO₂ films are performed with scanning electron microscopy (SEM) for general microstructure characterization. For in-depth analysis at the nanometer scale various transmission electron microscopy (TEM) techniques are applied. The latter include diffraction studies, conventional TEM, high-resolution TEM (HRTEM) and high-angle annular dark-field (HAADF) imaging in the scanning TEM (STEM) mode to determine the crystal structure, phase, morphology and grain size. For the analysis of the chemical composition energy-dispersive X-ray spectroscopy (EDX) in the TEM and SEM and inductively coupled plasma atomic emission spectrometry (ICP-AES) are used. Additional characterization of the crystal structure is done by X-ray diffraction (XRD). UV-Vis measurements on promising CuInS₂ films are performed to study the absorption behavior.

1.2 Chapter references

- [1] P. Würfel, *Physik der Solarzellen*, 2 ed., Spektrum, Heidelberg, **2000**.
- [2] C. Lorius, J. Jouzel, C. Ritz, L. Merlivat, N. I. Barkov, Y. S. Korotkevich, V. M. Kotlyakov, *Nature (London)* **1985**, 316, 591-596.
- [3] E. U. v. Weizäcker, *Erdpolitik*, 4 ed., WBV, Berlin, **1994**.
- [4] H. J. Lewerenz, H. Jungblut, *Photovoltaik*, 1 ed., Springer, Heidelberg, **1995**.
- [5] R. Scheer, T. Walter, H. W. Schrock, M. L. Fearheiley, H. J. Lewerenz, *Appl. Phys. Lett.* **1993**, 63, 3294-3296.
- [6] J. R. Sites, J. E. Granata, J. F. Hiltner, *Sol. Energy Mater. Sol. Cells* **1998**, 55, 43-50.
- [7] A. Rockett, R. W. Birkmire, *J. Appl. Phys.* **1991**, 70, R81-R97.
- [8] AVANCIS GmbH & Co. KG, AVANCIS, **2012**, <http://www.avancis.de/> 03.09.2012.
- [9] A. Ennaoui, S. Siebentritt, M. C. Lux-Steiner, W. Riedl, F. Karg, *Sol. Energy Mater. Sol. Cells* **2001**, 67, 31-40.
- [10] T. T. John, M. Mathew, C. S. Kartha, K. P. Vijayakumar, T. Abe, Y. Kashiwaba, *Sol. Energy Mater. Sol. Cells* **2005**, 89, 27-36.
- [11] K. Siemer, J. Klaer, I. Luck, J. Bruns, R. Klenk, D. Braunig, *Sol. Energy Mater. Sol. Cells* **2001**, 67, 159-166.
- [12] S. Bereznev, R. Koeppel, I. Konovalov, J. Kois, S. Guenes, A. Oepik, E. Mellikov, N. S. Sariciftci, *Thin Solid Films* **2007**, 515, 5759-5762.
- [13] F. Lenzmann, M. Nanu, O. Kijatkina, A. Belaidi, *Thin Solid Films* **2004**, 451-452, 639-643.
- [14] J. A. Hollingsworth, K. K. Banger, M. H. C. Jin, J. D. Harris, J. E. Cowen, E. W. Bohannon, J. A. Switzer, W. Buhro, A. F. Hepp, *Thin Solid Films* **2003**, 431, 63-67.
- [15] H. J. Muffler, C. H. Fischer, K. Diesner, M. C. Lux-Steiner, *Sol. Energy Mater. Sol. Cells* **2001**, 67, 121-127.
- [16] R. Scheer, I. Luck, M. Kanis, M. Matsui, T. Watanabe, T. Yamamoto, *Thin Solid Films* **2001**, 392, 1-10.
- [17] S. i. Kuranouchi, T. Nakazawa, *Sol. Energy Mater. Sol. Cells* **1998**, 50, 31-36.
- [18] T. Yukawa, K. Kuwabara, K. Koumoto, *Thin Solid Films* **1996**, 286, 151-153.
- [19] J. Möller, C. H. Fischer, H. J. Muffler, R. Könenkamp, I. Kaiser, C. Kelch, M. C. Lux-Steiner, *Thin Solid Films* **2000**, 361-362, 113-117.
- [20] P. Guha, D. Das, A. B. Maity, D. Ganguli, S. Chaudhuri, *Sol. Energy Mater. Sol. Cells* **2003**, 80, 115-130.
- [21] H. M. Pathan, C. D. Lokhande, *Appl. Surf. Sci.* **2004**, 239, 11-18.
- [22] Y. Shi, Z. Jin, C. Li, H. An, J. Qiu, *Appl. Surf. Sci.* **2006**, 252, 3737-3743.
- [23] S. Peng, F. Cheng, J. Liang, Z. Tao, J. Chen, *J. Alloys Compd.* **2009**, 481, 786-791.
- [24] C. Wen, X. Weidong, W. Juanjuan, W. Xiaoming, Z. Jiasong, L. Lijun, *Mater. Lett.* **2009**, 63, 2495-2498.
- [25] B. Yoo, K.-J. Kim, S.-Y. Bang, M. J. Ko, K. Kim, N.-G. Park, *J. Electroanal. Chem.* **2010**, 638, 161-166.
- [26] H. Yu, S. Zhang, H. Zhao, G. Will, P. Liu, *Electrochim. Acta* **2009**, 54, 1319-1324.
- [27] T.-Y. Cho, S.-G. Yoon, S. S. Sekhon, M. G. Kang, C.-H. Han, *Bull. Korean Chem. Soc.* **2011**, 32, 3629-3633.
- [28] P. J. Cameron, L. M. Peter, *J. Phys. Chem. B* **2003**, 107, 14394-14400.
- [29] B. Peng, G. Jungmann, C. Jager, D. Haarer, H.-W. Schmidt, M. Thelakkat, *Coord. Chem. Rev.* **2004**, 248, 1479-1489.

2 Theoretical background

2.1 Solar cells

Solar cells are electrical devices which convert short wavelength radiation energy like in the spectrum of sunlight into electrical energy. The physical background of this is the photoelectric respectively - photovoltaic effect. This effect was discovered first from Alexandre Edmond Becquerel in 1839.^[1, 2] The photoelectric effect leads to the emission of electrons from material surfaces due to the absorption of electromagnetic radiation with short wavelength like visible or ultraviolet radiation. The energy of the photon must be at least equal to the binding energy of the emitted electron. The photoconductive effect, which is a type of the inner photoelectric effect, increases the conductivity of semiconductors during illumination with light due to creation of additional electron hole pairs. Electrons are raised from the valence band into the energetically higher conduction band through the absorption of a photon. The energy of the photon must correlate to the band gap energy of the irradiated semiconductor, i.e. it has to be equal or larger than the band gap energy of the semiconductor. The photovoltaic effect is also based on the inner photoelectric effect. Charge carrier pairs (electron hole pairs) are created during illumination with light. In the depletion region (also called depletion layer or p-n junction) of a semiconductor device the charge carriers are separated by an intrinsic electric field and a current occurs.^[1-4]

2.1.1 Solar cell assembly and function

Besides the material of a solar cell also the construction and design are crucial. Usually semiconductor materials which can convert the whole spectrum of sunlight to electron-hole pairs are used. This demands for a specific width of the band gap, small enough to harvest the low energy of red light, but large enough to generate a sufficient potential. An electric field is required to separate the charge carriers, thus resulting in an electric current. It can be created by p-n junctions, which are obtained in a single crystal by gradually doping with elements of lower valency for p-type character or higher valency for n-type character. At the interface between p-and n-type regions a space charge zone is formed which creates an electric field that prevents further diffusion. Since the density of charge carriers in the diffusion zone is low, the transition zone is also denoted

as depletion region. Incident photons with an energy of $E = \hbar\omega$ (\hbar reduced Planck constant, ω angular frequency) greater than the band gap excite an electron from the valence band to the conduction band thus, creating a hole in the valence band. These electron-hole pairs are separated by the electric field at the p-n junction and conducted to the opposite electrodes of the cell. The photo-current can be directly used by a consumer, cached in an accumulator or injected in a power supply system. The assembly of solar cells is usually designed in a way that as much light as possible can be cached and that a large number of charge carriers can be created. For this, the electrode has to be transparent on the surface and additionally an anti reflection layer is deposited. The assembly and function of a typical solar cell is shown in Figure 2.1.^[3, 4]

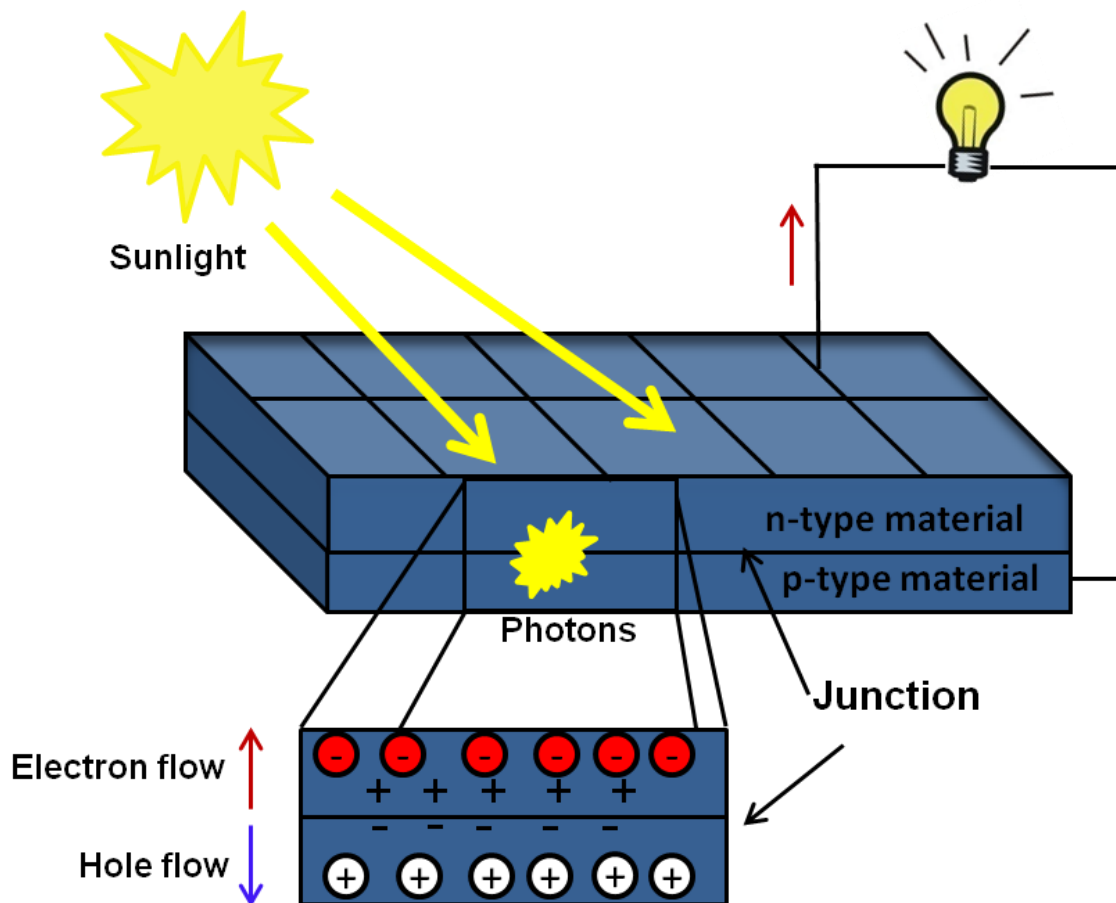


Figure 2.1 Schematic drawing of the assembly and function of a typical solar cell. Localized charges are labeled as +, - while free holes and electrons are denoted as \oplus , \ominus .

2.1.2 Solar cell types

Silicon based solar cells

The first commercially available solar cell was based on silicon and developed in 1953^[5] To date, 28% efficiency can be reached by single-crystal silicon solar cells.^[6-8] Despite of the relative high efficiency, there are several disadvantages. For example a high energy effort to produce the material, which leads to high production cost. In addition, silicon exhibits an indirect band gap of 1.12 eV which does not match well to the solar spectrum. Furthermore, Si exhibits a low absorption coefficient. Therefore silicon based solar cells have to be thicker than solar cells based on other materials with direct band gaps and higher absorption properties. Most of these problems can be minimized by using different types of silicon solar cells for example polycrystalline, amorphous, microcrystalline or tandem Si solar cells (combination of polycrystalline and amorphous cells on top of each other). Until now most of the commercially available solar cells are thus still based on silicon.^[6, 9, 10]

Concentration cells

In concentration cells the light is focused with additional lenses on the semiconductor material. Therefore, less amount of material is needed and material costs can be economized. Frequently used materials for these cells are III-V semiconductors.^[8]

Organic and hybrid solar cells

Because of the low production costs and various manufacturing methods organic solar cells are an active area in research.^[11] They possess a high current yield, flexibility, transparency and easy handling. Additionally, they are environment-friendly and they can adapt on the solar spectrum. The conjugated π -electron system of the used hydrocarbon based materials gives the material semiconductor properties. The first plastic solar cells were two-layer-solar cells existing of conjugated polymers (hole conductor) and fullerenes (electron conductor).^[12, 13] Meanwhile, research is focused on blend polymer solar cells where the n- and p-type regions are intermixed and a higher interface area is achieved.^[14, 15] The disadvantages of organic solar cells are a shorter lifetimes and instabilities compared to silicon based solar cells. Dye-sensitized solar cells (DSSCs) are another promising development introduced by O'Regan and Grätzel in

1991.^[16-18] They are built of a mesoporous TiO₂ layer which is deposited on a transparent conductive glass. The TiO₂ layer is coated with a ruthenium complex based dye and the two contacts are filled with an electrolyte solution. The dye absorbs the incident photons and injects the photo generated electrons into the conduction band of the TiO₂. The now oxidized dye molecules are reduced by the electrolyte solution and a current flow. The disadvantage is the short lifetime of the cell and the aggressive electrolyte solution. They belong to the classes of hybrid solar cells which are made up of organic and inorganic material. Further types of nanostructured hybrid solar cells are nowadays an active field in research. Different designs are based on TiO₂^[19] or ZnO^[20] nanotubes^[21] or nanorods,^[10] as well as mesoporous TiO₂ films^[22] in combination with a semiconducting polymer. With this a high interface area for an improved creation of electron-hole pairs is obtained in literature.^[22, 23]

Extremely thin absorber solar cells

The extremely thin absorber (ETA) concept has been introduced in 1997 to the scientific community.^[24] ETA solar cells consist of an ultra thin absorber layer which is deposited on the high surface area of a mesoporous metal oxide (e.g. TiO₂ or ZnO) film which acts as electron conductor. This mesoporous film is combined with a suitable solid hole conductor. To minimize recombination of electron hole pairs additional buffer layers are used between the absorber layer and the electron conductor. These solar cells comprise also the positive aspects of low cost manufacturing and belong to the class of thin film solar cells. ETA solar cells have been developed and investigated with various different absorber materials e.g. PbS^[25], Cu₂S^[26], Sb₂S₃^[27], CdTe^[28] or CuInS₂ which are combined with different solid hole semiconductors e.g. CuSCN. In case of CuInS₂, a related concept was published by Lenzmann et. al.^[29], however, an additional hole conductor was not needed since CuInS₂, depending on the composition, can act as p-type semiconductor. .

Thin film solar cells

The difference of thin film solar cells compared to conventional Si solar cells is the small layer thickness (100 times thinner than conventional Si solar cells) and the novel production methods. Physical properties and the efficiency of this class of solar cells render them promising for future application. To date popular thin film solar cells are based on amorphous silicon. Further materials are polycrystalline silicon or

semiconductor materials like III-V (e.g. GaAs), II-VI (e.g. CdTe) or I-III-VI (e.g. CuIn(Ga)Se₂ (CIGS) and CuInS₂ (CIS)). Thereby I, II and VI indicates the groups of the elements in the periodic system. Efficiencies up to 20% for CIGS and up to 16% for CdTe laboratory cells have already been reached.^[30] Thin film solar cells are cheap in production costs because of the used materials and production methods. Additionally, the low rates of the production effort energy, as well as the emission of non noxious substances during the production are important criteria. Merely the shortage of the needed resources, particularly In, Ga, Te and Se seems to be a problem.^[8, 31, 32] However, low material amount needed in this type of solar cells, this problem is minimized. A scheme of a thin film solar cell based on CuInS₂ is shown in Figure 2.2. Here the p-type CuInS₂ absorber layer is coated on a metal oxide blocking layer which again is deposited on a transparent conductive oxide (TCO) coated glass substrate. The absorber layer is in contact with a suitable electron conductor. Hereby, the space charge zone is formed on the interface. The created holes in the CuInS₂ are transported to the TCO while the electron conductor transports the electrons to the counter electrode. The counter electrode is usually a metallic contact made out of Au, Ag or Al.

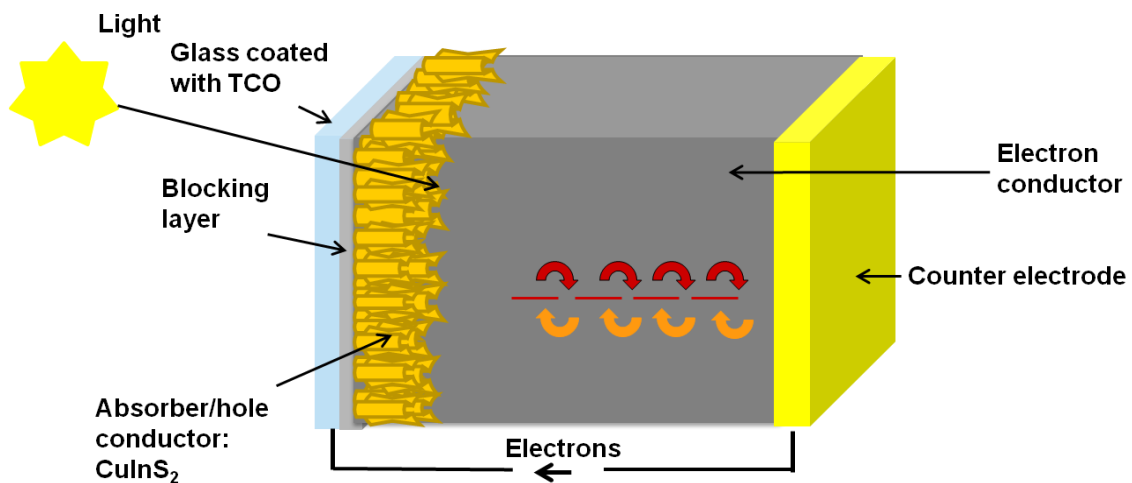


Figure 2.2: Schematic drawing of a thin film solar cell based on CuInS₂.

2.2 Materials

In the following sections the crystal structures and properties of the material relevant for the thesis are summarized.

2.2.1 Copperindiumdisulfide

Copperindiumdisulfide (CuInS_2) can be found in nature as the mineral Roquesite which belongs to the mineral class of sulfides and sulfa salts. It forms microscopic small crystals with blue-gray color (Figure 2.3).^[33]

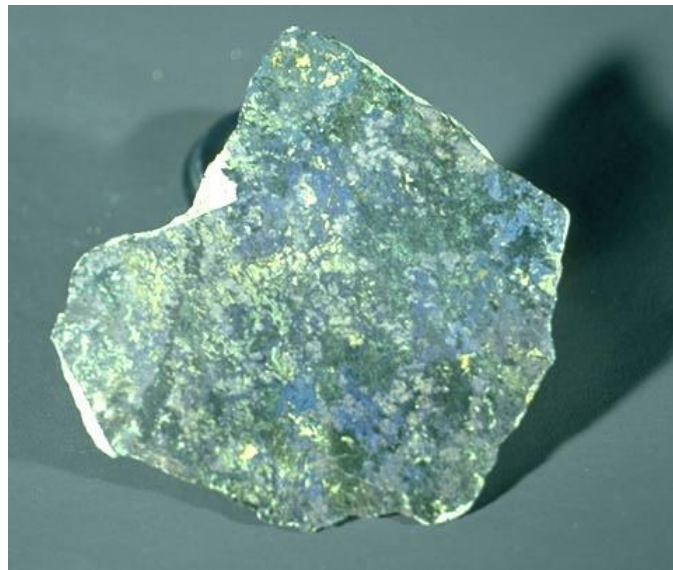


Figure 2.3: Natural pure Roquesite crystal.^[33]

CuInS_2 is a semiconductor, with the composition I-III-VI₂, where I stand for copper, II for indium and III for sulfur.^[34] From this material, three modifications are known, which can all be reduced from the Diamond structure following the Grimm-Sommerfeld rule.^[35] At room temperature, the Chalcopyrite structure ($I\bar{4}2d$) is formed.^[36] The unit cell contains eight tetrahedrons, each with two Cu and two In at the corner and one S in the middle.^[35, 37] At 980 °C, a displacive phase transition leads to the Zinblende structure ($I\bar{4}3m$). Compared to the Chalcopyrite structure, the cationic positions in the Zinblende structure are slightly distorted, resulting in a higher symmetry. At 1045 °C, a reconstructive transition leads to the Wurtzite structure ($P6_3mc$).^[38-40] All three crystal structures are shown in Figure 2.4, structural and material properties are given in Table 2.1.

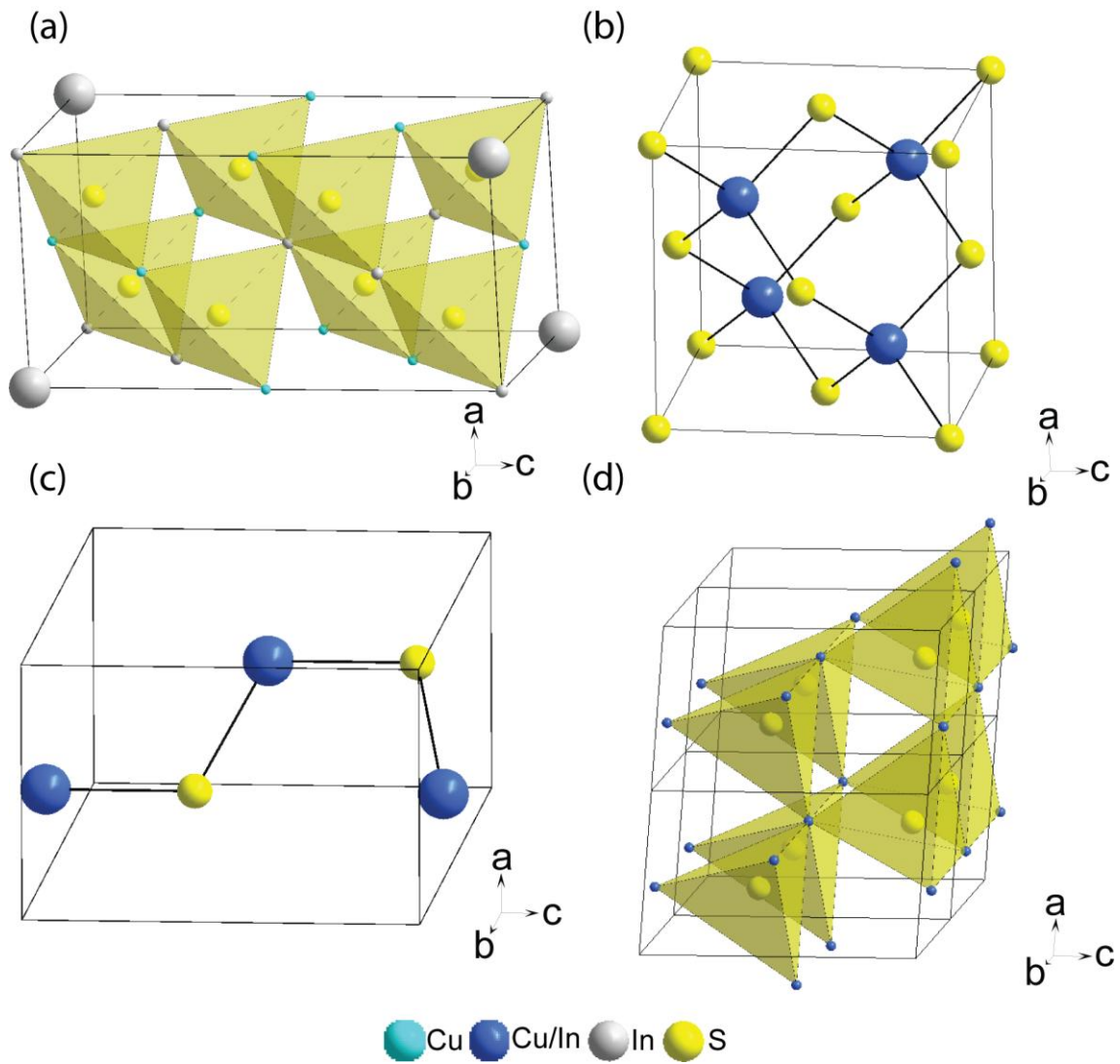


Figure 2.4: Structures of the three modifications of CuInS_2 . (a) shows one unit cell of the Chalcopyrite structure with the $\text{S}(\text{Cu,In})_4$ tetrahedrons. (b) displays one unit cell of the Zincblende structure, (c) one unit cell of the Wurtzite structure. Please note that in (b) and (c) the black lines connecting the atoms are not chemical bonds, but are supposed to clarify the structural composition. In (d), a $2 \times 2 \times 1$ supercell of the Wurtzite structure is shown with the $\text{S}(\text{Cu,In})_4$ tetrahedrons as a structural motif.

Table 2.1: Structural and material properties of CuInS₂ possessing Chalcopyrite, Wurtzite and Zinblende modification.

	Chalcopyrite ^[37]	Wurtzite ^[40]	Zinblende ^[38, 41]
Crystal system	tetragonal	hexagonal	cubic
Lattice constants (Å)	a = 5.52 c = 11.12	a = 3.91 c = 6.43	a = 5.52
Space group	$I\bar{4}2d$	$P6_3mc$	$I\bar{4}3m$
Band gap (eV)	1.52	1.42	1.07

Since, the room temperature modification of CuInS₂, Chalcopyrite, possesses a direct band gap of 1.52 eV and an absorption coefficient of 10⁵ cm⁻¹, it is a promising absorber material for solar cells.^[42] In Figure 2.5 the theoretical predicted efficiencies are plotted against possible band gaps.

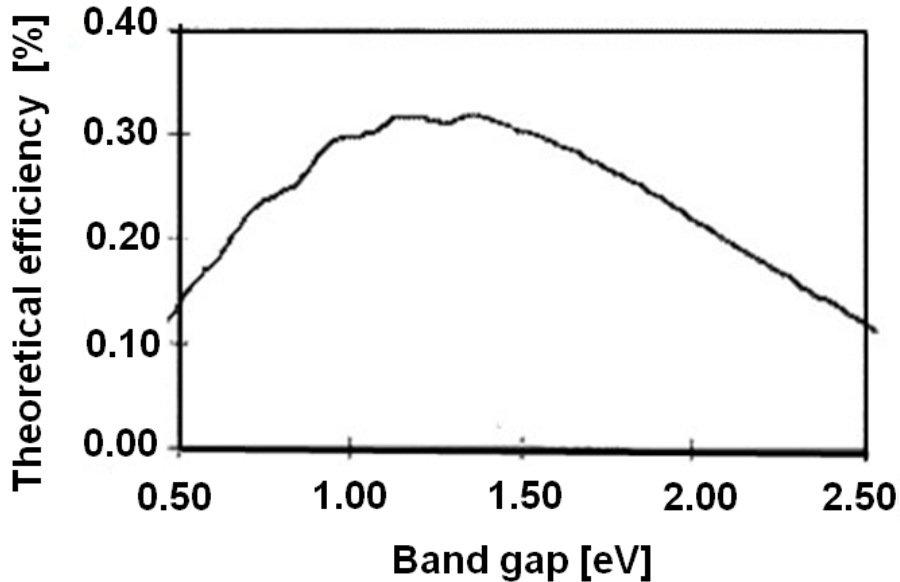


Figure 2.5: Theoretical efficiencies as function of the band gaps. A band gap of 1.5 eV is predicted to lead to a theoretical efficiency of 30%.^[4]

It can be seen that a solar cell with a band gap of about 1.5 eV can reach a maximum theoretical efficiency of 30%.^[4] Furthermore, depending on the chemical composition, CuInS₂ shows n-type or p-type properties. In that way the conductivity depends on defects for example defects in the cationic lattice or substitution with other atoms. Because Cu has a lower number of electrons than In, Cu-rich CuInS₂ exhibits p-type properties. Consequently, an electron deficiency exists and hole conducting properties dominate.^[42] Different synthesis methods for the fabrication of CuInS₂ nanostructures such as elemental chemical vapor deposition^[34], sulfurization of metallic precursors^[43], spray pyrolysis^[44], co-evaporation^[45], electro deposition^[46, 47], and ion layer gas reaction exist.^[48] Besides these cost-intensive methods, new approaches involving facile and low cost reactions have recently been explored. Synthesis methods such as chemical bath deposition^[49, 50], successive ionic layer adsorption and reaction^[51] as well as mild solvothermal synthesis routes^[52, 53] have been successfully applied to synthesize CuInS₂.

2.2.2 Titaniumdioxide

In nature, titanium dioxide exists in the three modifications Rutile, Anatase and Brookite. At room temperature, Rutile is stable. Its structure can be described by a slightly disordered hexagonal closed packing of O atoms in which half of the octahedral interstitials are filled with Ti atoms so that they form a body-centered tetragonal unit cell (I4₂/mnm). Each octahedron shared two vertices so that chains along one axis are formed. Additional edge-sharing leads to a three dimensional structure. The structures of Anatase and Brookite are similar to that of Rutile in that a cubic closed package of O atoms one half of the octahedral interstitials is filled. However, while in Rutile these octahedrons are connected by two vertices, they share three in the Brookite modification and four in the Anatase modification. Consequently, in all three modifications oxygen has the coordination number 3 while titanium is octahedrally coordinated by oxygen.^[54, 55] The transformation temperature from Brookite to Rutile is given at 925 °C to 1025 °C and for Anatase to Rutile at 1020 to 1130 °C.^[56] However, small particles show a high surface area and the surface energy can influence the stability of the individual modification. For example, for 2.4 nm sized particles, Anatase is the most stable modification.^[57] Commonly a 400 to 600 °C heat treatment of amorphous thin TiO₂ films is applied for conversion to Anatase.^[56] In Figure 2.6 the unit

cells of (a) Rutile, (b) Anatase and (c) Brookite are shown. Structural and material properties of Rutile, Anatase, and Brookite are given in Table 2.2.

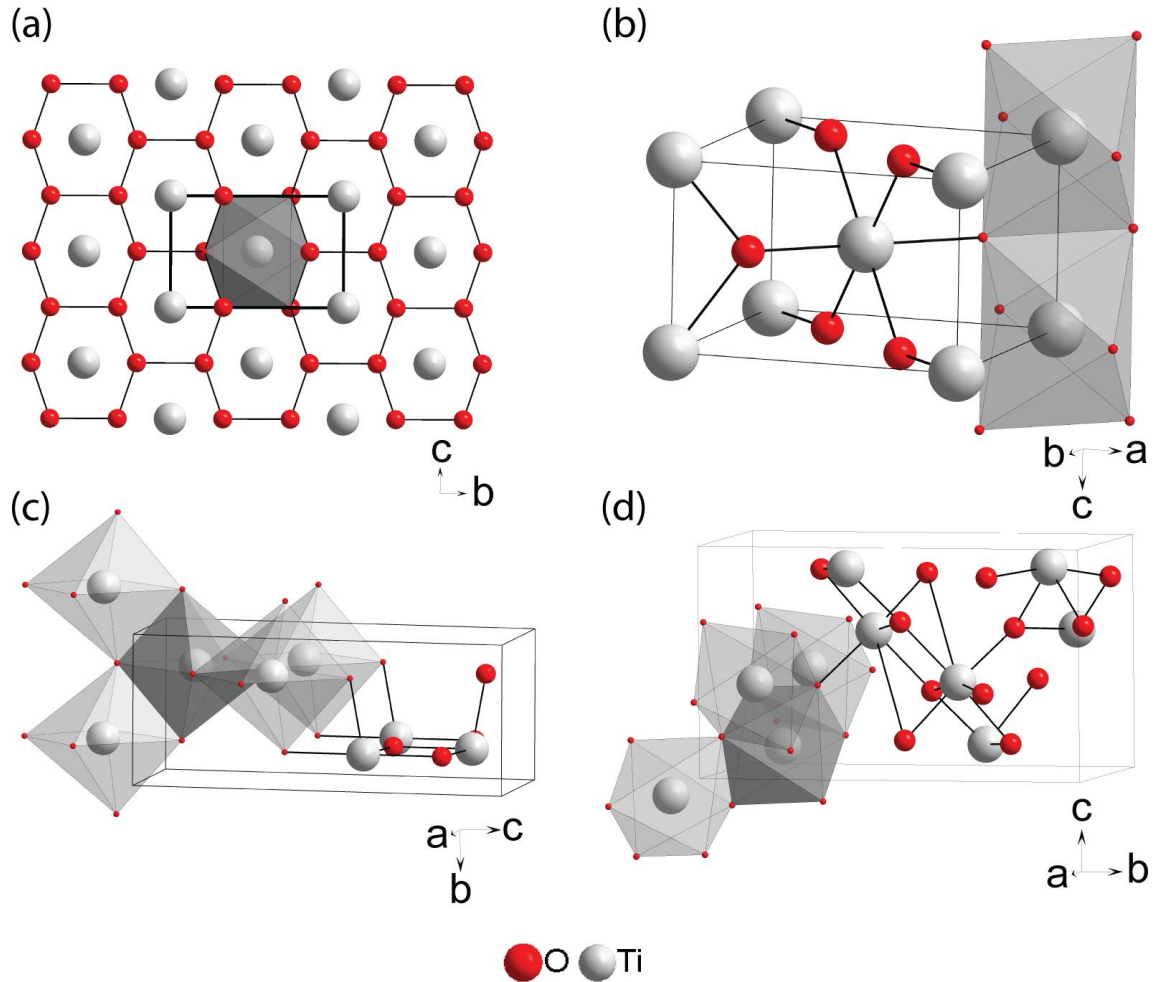


Figure 2.6: The three modifications of TiO₂. It is important to note that in all four figures black lines between the atoms are only to clarify the structural units and do not correspond to chemical bonds. In (a), the hexagonal closed packing of O atoms in the Rutile modification is shown. One tetrahedral unit cell is indicated by thick black lines and one TiO₆ octahedra is marked. In (b), one unit cell with additional oxygen to complete two TiO₆ octahedra is shown. It can be concluded that each octahedra is connected to the next by two vertices, thus forming chains. Similar to (b), (c) and (d) show unit cells of Anatase and Brookite, respectively. In both images, additional TiO₆ octahedra show the vertex-sharing of one dark-grey-colored octahedra with four, in the case of Anatase, or three, in the case of Brookite, octahedra of a lighter grey.

Table 2.2: Structural and material properties of TiO₂ in Rutile, Anatase and Brookite modification.

	Rutile^[54]	Anatase^[54]	Brookite^[55]
Crystal system	tetragonal	tetragonal	orthorhombic
Lattice constants (Å)	a = 4.5937 c = 2.9587	a = 3.7845 c = 9.5143	a = 5.4558 b = 9.1819 c = 5.1429
Space group	<i>I4₂/mnm</i>	<i>I4₁/amd</i>	<i>Pcab</i>
Band gap (eV)	3.1	3.3	1.9

Because of its chemical, electrical and optical properties TiO₂ is used in different fields such as microelectric devices or solar cells. A benefit for solar cell applications is its n-type semiconductor properties, its transparency and the different possible low cost manufacturing processes.^[58] Different nanostructures like nanotubes^[21], nanorods^[10] or mesoporous films^[22, 23] in different modifications can be obtained by synthesis such as atomic layer deposition,^[59] electrodeposition,^[60] magnetron-sputtering method,^[61] chemical vapor deposition^[59], chemical spray pyrolysis,^[62, 63] and sol-gel method^[58, 64] for applications in solar cells. TiO₂ thin films (~ 50 - 100 nm) consisting of Anatase nanoparticles are used as blocking layers to prevent short circuiting in non silicon based solar cells.^[65, 66]

2.2.3 Coppersulfide

From the Cu-S material system a large variety of compounds are known. At normal pressure (1.013 bar) and room temperature the stable forms are CuS (Covelite), α-Cu₂S (α-Chalcocite), Cu_{1.96}S (Djurleite) and Cu_{1.75}S (Anilite). Structural and material properties of all modifications mentioned in the thesis are summarized in Table 2.3.

Covelite has an indigo blue color and a hexagonal unit cell with 6 sulfur atoms in the unit cell, 4 of which form two disulfide anions (S₂²⁻). The other two are isolated sulfide ions (S²⁻). The copper cations also exist in two valence states. 4 of the cations are Cu⁺ and tetrahedrally coordinated by sulfur. One edge of the tetrahedrons consists of one single sulfide anion and the other 3 edges are sulfur atoms which are part of a disulfide anion.

The rest of the copper atoms are Cu^{2+} and trigonal planar surrounded by three single sulfur anions. Covellite is stable below temperatures of $T \leq 507 \text{ }^\circ\text{C}$.

Chalcocite is a black or blue-black crystalline solid compound which crystallizes in three distinct allotropic forms (α , β , γ) depending on the temperature. The orthorhombic Chalcocite (α - Cu_2S or lowchalcocite) is stable at low temperatures ($T \leq 103 \text{ }^\circ\text{C}$) and has a complex hexagonal close-packed crystal structure with a unit cell containing 48 Cu_2S units. Copper and sulfur atoms occupy triangular interstitials, with 21 out of the 24 non-equivalent copper atoms, forming triangular CuS_3 groups. The hexagonal β - Cu_2S , is stable between 103°C and 435°C . It crystallizes in a hexagonal lattice with the S atoms arranged in a close-packing and the Cu atoms distributed in the interstitials. The cubic Chalcocite, γ - Cu_2S or highchalcocite, is stable at temperatures higher than 435°C and shows a face-centered cubic crystalline structure.

Djurleite crystallizes in an orthorhombic cell containing 128 Cu_2S formula units and is stable at temperatures $T \leq 100 \text{ }^\circ\text{C}$. The tetragonal form is stable between 94 and $140 \text{ }^\circ\text{C}$.

Anilite is stable below $73 \text{ }^\circ\text{C}$ and has a pseudo-tetragonal unit cell containing 4 Cu_7S_4 molecules.

The low temperature phase of Digenite can be observed at temperatures of $T \leq 80 \text{ }^\circ\text{C}$ and has a cubic unit cell. The high temperature phase can be observed at temperature $T \geq 80 \text{ }^\circ\text{C}$.^[67-69] Many metastable configurations exist but these are not relevant for the present thesis and thus not described.

Table 2.3: Structural and material properties of coppersulfide.

	CuS Covellite ^[70]	α-Cu₂S α -Chalcocite ^[71]	β-Cu₂S β -Chalcocite ^[72]	Cu_{1.93}S Djurleite ^[73]	Cu_{1.74}S Anilite ^[74]	Cu₂S Digenite ^[75]
Crystal system	hexagonal	pseudo-orthorhombic	hexagonal	monoclinic	pseudo-tetragonal	cubic
Lattice constant (Å)	a = 3.79 c = 16.34	a = 15.25 b = 11.88 c = 13.49	a = 3.96 c = 6.78	a = 26.92 b = 15.71 c = 13.56	a = 7.89 b = 7.85 c = 11.01	a = 5.45
Space group	<i>P6₆/mmc</i>	<i>P2₁/c</i>	<i>P6₆/mmc</i>	<i>P2₁/n</i>	<i>Pnma</i>	<i>Fd$\bar{3}m$</i>
Band Gap (eV)	2.1	1.2-1.4	1.2-1.4	1.4	1.4	1.2

All copper sulfides are p-type semiconducting materials, attributed to free holes from acceptor levels of copper vacancies. Cu₂S can be used as a p-type semiconductor material in photovoltaic devices or as absorber material, due to its optical properties. The energy band gaps range from 1.2 to 2.4 eV and the materials exhibit a high absorption coefficient.^[68]

2.2.4 Indium(III)sulfide

For In₂S₃ three modifications are known. At room temperature, red β -In₂S₃ is stable. The crystal structure can be described as a defect spinel. Accordingly, the S forms a closed cubic package and In fills all octahedral interstitials as well as 2/3 of the tetrahedral interstitials of a regular spinel. The tetrahedral vacancies are ordered along a 4₁ screw axis parallel to the c-axis. This leads to a distortion of the cubic structure and the tetragonal space group *I4₁/amd* results. At ~ 420 °C, an order/disorder transition leads to the α -modification. While the tetrahedral vacancies are ordered in β -In₂S₃, they are now randomly distributed. The 4₁ screw axis vanishes and the structure is cubic (*Fd $\bar{3}m$*). A third modification, γ -In₂S₃ forms at ~755 °C in a trigonal structure (*P $\bar{3}m1$*). The S atoms are arranged in a nearly densed-packed sublattice and the In atoms fill

octahedral interstitials such that a layered structure of (In,S)-In-S-(In,S) stacking results. By substituting $\sim 5\%$ As or Sb instead of In, this structure can also be stabilized at room temperature.^[76, 77] All mentioned indium sulfides are indirect n-type semiconductors. Since $\beta\text{-In}_2\text{S}_3$ exhibits an optical band gap of 2.1. It is proposed to replace the toxic cadmium sulfide as a buffer layer in solar cells.^[78] The crystal structures of In_2S_3 are shown in Figure 2.7, structural and material properties are summarized in Table 2.4.

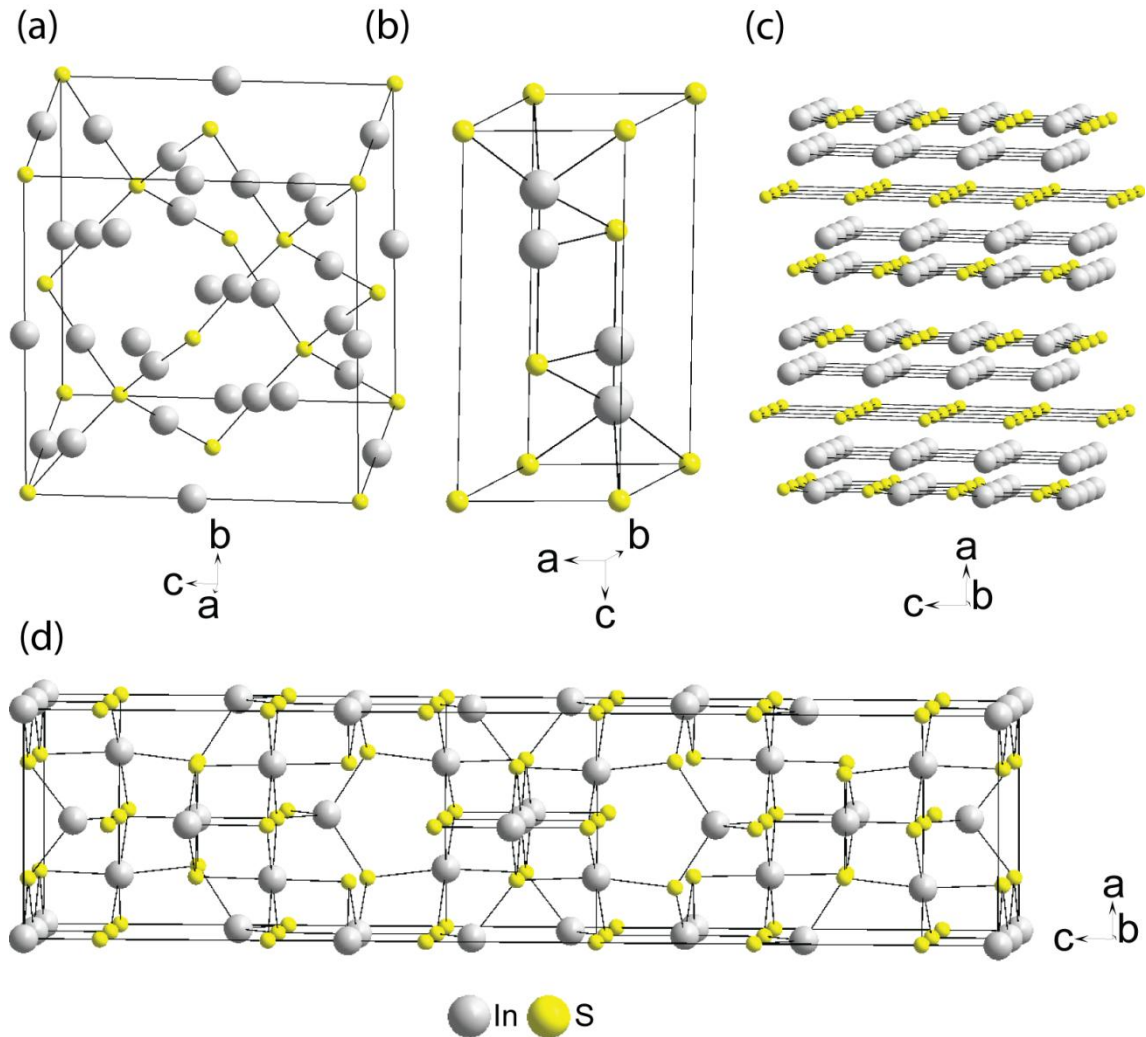


Figure 2.7: In_2S_3 can, in dependence of the temperature, form three different modifications $\alpha\text{-In}_2\text{S}_3$, $\beta\text{-In}_2\text{S}_3$ and $\gamma\text{-In}_2\text{S}_3$ of which unit cells are shown in (a), (d) and (b), respectively. In addition, the layered structure of $\gamma\text{-In}_2\text{S}_3$ can be seen in (c). It must be pointed out that lines connecting the atoms are only to show the structural units and do not correspond to chemical bonds.

2 Theoretical background

Table 2.4: Structural and material properties of In_2S_3 .

	$\beta\text{-In}_2\text{S}_3$ ^[77]	$\alpha\text{-In}_2\text{S}_3$ ^[76]	$\gamma\text{-In}_2\text{S}_3$
Crystal system	tetragonal	cubic	trigonal
Lattice constants (Å)	a = 7.62 c = 32.32	a = 10.77	a = 3.87 b = 9.16
Space group	$I4_1/amd$	$Fd\bar{3}m$	$P\bar{3}m1$
Band gap (eV)	2.1	-	-

2.3 Chapter references

- [1] E. Becquerel, *Annalen der Physik* **1841**, 130, 18-35.
- [2] E. Becquerel, *Annalen der Physik* **1841**, 130, 35-42.
- [3] P. Würfel, *Physik der Solarzellen*, 2 ed., Spektrum, Heidelberg, **2000**.
- [4] J. Nelson, *Physics of Solar Cells, Vol. 1*, **2007**.
- [5] D. Chapin, *J. Appl. Phys.* **1954**, 25, 676.
- [6] A. Goetzberger, C. Hebling, *Sol. Energy Mater. Sol. Cells* **2000**, 62, 1-19.
- [7] R. L. W. A.K. Hyder, G. Halpert, D.J. Flood, S. Sabripour, 1 ed., Imperial College Press, London, **2000**.
- [8] L. Kazmerski, National Renewable Energy Laboratory (NREL), <http://www.nrel.gov/>, **2010**, p. NREL compilation of best research solar cell efficiencies.
- [9] D. Carlson, *Appl. Phys. Lett.* **1976**, 28, 671.
- [10] M. Ghaffari, M. B. Cosar, H. I. Yavuz, M. Ozenbas, A. K. Okyay, *Electrochim. Acta* **2012**, 76, 446-452.
- [11] C. J. Brabec, N. S. Sariciftci, J. C. Hummelen, *Adv. Funct. Mater.* **2001**, 11, 15-26.
- [12] G. Yu, A. J. Heeger, *J. Appl. Phys.* **1995**, 78, 4510-4515.
- [13] M. Lenes, G.-J. A. H. Wetzelaer, F. B. Kooistra, S. C. Veenstra, J. C. Hummelen, P. W. M. Blom, *Adv. Mater. (Weinheim, Ger.)* **2008**, 20, 2116-2119.
- [14] M. A. Ruderer, R. Meier, L. Porcar, R. Cubitt, P. Mueller-Buschbaum, *J. Phys. Chem. Lett.* **2012**, 3, 683-688.
- [15] W. Wiedemann, L. Sims, A. Abdellah, A. Exner, R. Meier, K. P. Musselman, J. L. MacManus-Driscoll, P. Mueller-Buschbaum, G. Scarpa, P. Lugli, L. Schmidt-Mende, *Appl. Phys. Lett.* **2010**, 96, 263109/263101-263109/263103.
- [16] B. O'Regan, M. Graetzel, *Nature (London)* **1991**, 353, 737-740.
- [17] M. Graetzel, M. K. Nazeeruddin, B. O'Regan, *Switz.* **1991**, p. 39 pp.
- [18] M. Grätzel, *Nature* **2001**, 414, 338.
- [19] J. Weickert, C. Palumbiny, M. Nedelcu, T. Bein, L. Schmidt-Mende, *Chem. Mater.* **2011**, 23, 155-162.
- [20] Y. Xi, W. Z. Wu, H. Fang, C. G. Hu, *J. Alloys Compd.* **2012**, 529, 163-168.
- [21] A. Wisnet, M. Thomann, J. Weickert, L. Schmidt-Mende, C. Scheu, *J. Mater. Sci.* **2012**, 47, 6459-6466.
- [22] M. Rawolle, M. A. Niedermeier, G. Kaune, J. Perlich, P. Lellig, M. Memesa, Y.-J. Cheng, J. S. Gutmann, P. Muller-Buschbaum, *Chem. Soc. Rev.* **2012**, 41, 5131-5142.
- [23] J. M. Szeifert, D. Fattakhova-Rohlfing, D. Georgiadou, V. Kalousek, J. Rathousky, D. Kuang, S. Wenger, S. M. Zakeeruddin, M. Gratzel, T. Bein, *Chem. Mater.* **2009**, 21, 1260-1265.
- [24] I. Kaiser, K. Ernst, C. H. Fischer, R. Konenkamp, C. Rost, I. Sieber, M. C. Lux-Steiner, *Sol. Energy Mater. Sol. Cells* **2001**, 67, 89-96.
- [25] H. Lee, H. C. Leventis, S.-J. Moon, P. Chen, S. Ito, S. A. Haque, T. Torres, F. Nueesch, T. Geiger, S. M. Zakeeruddin, M. Graetzel, M. K. Nazeeruddin, *Adv. Funct. Mater.* **2009**, 19, 2735-2742.
- [26] M. Page, O. Niitsoo, Y. Itzhaik, D. Cahen, G. Hodes, *Energy Environ. Sci.* **2009**, 2, 220-223.
- [27] Y. Itzhaik, O. Niitsoo, M. Page, G. Hodes, *The Journal of Physical Chemistry C* **2009**, 113, 4254-4256.
- [28] R. Tena-Zaera, A. Katty, S. Bastide, C. Levy-Clement, B. O'Regan, V. Munoz-Sanjose, *Thin Solid Films* **2005**, 483, 372-377.

- [29] F. Lenzmann, M. Nanu, O. Kijatkina, A. Belaidi, *Thin Solid Films* **2004**, 451-452, 639-643.
- [30] W. Xuanzhi, *Solar Energy* **2004**, 77, 803-814.
- [31] V. Avrutin, N. Izyumskaya, H. Morkoç, *Superlattices Microstruct.* **2011**, 49, 337-364.
- [32] V. M. Fthenakis, H. C. Kim, E. Alsema, *Environ. Sci. Technol.* **2008**, 42, 2168-2174.
- [33] *All Minerals of the World*, M. o. Mineralogy, <http://www.musee.ensmp.fr/> 2012.
- [34] J. A. Hollingsworth, K. K. Banger, M. H. C. Jin, J. D. Harris, J. E. Cowen, E. W. Bohannon, J. A. Switzer, W. Buhro, A. F. Hepp, *Thin Solid Films* **2003**, 431, 63-67.
- [35] H. G. Grimm, A. Sommerfeld, *Zeitschrift für Physik A Hadrons and Nuclei* **1926**, 36, 36-59.
- [36] S. Abrahams, *J. Chem. Phys.* **1973**, 59, 5415.
- [37] J. E. Jaffe, A. Zunger, *Phys. Rev. B* **1984**, 29, 1882-1906.
- [38] S. K. Batabyal, L. Tian, N. Venkatram, W. Ji, J. J. Vittal, *J. Phys. Chem. C* **2009**, 113, 15037-15042.
- [39] D. Pan, L. An, Z. Sun, W. Hou, Y. Yang, Z. Yang, Y. Lu, *J. Am. Chem. Soc.* **2008**, 130, 5620-5621.
- [40] Y. Qi, Q. Liu, K. Tang, Z. Liang, Z. Ren, X. Liu, *J. Phys. Chem. C* **2009**, 113, 3939-3944.
- [41] W.-C. Huang, C.-H. Tseng, S.-H. Chang, H.-Y. Tuan, C.-C. Chiang, L.-M. Lyu, M. H. Huang, *Langmuir* **2012**, 28, 8496-8501.
- [42] H. Bihri, M. Abd-Lefdil, *Thin Solid Films* **1999**, 354, 5-8.
- [43] H. J. Muffler, C. H. Fischer, K. Diesner, M. C. Lux-Steiner, *Sol. Energy Mater. Sol. Cells* **2001**, 67, 121-127.
- [44] M. C. Zouaghi, T. Ben Nasrallah, S. Marsillac, J. C. Bernede, S. Belgacem, *Thin Solid Films* **2001**, 382, 39-46.
- [45] R. Scheer, I. Luck, M. Kanis, M. Matsui, T. Watanabe, T. Yamamoto, *Thin Solid Films* **2001**, 392, 1-10.
- [46] S. i. Kuranouchi, T. Nakazawa, *Sol. Energy Mater. Sol. Cells* **1998**, 50, 31-36.
- [47] T. Yukawa, K. Kuwabara, K. Koumoto, *Thin Solid Films* **1996**, 286, 151-153.
- [48] J. Möller, C. H. Fischer, H. J. Muffler, R. Könenkamp, I. Kaiser, C. Kelch, M. C. Lux-Steiner, *Thin Solid Films* **2000**, 361-362, 113-117.
- [49] P. Guha, D. Das, A. B. Maity, D. Ganguli, S. Chaudhuri, *Sol. Energy Mater. Sol. Cells* **2003**, 80, 115-130.
- [50] H. M. Pathan, C. D. Lokhande, *Appl. Surf. Sci.* **2004**, 239, 11-18.
- [51] Y. Shi, Z. Jin, C. Li, H. An, J. Qiu, *Appl. Surf. Sci.* **2006**, 252, 3737-3743.
- [52] S. Peng, F. Cheng, J. Liang, Z. Tao, J. Chen, *J. Alloys Compd.* **2009**, 481, 786-791.
- [53] C. Wen, X. Weidong, W. Juanjuan, W. Xiaoming, Z. Jiasong, L. Lijun, *Mater. Lett.* **2009**, 63, 2495-2498.
- [54] D. T. Cromer, K. Herrington, *J. Am. Chem. Soc.* **1955**, 77, 4708-4709.
- [55] W. H. Baur, *Acta Crystallogr.* **1961**, 14, 214-216.
- [56] T. Mitsushashi, O. J. Kleppa, *J. Am. Ceram. Soc.* **1979**, 62, 356-357.
- [57] D. W. Bahnemann, M. Hilgendorff, R. Memming, *J. Phys. Chem. B* **1997**, 101, 4265-4275.
- [58] Y. U. Ahn, E. J. Kim, H. T. Kim, S. H. Hahn, *Mater. Lett.* **2003**, 57, 4660-4666.
- [59] J. Aarik, A. Aidla, A.-A. Kiisler, T. Uustare, V. Sammelselg, *Thin Solid Films* **1997**, 305, 270-273.
- [60] K.-I. Jang, E. Hong, J. H. Kim, *Korean J. Chem. Eng.* **2012**, 29, 356-361.
- [61] A. Yildiz, S. B. Lisesivdin, M. Kasap, D. Mardare, *J. Non-Cryst. Solids* **2008**, 354, 4944-4947.
- [62] P. J. Cameron, L. M. Peter, *J. Phys. Chem. B* **2003**, 107, 14394-14400.

- [63] B. Peng, G. Jungmann, C. Jager, D. Haarer, H.-W. Schmidt, M. Thelakkat, *Coord. Chem. Rev.* **2004**, *248*, 1479-1489.
- [64] R. Mechiakh, S. N. Ben, R. Chtourou, R. Bensaha, *Appl. Surf. Sci.* **2010**, *257*, 670-676.
- [65] T.-Y. Cho, S.-G. Yoon, S. S. Sekhon, M. G. Kang, C.-H. Han, *Bull. Korean Chem. Soc.* **2011**, *32*, 3629-3633.
- [66] C.-y. Wang, H. Groenzin, M. J. Shultz, *J. Am. Chem. Soc.* **2005**, *127*, 9736-9744.
- [67] E. H. Roseboom, Jr., *Econ. Geol. Bull. Soc. Econ. Geol.* **1966**, *61*, 641-672.
- [68] L. A. Isac, A. Duta, A. Kriza, M. Nanu, J. Schoonman, *J. Optoelectron. Adv. Mater.* **2007**, *9*, 1265-1268.
- [69] D. J. Chakrabarti, D. E. Laughlin, *Bulletin of Alloy Phase Diagrams* **1983**, *4*, 254-271.
- [70] H. Fjellvag, F. Gronvold, S. Stolen, A. F. Andresen, R. Mueller Kaefer, A. Simon, *Z. Kristallogr.* **1988**, *184*, 111-121.
- [71] G. A. Harcourt, *Am. Mineral.* **1942**, *27*, 63-113.
- [72] N. V. Belov, Butuzov, V.P., *Doklady Akademii Nauk SSSR* **1946**, *54*, 717.
- [73] H. T. j. Evans, *Science* **1979**, *203*, 356-358.
- [74] K. Koto, N. Morimoto, *Acta Crystallographica B* **1970**, *26*, 915-924.
- [75] P. Lukashev, W. R. L. Lambrecht, T. Kotani, M. van Schilfgaarde, *Physical Review, Serie 3. B - Condensed Matter* **2007**, *76*, 195202-195201-195202-195214.
- [76] T. B. Massalski, J. L. Murray, L. H. Bennett, H. Baker, *Binary alloy phase diagrams*, American Society for Metals, **1986**.
- [77] G. A. Steigmann, H. H. Sutherland, J. Goodyear, *Acta Crystallographica* **1965**, *19*, 967-971.
- [78] N. Barreau, S. Marsillac, D. Albertini, J. C. Bernede, *Thin Solid Films* **2002**, *403-404*, 331-334.

3 Synthesis and characterization methods

To understand the diverse properties like morphology, chemical composition and optical and electrical behavior of the synthesized thin films and nano materials various characterization methods are used. To investigate the crystal phase X-ray diffraction experiments (XRD) were done. The optical properties are investigated via UV-Vis spectroscopy and for the average chemical composition inductively coupled plasma mass spectrometry and energy dispersive X-ray spectroscopy (EDX) in the scanning electron microscopy (SEM) was applied. To characterize the morphology a SEM was used. Transmission electron microscopy (TEM) and its analytical techniques were applied for detailed characterization of the crystal structure and size as well as the average and local chemical composition. In the following chapter, the synthesis methods and characterization techniques used in this work are described.

3.1 Solvothermal synthesis

To obtain CuInS_2 thin films on fluorine doped thin oxide (FTO) substrates three different synthesis methods were tested in this work. Chemical bath deposition (CBD), successive ionic layer adsorption reaction (SILAR) method and solvothermal reaction were applied. Hereby the latter leads to the most promising results.

The solvothermal synthesis method is nowadays widely used for treatment and synthesis of different materials.^[1] Solvothermal reactions are defined as heterogenic chemical reactions in a liquid medium above the boiling point at pressures exceeding 1 bar. To achieve these conditions they are usually performed in sealed autoclaves. If the used solvent is water the synthesis is called hydrothermal. Reactants usually show a better solubility under hydrothermal/solvothermal conditions, because of the action of mineralizers or solvents. Depending on the reaction conditions and materials, different types of reactions can be realized, like crystal growth, synthesis of new phases or stabilization of complexes. Furthermore, materials that are complicated to obtain by other techniques can be synthesized with this method, e.g. low temperature phases of materials like α -quartz or metastable compounds like Te_2I . The big advantage of solvothermal synthesis, compared to other conventional methods for fabrication of materials, is the fact that less energy is needed to produce

solid state materials from liquid solution, compared to other methods which use e.g. the vapor phase. For example materials like chalcogenides or chalcogenid halides and oxidic or sulfidic thin films like ZnO, TiO₂, PbS, CuS, In₂S₃ or CuInS₂ can be produced by the solvothermal method.^[2-5] Hereby a controlled microstructure and chemical composition can be obtained at temperatures below 200 °C which is much lower than the temperature needed for common chemical or physical deposition methods. Publications showed over the last years that different morphologies of CuInS₂ can be realized just by varying the growth conditions such as growth temperature and the molar ratio of Cu/In. By employing a solvothermal procedure, nanoparticles ^[6], nanorods ^[7], foam-like nanocrystallites ^[8], quantum dots ^[9], and porous microspheres ^[10] of CuInS₂ have been synthesized.

For the description of the synthesis, the used solutions are generally considered as thermodynamically ideal what means that they behave like a mixed ideal gas with no interactions between the molecules in the solution. The relation between temperature T , pressure p , volume V and the amount of molecules n for ideal gases is given by the ideal gas law, where R is the gas constant:

$$pV = nRT \quad (3.1)$$

The equation shows that an increase in temperature at constant volume leads to an increase of the pressure in the system. Consequently, it is possible to reach certain regions in the particular phase diagram by heating the system at constant volumes. Higher temperatures also lead to an increase of the inner energy U which is given for ideal gases by:

$$U = \frac{3}{2}nRT \quad (3.2)$$

In most cases the hydrothermal reaction initializes enough energy for the synthesis before the critical point of the solvent is reached. But the suitable reaction parameters, temperature and pressure, which provide a high enough energy for overcoming the reaction barriers as well as an increased solubility of the materials, have to be found. ^[1, 11-13]

3.2 Sol-gel method

To obtain TiO₂ thin films on FTO substrates, the sol-gel method was used. To deposit the TiO₂ films the sol-gel solution was spin coated on the substrate.

Sol describes a colloidal solution of particles or macromolecules, with a diameter of about 1-100 nm. Through aggregation of the particles a network is formed. The resulting gel is a two-phase semisolid which can easily be deformed by external influences. The network consists of a polymer compound with long chains or branches which comprise a liquid, e.g. water. In the first step of the sol gel technique the starting materials have to be dissolved in a suitable solvent. For this work metal complexes are used as precursor to form a colloidal product. Generally, three different reaction types are distinguished: hydrolysis, alcohol condensation and water condensation.^[14] These types are shown in the reaction equation summarized in Figure 3.1.

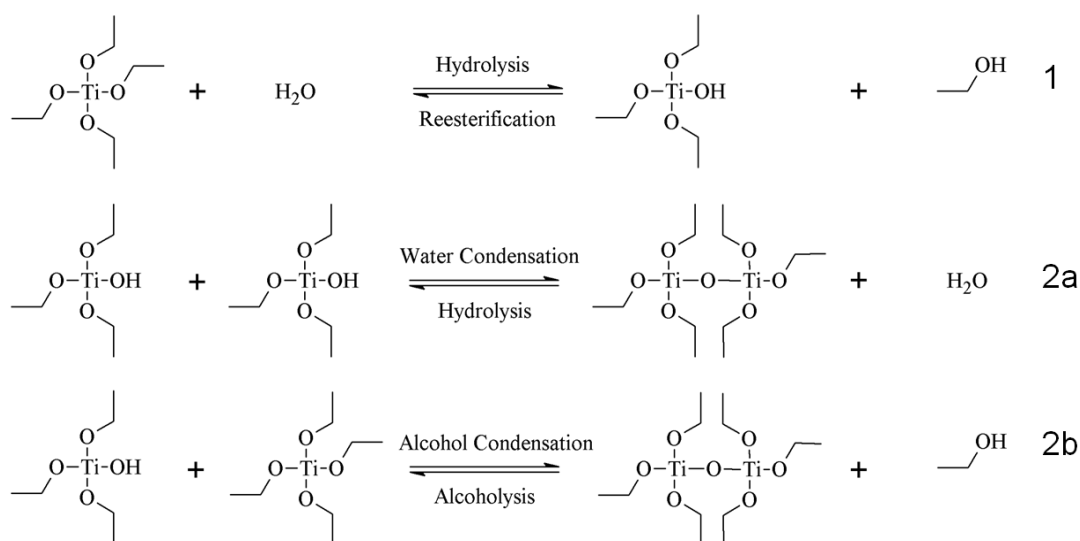


Figure 3.1: Reaction equation of the three different reaction types, hydrolysis (1), alcohol condensation (2a) and water condensation (2b) distinguished during the sol-gel reaction.

During the hydrolysis mechanism the alkoxide groups at the metal center are replaced by water. During the subsequent condensation reaction (2a+2b) the metal-oxygen-metal-bondings are formed, in doing so at first oligomers and polymers are formed. In water free solution the condensation reactions are reversible; the bindings

between the oligomeres are random. In general, the condensation reaction begins before the hydrolysis is completed. This can be influenced with the variation of $H_2O:Ti$ ratio, the pH-value or catalysts. Water and alkoxide are not mixable. Therefore alcohol is used as homogenization reagent. After drying of the gel amorphous structures are obtained which can crystallize by calcination.^[15, 16] The acid catalyzed sol-gel mechanism used in this work is given in Figure 3.2.

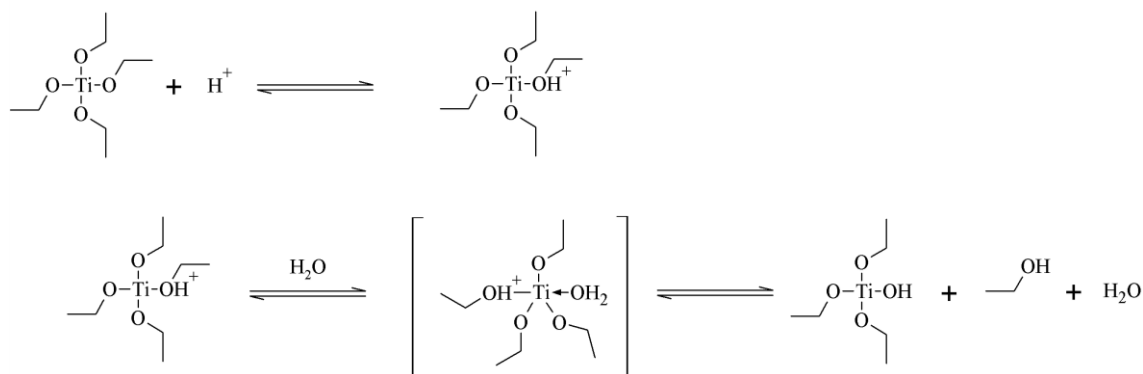


Figure 3.2: Acid catalyzed sol-gel mechanism used in this work.

Hereby an alcohol ligand will be protonated in a first fast step causing the withdrawal of the metal centre electron density and thus an increase of the electrophilicity occurs. The behavior of the water leads to the formation of a fivefold coordinated transition state. Subsequently, an alcohol ligand splits off. Acid catalyzed sol-gel reactions have a fast hydrolysis time and long gelation times, while in contrast base catalyzed reactions have slow hydrolysis times and a fast condensation reaction. Acid and base catalyzed reactions are defined by the isoelectric point of the product.^[16, 17]

3.3 X-ray diffraction

X-rays are a type of electromagnetic radiation with a wavelength between 0.1 and 100 Å exhibiting a high energy. In 1895 Wilhelm Conrad Röntgen first discovered X-rays and was therefore awarded the Nobel Prize in Physics in 1901.

With X-ray diffraction (XRD), it is possible to investigate phase composition and crystal structure of solids. Hence, it is one of the most fundamental analytical techniques in research fields like solid state chemistry and material science.

In a common XRD setup, X-rays are generated in a high vacuum tube. Therein, a focused electron beam, accelerated from the cathode by high voltage, collides with the

anode metal (such as Cu or Mo). This leads to emission of X-rays. The spectrum comprises the so called “Bremsstrahlung” and characteristic X-rays. The latter result when the incident electron beam excites inner shell electrons to unoccupied states and when these relax back to their ground states. The energy difference of these two energy states of the transferred electrons is emitted as X-ray photon. The intensity and wavelength of the X-rays are dependent on the target material, since the energy difference between the electron shells in different elements is varying.

Through the application of different metal filters, a collimator and a monochromator, an intense part of the spectrum, is selectively isolated, usually K_{α} radiation. These characteristic X-rays with well defined wavelength is then used for XRD experiments. The interaction between the X-rays and the specimen results in different secondary effects, for example, absorption, scattering and reflection. The XRD diffraction process is based on scattering. In 1912 Max von Laue discovered the diffraction of X-rays by single crystals. He found that diffraction maxima occur in particular directions which depend on the crystal structure and the wavelength. The structure determination is carried out by interpretation of the diffraction maxima. These are caused by constructive interference of X-rays scattered at in the ordered atomic arrangement in a crystal.

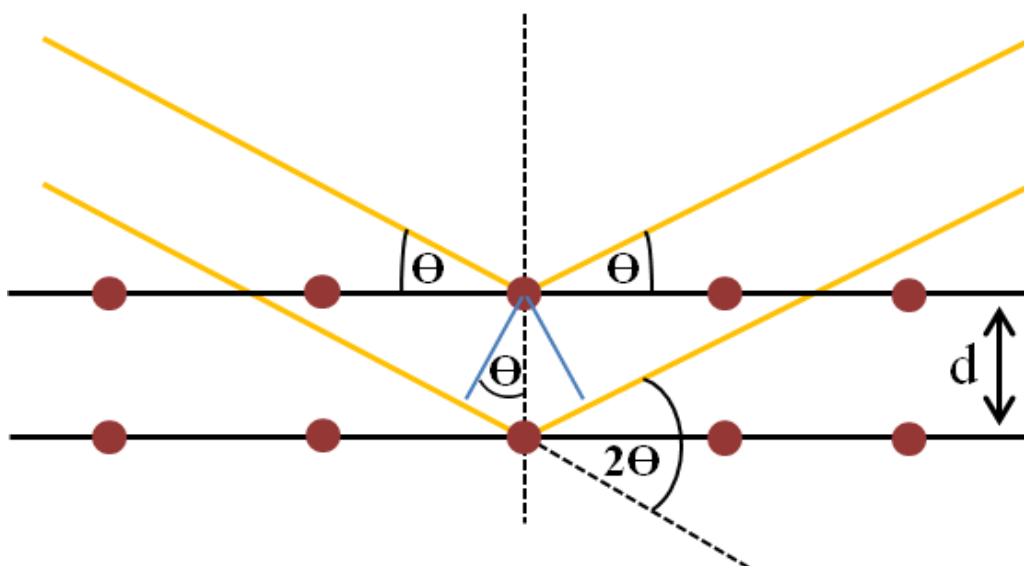


Figure 3.3: Schematic illustration of the Bragg relation.

The condition for constructive interference is given by the Bragg equation (Figure 3.3):

$$n\lambda = 2d_{hkl} \sin \theta \quad (3.3)$$

where n is the order of diffraction, λ the wavelength of the X-rays, d_{hkl} the distance of the lattice planes and θ the Bragg angle.

A XRD measurement allows the calculation of the distance of the lattice planes d_{hkl} in the crystal, where hkl are the Miller indices. The obtained diffraction patterns can be compared to databases from literature.

For XRD patterns of polycrystalline samples like thin films or powder the average crystal size can be obtained from the peak broadening of the diffraction peaks. The Scherrer equation correlates the crystal size to full width of the diffraction peak at half maximum (FWHM). Thereby, the domain size τ can be calculated via

$$\tau = \frac{K\lambda}{\beta \cos \theta} \quad (3.4)$$

where K is the shape factor approximated to 0.9 for spherical shape, λ is the X-ray wavelength, β is the line broadening at the half-maximum intensity in rad, and θ is the Bragg angle.^[13, 18-20]

3.4 UV-Vis spectroscopy

Spectral photochemical analysis is based on the measurements of light absorption in the range of visible (Vis) and ultraviolet (UV-) radiation of materials in dependence of the wavelength. The light absorption is generated by electron transitions between different states in the molecule or solid. The Lambert-Beer law describes the relation between the concentration of the absorbing material, the path length and the intensity of the transmitted light and is given by

$$A = -\log \frac{I}{I_0} = \epsilon cd \quad (3.5)$$

where A is the absorbance, I_0 the intensity of incoming light, I the intensity of transmitted light, ε the extinctions coefficient, c the concentration of absorbing material and d the thickness of the absorbing material.

In order to excite an electron from an occupied (HOMO) to an unoccupied (LUMO) orbital in a molecule or from the valence band to the conduction band in a solid, the absorbed photon must have an energy matching to the energy difference of the two energy levels. Via the equation

$$E = h\nu = \frac{hc}{\lambda} \quad (3.6)$$

the wavelength of the absorbed photons can be calculated. Hereby is E the energy, h the Planck constant, c the speed of light, ν the frequency and λ the wavelength. For materials with smaller band gap, for example semiconductors, the exiting of electrons in the conduction band is easier and therefore they show often high absorption.^[13, 21]

3.5 Inductively coupled plasma atomic emission spectrometry

The inductively coupled plasma atomic emission spectrometry (ICP-AES) is a common, qualitative and quantitative analytical method which is able to detect metals and some non metals at a very low concentration in the range of nano gramm per liter. By this method the fact that excited atoms are emitting electromagnetic radiation is used. With a high frequent stream of argon plasma, the sample will be heated up to 5000-10000 °C. Hereby a high-frequency generator coupled with a magnetic field is used to generate a small area with extremely high energy density. Thereby, the substances are atomized and excited. The resulting radiation will be conducted through a monochromator to detect the for each element characteristic wavelength.^[21]

3.6 Electron microscopy

Electron microscopy is a useful technique to reveal the micro- and nanostructure of materials. Electrons are used to irradiate the specimen and to produce a magnified image. In an electric field, electrons can be accelerated. The kinetic energy of an electron in an electric field and its velocity v , are related to the acceleration voltage U and is given by:

$$E_{kin} = \frac{1}{2} m_e v^2 = eU \quad (3.7)$$

$$v = \sqrt{\frac{2eU}{m_e}} \quad (3.8)$$

In this nonrelativistic approximation, e is the elementary charge and m_e is the mass of the electron. The wave-particle duality postulates that all particles exhibit both wave and particle properties and the de Broglie equations relates the wavelength λ to the momentum p , and velocity v . Together with the equation above one obtains:

$$\lambda = \frac{h}{p} = \frac{h}{m_e v} = \frac{h}{\sqrt{2m_e e U}} \quad (3.9)$$

where h is the Planck constant.

Electron microscopes have a much higher resolution than light-powered optical microscopes. Electrons have wavelengths about 100,000 times shorter than visible light and can achieve a theoretical resolution of about 0.1 Å. Whereas conventional, non-confocal light microscopes are limited by diffraction to approximately 200 nm resolution. With good electromagnetic lenses and lens aberration corrected microscopes, atomic resolution is possible.

There are several signals which can be generated when an incident electron beam interacts with a sample. These are summarized in Figure 3.4. They can be backscattered or secondary electrons or Auger electrons and X-rays can be emitted. Additionally, the electrons can be elastically or inelastically scattered. These different signals are used either for imaging, diffraction experiments or for analytical studies as described in the following.^[22, 23]

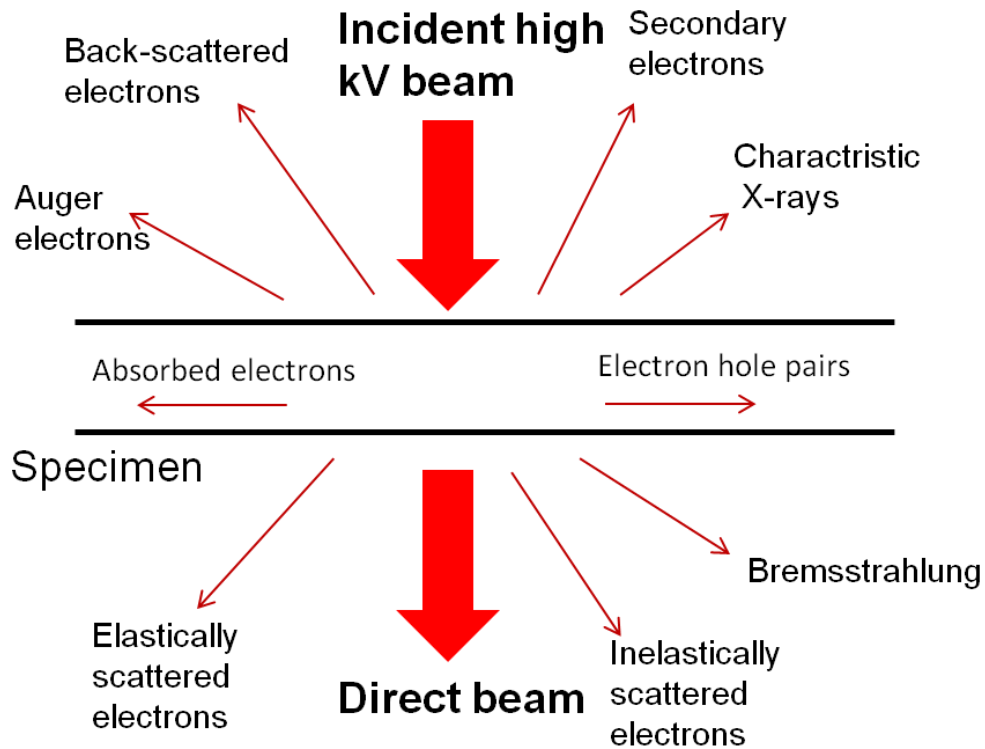


Figure 3.4: Generated signals from interaction between incident electron beam and a thin specimen. Image modified from Williams and Carter.^[22]

3.6.1 Scanning electron microscopy

The scanning electron microscope (SEM) is primarily used to study the surface, or near surface structure of bulk specimens. Figure 3.5 shows a schematic diagram with the main components and the mode of operation of a SEM.

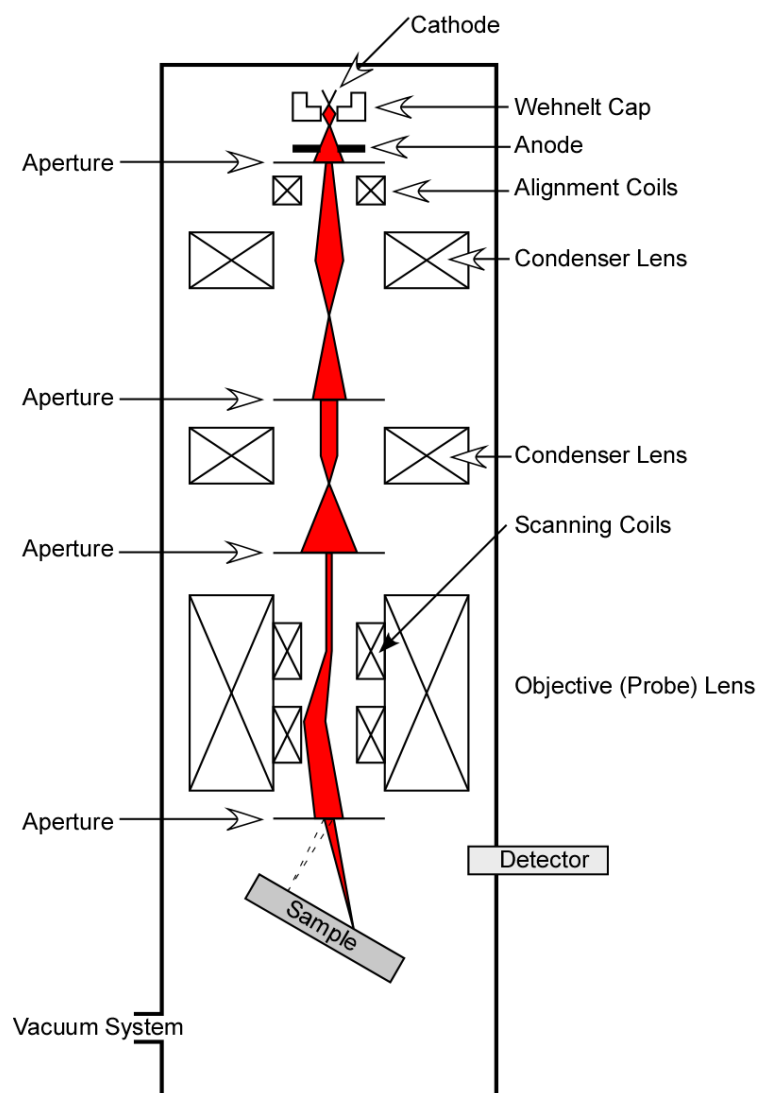


Figure 3.5: Schematic diagram of a scanning electron microscope.^[24]

Conventional SEMs have thermionic guns, for which tungsten or lanthanum hexaboride (LaB_6) cathodes are normally used. The LaB_6 cathode is heated up to 1400 K and electrons are released from the surface by overcoming the work function. The electrons are accelerated to an energy which is usually between 1 keV and 30 keV. Two or three condenser lenses are focusing the electrons to a beam with a diameter of 2 - 10 nm. The fine electron beam is scanned across the specimen by the scanning

coils. A detector counts the number of low energy secondary electrons, or back scattered electrons, emitted or scattered from each point of the surface. Secondary electrons detected through an Everhart-Thornley detector stem from the surface region and are used to study the morphology of the sample. Back-scattered electrons detected by semiconductor devices have a large escape depth and are used to visualize the phase distribution of the specimen. They are sensitive to the atomic number.^[19, 23]

3.6.2 Focused ion beam microscopy

In a focused ion beam (FIB) microscope a high energy-ion beam is focused on the specimen. The ion beam is generated in a liquid metal field-evaporation source, which is maintained at a high positive potential. Usually, gallium is used, which has a very low melting point (~ 30 °C). A liquid Ga film is wetting a tungsten needle and forming a Taylor cone. Due to an extraction voltage, the ions are emitted. The generated ions are accelerated to an energy of 1-50 keV and electrostatic lenses are used to focus the beam and to raster it on the surface of the specimen. When the Ga⁺-ion beam interacts with the specimen surface it sputters the material. The primary beam also produces secondary electrons. The signals from the sputtered ions or secondary electrons are collected to form an image. Using higher primary currents, material can be removed faster by sputtering, allowing precision milling of the specimen down to a sub-micrometer level. This process is called micro-machining. Dual-beam FIB instruments are available which integrate a field-emission electron source in addition to an ion-beam source, in separate optical columns. The scanning electron microscope column is usually mounted vertically above the sample, and the ion beam source and column are attached at an inclined angle to the sample chamber (see Figure 3.6). Such an instrument can be used for example for characterization and micro-machining. The dual-beam FIB microscopes are also used to prepare thin-film sections and lamellas for TEM characterization.^[19]

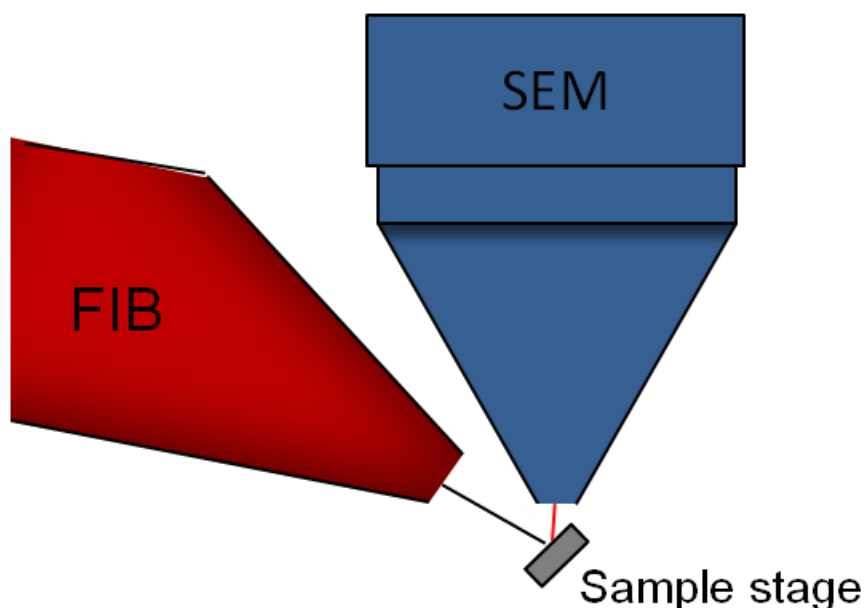


Figure 3.6: Schematic of a dual-beam configuration with respect to the sample stage.^[19]

3.6.3 Transmission electron microscopy

In a transmission electron microscope (TEM) an electron beam transmitted through a very thin specimen is responsible for imaging. The magnified image is formed by the interaction of the electrons transmitted through the specimen. The optical path in a TEM is shown in Figure 3.7. At the top of the instrument the electron beam is created in the electron gun. Different electron sources like thermal emitters (for example tungsten filament or a LaB_6 -crystal as described in chapter 2.6.1) or thermally assisted field emission guns (Schottky field emitter) are used. In a Schottky emitter a high electrical field is applied to the tip and due to this the work function is reduced. Electrons can then overcome the barrier at lower temperatures. If the electrical field is high enough, electrons can also tunnel from the tip to the vacuum. This field effect is often assisted by using an elevated temperature. The wavelength of the generated electron beam depends on the acceleration voltage (between 80 and 300 kV). Below the electron gun the condenser lens system is located. With the condenser lens the electron beam is demagnified and its diameter is controlled. Hereby the intensity of the illumination and the convergence angle of the beam can be adjusted. Below the condenser, the specimen is located. An ultra thin specimen with a diameter of 3 nm is held precisely between the pole pieces of the objective lens. The objective lens is needed to form the first intermediate image which is subsequently enlarged by intermediate and projector lenses. Alternatively, the diffraction pattern obtained in

the back focal plane of the objective lens can be magnified by changing the strength of the intermediate lens. The image or diffraction pattern is projected on a fluorescent screen or a CCD camera.

Contrast mechanism

In a TEM different contrast mechanism can be used. Within the specimen electrons are elastically and inelastically scattered. Elastic scattered electrons which leave the object under the same angle are focused in the back focal plane of the objective lens. A diffraction pattern is formed at that plane. With the objective aperture all electrons which have been scattered by any mechanism can be stopped. If the objective aperture is centered around the optical axis, a bright background can be seen in absence of a specimen. This is called bright field imaging. Thicker sample areas and regions with higher density in the specimen will be scattered more strongly and appear darker in the image. The so originated contrast is called mass contrast. In crystalline specimens an additional contrast mechanism can occur, the so called diffraction contrast. Here the electron beam undergoes Bragg scattering. As mentioned above electrons scattered within the same angle are focused in the back focal plane. By the placement of the objective aperture in the back focal plane the desired Bragg reflections can be selected (or excluded). If the central beam is used for imaging, a bright field image is formed. If the objective aperture is shifted to select one reflection, an off-axis dark field image is formed. If the incident beam is tilted and the Bragg reflected beam is parallel to the optical axis, an on-axis dark field image is obtained. In these images a region will appear dark wherever no sample scattering to the selected direction is present, as such a region without a specimen will appear dark.^[20, 22, 23]

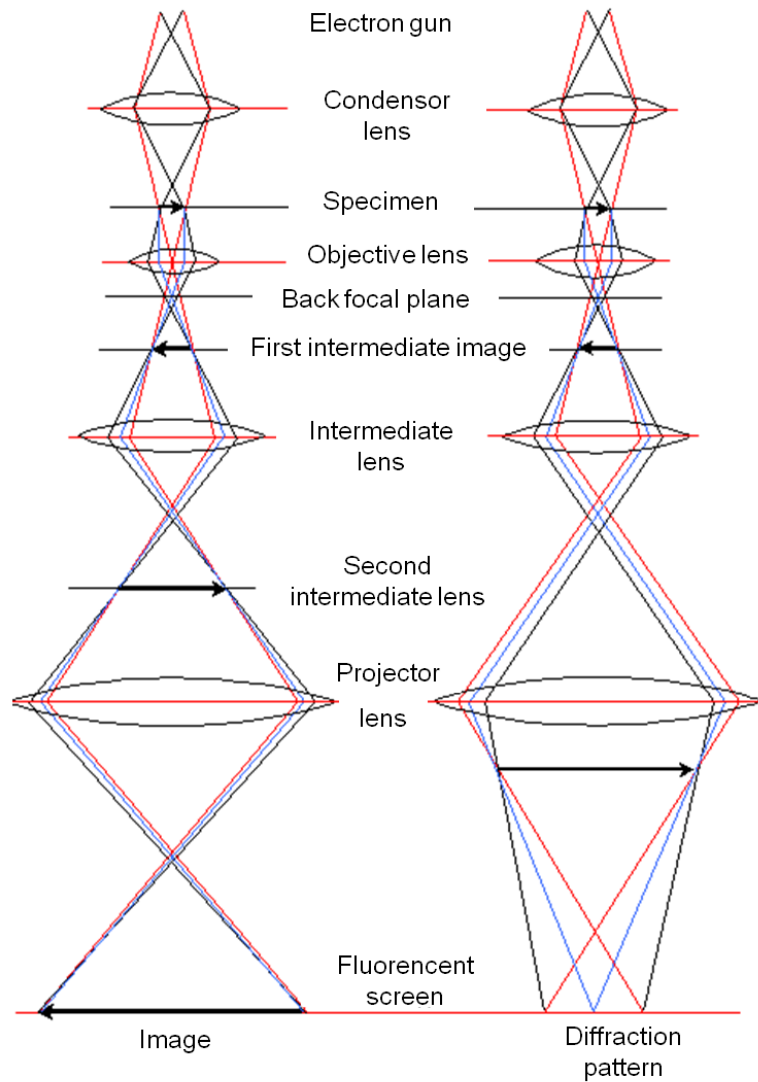


Figure 3.7: Optical path in a TEM.^[25]

Electron diffraction

A diffraction pattern is formed in the back focal plane of the objective lens. The first projector lens (or intermediate or diffraction lens) can be switched from the image mode, where the lens is focused on the image plane, to diffraction mode, at which the lens is focused on the back focal plane of the objective lens and the diffraction pattern is projected and magnified by the projector lenses to the viewing screen. The obtained diffraction pattern can be analyzed with the effective camera constant of the system which can be calibrated by using standards such as Si single crystals. The following equation is used to calculate lattice spacings d_{hkl} :

$$\lambda L = R d_{hkl} \quad (3.10)$$

Here λL is the camera constant, R the measured distance on the image in units of pixel or length. Selected area diffraction apertures in different sizes can be used to select a small area of the specimen.^[20, 22]

High resolution TEM

High resolution TEM (HRTEM) is an imaging method which allows illustration of the periodicity of the crystallographic structure of a specimen with atomic resolution and is therefore a common tool to characterize nanostructures in crystalline materials like oxides and metals. With novel chromatic and spherical aberration corrected microscopes, details finer than 0.1 nm can be distinguished. The contrast in HRTEM images is generated by phase differences which arise from the interference in the image plane of the electron wave with itself. The contrast transfer function (CTF) is a function of aberration in imaging optics in electron microscopy and is given by:

$$CTF(u) = \sin(C_s \lambda^3 u^4 \frac{\pi}{2} + \pi \Delta f \lambda u^2) \quad (3.11)$$

where C_s is the spherical aberration coefficient, λ is the electron wavelength, u is the spatial frequency and Δf is the defocus. The point resolution is defined as the point when the CTF has the first zero crossing. Up to this frequency, there is no contrast inversion in the image. The focus where the point resolution is maximal is called Scherzer-defocus and is given by $\Delta f = -(\lambda C_s)^{1/2}$.^[22]

The objective lens transfer function is given by $T(u) = A(u)E(u)2\sin\chi$, Whereby $A(u)$ is the aperture function and $E(u)$ the envelope function. $T(u)$ is plotted against u [nm^{-1}] in Figure 3.8. The defocused value Δf is -58 nm. The curve has been calculated with $C_s = 1.0$ mm and 200 kV acceleration voltage.^[22]

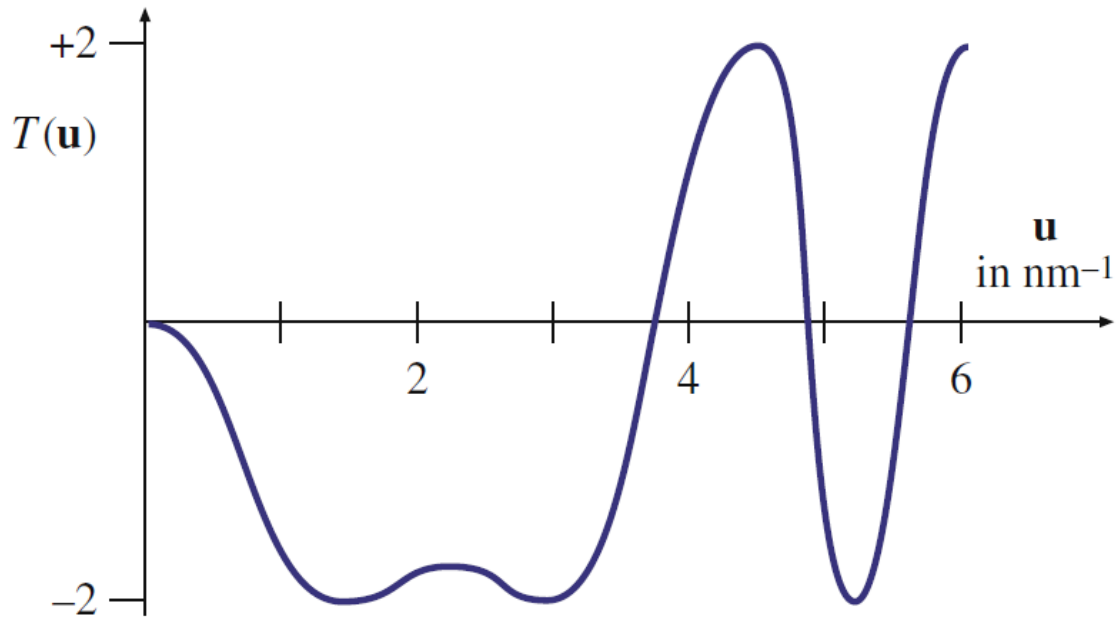


Figure 3.8: Contrast transfer function.^[22]

Scanning TEM

The first scanning transmission electron microscope (STEM) was constructed by Manfred von Ardenne in 1937 - 1938 in Berlin. Nowadays, modern TEMs allow the utilization as STEM and are called TEM/STEM. In a scanning transmission electron microscope, different from the conventional TEM, a convergent electron beam is formed and this small spot is scanned over the sample in a raster. Figure 3.9 shows a schematic drawing of a STEM instrument.

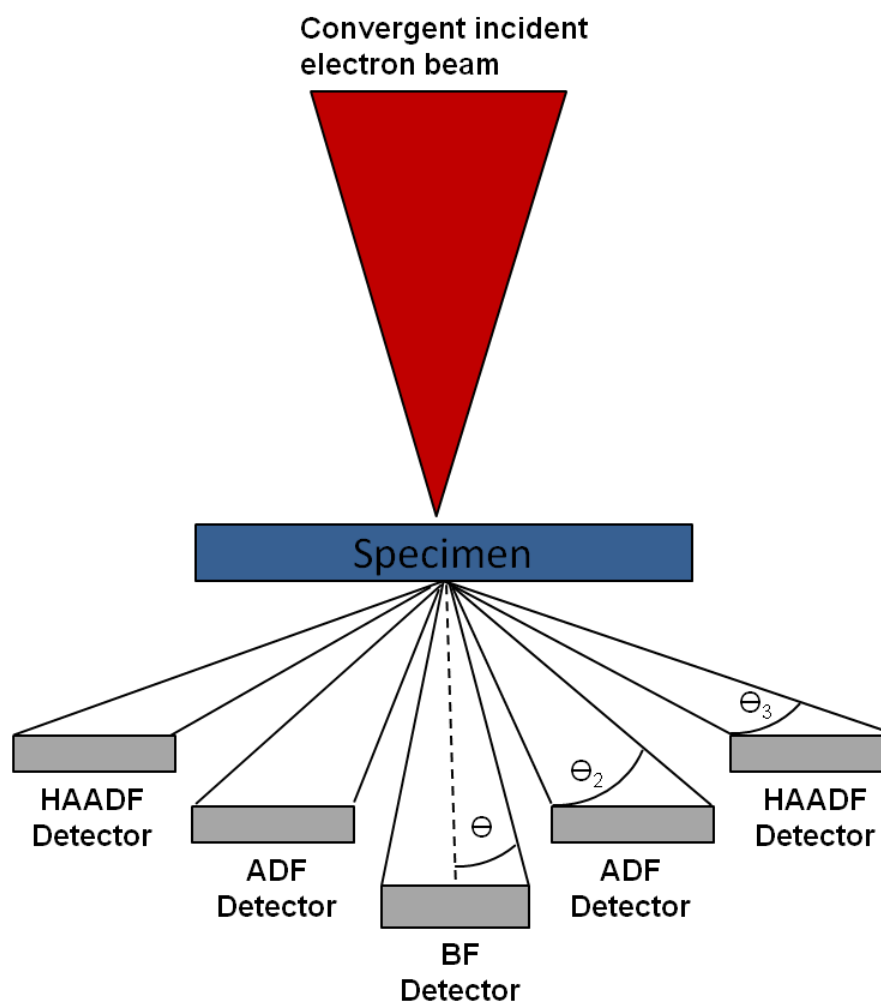


Figure 3.9: Schematic diagram of detector in a STEM instrument. Modified from D. Brandon and W. D. Kaplan.^[19]

A series of lenses is used to focus the electron beam to a probe which is directed to a thin, electron transparent specimen. Scan coils are used to scan the probe over the specimen in a raster. A multitude of scattered signals can be detected and plotted as a function of probe position to get a magnified image. Transmitted electrons which leave the sample at angles smaller or equal to the incident beam convergence angle (typically 10 – 25 mrad) are used to obtain images in bright field mode. Electrons that leave the sample at high angle (several times the incident beam convergence angle e.g. between 25 and 150 mrad) are imaged in annular dark field (ADF) or high angle annular dark field (HAADF) mode (larger than 50 mrad). The dark field detectors are usually centered around the optical axis of the microscope. The HAADF signal enables the distinction of chemical elements in the sample by the signal intensity, because the scattering of the appropriate angle range is nearly proportional to the square of the atomic number.^[26]

3.7 Energy dispersive X-ray spectroscopy

Energy dispersive X-ray spectroscopy (EDX) in the electron microscope has become an important tool for elemental analysis or chemical characterization for all types of solid material. Its application for detection and quantification of light elements is limited and usually elements below atomic numbers of 11 (Na) or 5 (B) (depending on the detector) cannot be quantified because parts of the detector absorbs low energy X-rays (< 1 KeV). This spectroscopic method can be realized in SEM as well as in TEM. The bombardment of a material with high energy electrons will result in the emission of characteristic X-rays, whose wavelengths depend on the nature of the atoms in the specimen. For the emission of the characteristic X-rays, an atom has to be excited. Thereby an electron from an inner shell will be knocked out. This state is instable and the empty state will be filled up from a more energy-rich electron from an outer shell. At this relaxation the energy difference can be released as a characteristic X-ray quant. This process is shown in Figure 3.10.

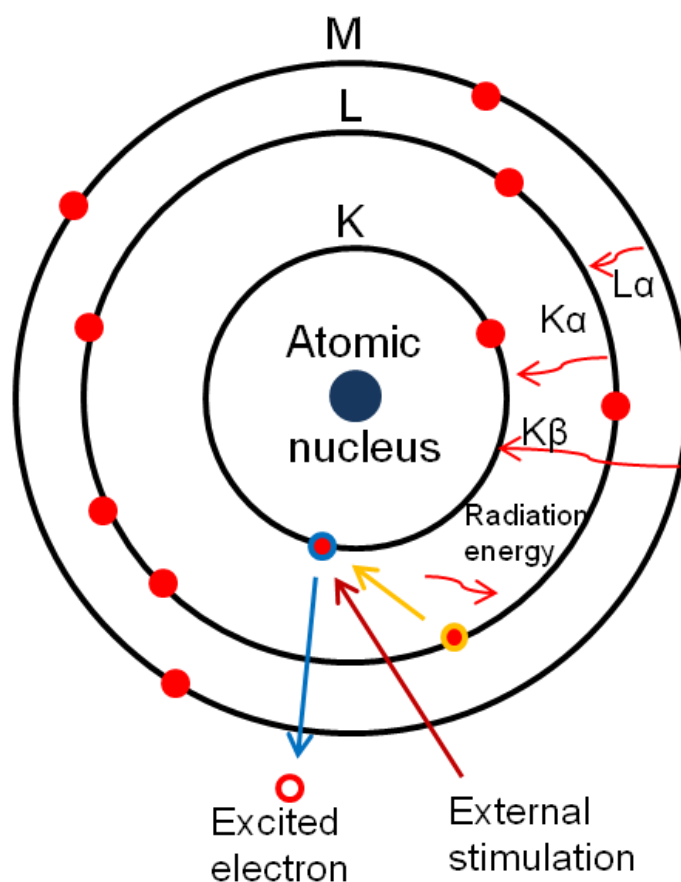


Figure 3.10: Schematic of the relaxation of an inner-shell-excited atom.

The formed X-ray radiation is characteristic for the transition and each element. For one element more transitions are allowed. Depending from which shell the more energy-rich electron is coming and in which unoccupied inner shell state it goes. The created X-rays are identified as for example K_{α} , K_{β} or L_{α} according from which shell the electron was excited and from which shell the electron fills the empty state (see Figure 3.10). The wavelength of this X-ray can be calculated with the following equation:

$$\lambda = \frac{hc}{\Delta E} \quad (3.12)$$

hereby h is the Planck constant, c the speed of light and ΔE the energy difference of the states involved.

Additionally, the electrons get decelerated by the coulomb field of the atomic nucleus which results in “Bremsstrahlung” as mentioned already in chapter 3.3. The Bremsstrahlung forms the background of the EDX spectrum. For thin specimens, quantification is possible by using the Cliff-Lorimer equation which is given by:

$$\frac{C_A}{C_B} = k_{AB} \frac{I_A}{I_B} \quad (3.13)$$

C_A and C_B are the concentrations of the element A and B, I_A and I_B is the intensity of the peaks of element A and B and k_{AB} is the Cliff-Lorimer factor which depends on the involved elements and the used EDX/TEM/SEM.^[19, 22, 27]

3.8 Electron energy loss spectroscopy

Electron energy loss spectroscopy is an analytical method which can be performed in the TEM and which is used for the chemical and electronic characterization of inorganic and organic materials. As mentioned above the electron beam interacts with the specimen leading to elastical and inelastic scattering. The resulting spectrum shows the intensity of the transmitted electrons as function of their energy loss. Inelastic interactions include phonon excitations, inter and intra band transitions, plasmon excitations and inner shell ionizations. An electron energy loss spectrum consists of three parts, the zero-loss peak at 0 eV which mainly contains electrons that still have the original beam energy E_0 . For example, they have only interacted elastically or not at all with the specimen. The zero loss peak also contains inelastic interactions with very low energy loss (i. e. phonons) which cannot be distinguished. At the low-loss region until 50 eV the spectrum is dominated by plasmon oscillations. In the area of the core-loss region (> 50 eV) inelastic processes especially excitation of electrons from the inner shell (K, L, M,..) in unoccupied states (ionization) occur. The edges in the spectrum are characteristic for an element. Thus, EELS is complementary to X-ray spectroscopy, and it can be utilized for qualitative and quantitative element analysis. In particular, the detection of light elements is a main task of EELS.^[28]

3.9 TEM sample preparation

Conventional TEM sample preparation

By using the conventional TEM cross sample preparation method two pieces of the same films are glued together with an epoxy glue to get the following layer order: substrate | film | glue | film | substrate. With a diamond saw, small pieces of about 2.1 mm in width were cut out from this stack. Subsequently, this sandwich will be embedded again with epoxy glue in a brass tube with an inner diameter of about 2.4 mm. With the diamond saw, discs with a thickness of about 200 μm are cut and ground to a thickness of 60 to 80 μm . With a dimple grinder a cavity is grounded from both sides so that the discs have a thickness of 20 μm in the center. Finally, a hole is created with an ion polishing system by an argon ion beam. The acceleration of the

beam is between 0.3 and 4 keV and it is hitting the sample at angles between 4 and 5° until a small hole is created. The edges of this hole are then electron transparent and can be investigated in the TEM. Typically values for electron transparency are below 100 nm.^[29] In Figure 3.11 the different steps of the TEM cross section preparation are diagrammed.^[19]

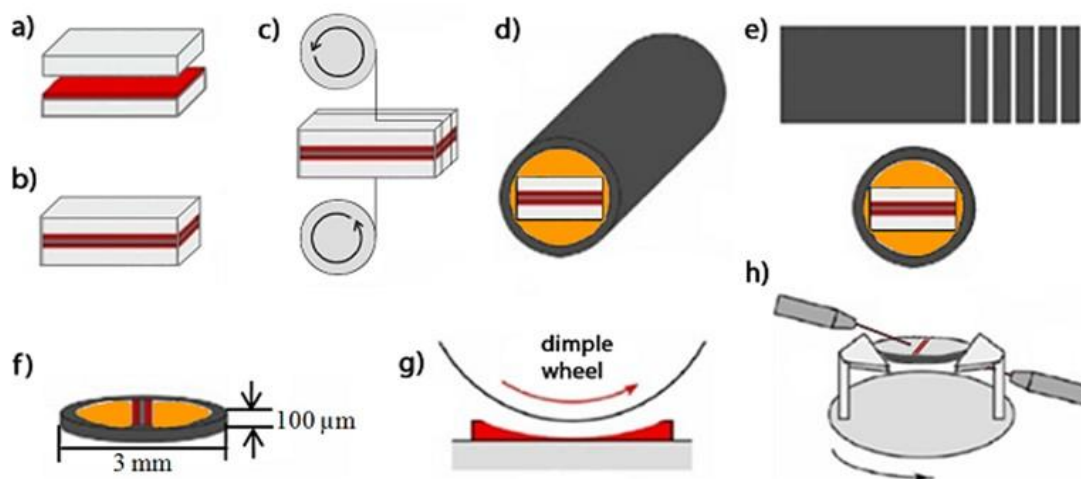


Figure 3.11: Schematic diagram of the working steps of the TEM cross section sample preparation. Gluing of the films (a, b), cutting of the sandwiches to the right size (c), gluing the sandwich in a brass tube (d), cutting of slices and grinding (e, f), grinding a cavity/dimpling(g) und ion milling (h).^[19]

To prepare TEM samples for the investigation of for example nanoparticles the dropping method can be used. Here, the material will be dissolved in a solvent, for example ethanol. The solution is dropped on a Cu, Au or Ni TEM grid with a diameter of 3 mm exhibiting for example 200 meshes which are coated by a holey carbon film (see Figure 3.12). The material of interest stays on the carbon film deposited on the grid and the solvent is evaporated. This method can also be used for the investigation of film material. In that case, the material can be scratched from the substrate and deposited on the TEM grid.

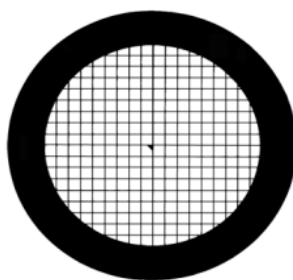


Figure 3.12: TEM grid with a diameter size of 3 mm consisting of 200 meshes and coated with a holy carbon film (not visible).

TEM sample preparation with FIB

Cross section TEM samples can be also prepared by focused ion beam milling. The working principle of this instrument is described in 2.3.2. The sample is viewed using the integrated SEM in the dual-beam instrument. Then an interesting region of the sample is selected. A protective coating of carbon or platinum is deposited on the sample surface to avoid surface damage by the high-energy ions. Two trapezoids, on either side of the selected region are milled into the sample while the sample is tilted to 45°. A lamella with the typical size of 2 x 20 x 5 μm is separated. Then the lamella is cut free of the surface by the ion beam except of one edge. A nano-manipulator consisting of a sharp tungsten needle is now inserted. Then a gas-injector needle is inserted, and either platinum or carbon is deposited assisted by the electron- or ion-beam to attach the tungsten needle to the lamella. The lamella is then being cut completely free from the substrate with the ion beam. Afterwards it is transferred to a TEM grid, which is located within the vacuum chamber on a special stub. The TEM grid is usually a 3 mm diameter half-ring consisting of copper or nickel as shown in Figure 3.13. The lamella is moved next to the grid and platinum or carbon is now deposited to attach the lamella to the TEM grid. Ion milling is used to remove the affiliation between the sample and the nano-manipulator needle. Ion-thinning of the $\sim 2 \mu\text{m}$ thick lamella is performed to reach the required specimen thickness of around 70 nm.^[19]

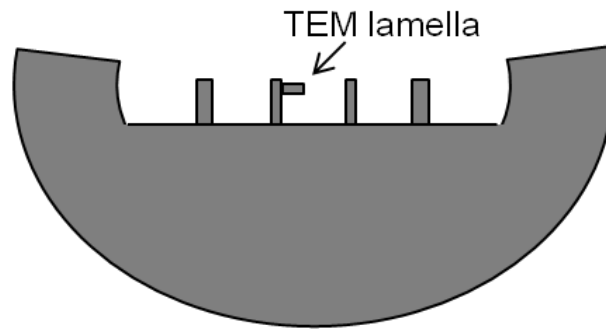


Figure 3.13: Schematic drawing of a 3 mm diameter half-ring, used for mounting a thin TEM specimen lamella in the FIB TEM sample preparation.

3.10 Chapter references

- [1] K. Byrappa, M. Yoshimura, M. Haber, *Handbook of Hydrothermal Technology: A Technology for Crystal Growth and Materials Processing*, 1 ed., Noyes Publication, New York, **2001**.
- [2] M. Yoshimura, *J. Mater. Res.* **1998**, *13*, 796-802.
- [3] F. Jia, Z. Yao, Z. Jiang, *Int. J. Hydrogen Energy* **2012**, *37*, 3048-3055.
- [4] J. Liu, D. Xue, *J. Cryst. Growth* **2009**, *311*, 500-503.
- [5] H.-T. Liu, J.-S. Zhong, B.-F. Liu, X.-J. Liang, X.-Y. Yang, H.-D. Jin, F. Yang, W.-D. Xiang, *Chin. Phys. Lett.* **2011**, *28*.
- [6] S. Han, M. Kong, Y. Guo, M. Wang, *Mater. Lett.* **2009**, *63*, 1192-1194.
- [7] J. Xiao, Y. Xie, R. Tang, Y. Qian, *J. Solid State Chem.* **2001**, *161*, 179-183.
- [8] G. Z. Shen, D. Chen, K. B. Tang, Z. Fang, J. Sheng, Y. T. Qian, *J. Cryst. Growth* **2003**, *254*, 75-79.
- [9] J. Feng, J. Han, X. Zhao, *Prog. Org. Coat.* **2009**, *64*, 268-273.
- [10] Y. Qi, K. Tang, S. Zeng, W. Zhou, *Microporous Mesoporous Mater.* **2008**, *114*, 395-400.
- [11] E. Riedel, C. Janiak, *Moderne Anorganische Chemie*, 2 ed., Gruyter, Berlin, **2007**.
- [12] L. Smart, *Einführung in die Festkörperchemie*, 1 ed., Vieweg, Berlin, **1995**.
- [13] P. W. Atkins, J. Paula, *Physikalische Chemie*, 4 ed., Wiley, Weinheim, **2006**.
- [14] O. Lev, M. Tsionsky, L. Rabinovich, V. Glezer, S. Sampath, I. Pankratov, J. Gun, *Anal. Chem.* **1995**, *67*, 22A-30A.
- [15] G. R. Lee, J. A. Crayston, *J. Mater. Chem.* **1994**, *4*, 1093-1100.
- [16] C. J. Brinker, *J. Non-Cryst. Solids* **1988**, *100*, 31-50.
- [17] R. Aelion, A. Loebel, F. Eirich, *J. Am. Chem. Soc.* **1950**, *72*, 5705-5712.
- [18] W. Massa, *Kristallstrukturbestimmung*, 7 ed., Vieweg&Teubner, Wiesbaden, **2011**.
- [19] D. Brandon, W. Kalpan, *Microstructural Characterization of Materials*, 2 ed., Wiley, Weinheim, **2008**.
- [20] B. Fultz, J. Howe, *Transmission Electron Microscopy and Diffractometry of Materials*, 3 ed., Springer, Berlin, **2009**.
- [21] G. Schwedt, *Analytische Chemie*, Wiley-VCH, Weinheim, **2008**.
- [22] D. B. Williams, B. C. Carter, *Transmission Electron Microscopy*, 2 ed., Springer, New York, **2009**.
- [23] P. J. Goodhew, J. Humphreys, R. Beanland, *Electron Microscopy and Analysis*, 1 ed., Taylor & Francis, London, **2001**.
- [24] G. Dehm, J. Howe, J. Zweck, *In-situ Electron Microscopy, Applications in Physics, Chemistry and Materials Science*, 1 ed., Wiley-VCH, Weinheim, **2012**.
- [25] *Transmission electron microscopy*, E. Tarhan, **2004**, <http://www.mete.metu.edu.tr/pages/tem/TEMtext/TEMtext.html> (Department Metallurgical and Materials Engineering, METU) 7.11. 2012.
- [26] S. J. Pennycook, P. D. Nellist, *Scanning Transmission Electron Microscopy*, 1 ed., Springer, New York, **2011**.
- [27] J. Goldstein, D. Newbury, D. Joy, C. Lyman, E. Echlin, E. Lifshin, L. Sawyer, J. Michael, *Scanning Electron Microscopy and X-Ray Microanalysis*, 3 ed., Springer, New York, **2003**.
- [28] R. Brydson, *Electron Energy Loss Spectroscopy*, 1 ed., Taylor & Francis, **2001**.
- [29] A. Strecker, U. Salzberger, J. Mayer, *Prakt. Metallogr.* **1993**, *30*, 482-495.

4 Experimental details

In the following chapter the used chemicals and substrates, the used synthesis methods as well as the used equipments are described.

4.1 Chemicals and substrates

In Table 4.1 the used chemicals and substrates are summarized.

Table 4.1: Used chemicals and substrates.

Chemicals/Substrates	Supplier
Ethanol	Merck, 99,9%
FTO substrate	Pilkington
Indium(III)-Chloride, InCl_3	Sigma-Aldrich, 98%
Chlorbenzol	VWR-International Merck
Coppersulfate-Pentahydrate, $\text{CuSO}_4 \cdot 5 \text{H}_2\text{O}$	Riedel-deHaën, puriss
L-Cysteine	Sigma-Aldrich, $\geq 98\%$
Phenyl-C61-butansäure-methylester, PCBM	Solenne, 99%
Nitric acid, HNO_3	VWR-International Merck, concentrated
Hydrochloric acid, HCl	VWR-International Merck
Silver conductive varnish	ACHESON Silver DAG 1415 G3692
Tetraorthoethyltitanate, $\text{Ti}(\text{OEt})_4$	Sigma-Aldrich, $\geq 98\%$
Tetrahydrofurane THF	VWR-International Merck
Thioacetamide, $\text{C}_2\text{H}_5\text{NS}$	Sigma-Aldrich, $> 99,0\%$

4.1.1 Synthesis of Copperindiumdisulfide

For the synthesis of the CuInS_2 a solvothermal synthesis route adapted from Peng et al.^[1] was used. CuInS_2 films were deposited on fluorine-doped tin oxide (FTO) conductive glass (Pilkington) with a size of $15 \times 30 \times 2 \text{ mm}^3$ was used as substrate for the deposition of films. The FTO substrate was washed in diluted nitric acid, acetone, double-distilled water and ethanol in an ultrasonic cleaner for 5 min in each case. In a Teflon-lined stainless steel autoclave (20 mL) $\text{CuSO}_4 \cdot 5\text{H}_2\text{O}$, InCl_3 and $\text{C}_2\text{H}_5\text{NS}$ or L-cysteine as sulfur source were dissolved in 10 mL ethanol and stirred for 15 min. The cleaned substrate was placed diagonally, with the FTO surface pointing downwards, in the Teflon liner. The autoclave was closed and heated for different times and temperatures (150 - 200 °C). The samples were either quickly cooled down to room temperature by immediately placing the hot autoclave in a water bath after heating or cooled down on to room temperature without water bath. The obtained colored black or brownish films on FTO were washed afterward using double-distilled water and ethanol. For the synthesis of CuInS_2 microsphere $\text{CuSO}_4 \cdot 5\text{H}_2\text{O}$, InCl_3 and $\text{C}_2\text{H}_5\text{NS}$ was used as precursors. The same reaction conditions were used as described above. Just no substrate was placed in the autoclave. The obtained black product was filtered, washed with ethanol and dried on air.

4.1.2 Synthesis of Titaniumdioxide

FTO conductive glass (Pilkington) with dimension of $20 \times 15 \times 2 \text{ mm}$ was used as substrate for the deposition of the TiO_2 films. The FTO was cleaned in a solution of one part extrane and five parts double-distilled water in an ultrasonic bath for 15 min. Afterwards, a second wash cycle was done with ethanol again for 15 min in the ultrasonic bath. After cleaning, the substrates were dried with compressed air and treated in an O_2 -plasma cleaner. For the synthesis of the TiO_2 layers, a high diluted tetrahydrofurane (THF) sol-gel solution was prepared. Therefore 0.186 ml concentrated hydrochloric acid was given to 0.275 ml tetraorthoethyltitanate during stirring. The incurred sol-gel solution was diluted with 3.5 ml THF. For the deposition of the TiO_2 layers on the cleaned FTO substrates a spin coater was used. Hereby 0.130 mL of the prepared sol.gel solution was given on the FTO substrates. The spin coating parameters were 3000 rpm for 1.5 min for thinner films or 1500 rpm for 1.5 min for thicker films.

After spin coating the layers were calcinated in an oven at 450 °C for different dwell times (0.5 – 5 h).

4.2 Equipment

Equipment applied in this work is summarized in Table 4.2.

Table 4.2: Used equipment.

Diamond saw	<i>Precision Vertical Diamond Wire Saw, Model 3242 from WELL</i>
Dimple Grinder	Model 656 von <i>GATAN</i> Diamond paste with 5 micron, and 0,25 micron (for polishing)
Disc Grinder	Model 623 von <i>GATAN</i>
Dual focused ion beam und scanning electron microscope (SEM/FIB)	<i>ZEISS NVISION 40</i> SEM used at 2,5 keV FIB used at 30 keV and 1,5 pA
Ion miller	<i>Precision Ion Polishing System from GATAN</i>
Inductively coupled plasma atomic emission spectrometry (ICP-AES)	<i>VARIAN VISTA RL CCD Simultaneous ICP-AES</i>
Ovens	<i>MEMMERT</i> oven (Model UM400) KENDRO LABORATORY PRODUCT, type Heraeus (Model T6030)
SEM	<i>JEOL JSM-6500F</i> Equipped with an EDX spectrometer from OXFORD INSTRUMENTS INCA ENERGY

TEM	<i>FEI Titan</i> Operated at 80 – 300 kV acceleration voltage Equipped with an EDX spectrometer from EDAX, a HAADF-detector from <i>FISCHIONE INSTRUMENTS</i> (Model 3000) for STEM and an Tridiem Electron Energy Loss Spectrometer (EELS) detector from GATAN
UV-Vis spectrometer	<i>HITACHI U-3501</i> spectrophotometer
UV-Vis spectrometer	<i>PERKIN ELMER 330</i> spectrophotometer
XRD	<i>D8 DISCOVERY</i> from <i>BRUKER</i>

Chapter reference

- [1] S. Peng, F. Cheng, J. Liang, Z. Tao, J. Chen, *J. Alloys Compd.* **2009**, 481, 786-791.

5 Synthesis and characterization of CuInS₂ thin film structures

This chapter is based on the following publication:

Angela S. Wochnik, Christoph Heinzl, Florian Auras, Thomas Bein, Christina Scheu.
Journal of Material Science **2011**, 47 (4), 1669-1676.

5.1 Introduction

The development of alternative solar cell concepts such as extremely thin absorber cells leads to a high interest in new semiconductor materials for photovoltaic applications. Semiconducting ternary chalcogenide compounds of the type I-III-VI₂ seem to be promising candidates to meet the demands of light absorbers in high efficiency thin film solar cells because of their excellent optical and electrical properties. The chalcopyrite semiconductor CuInS₂ has, next to a good long-term stability, a high absorption coefficient ($>10^5 \text{ cm}^{-1}$) and a direct band gap of 1.53 eV which allows utilization of much of the solar spectrum.^[1] Another advantage of CuInS₂ is that by changing the molar ratio of Cu/In an n-type or p-type semiconductor can be achieved^[2] CuInS₂ nanostructures have been synthesized via several manufacturing methods as for example elemental chemical vapor deposition,^[3] spray pyrolysis^[4], sulfurization of metallic precursors,^[5] electro deposition,^[6] co-evaporation,^[7] and ion layer gas reaction.^[8] Besides these cost-intensive methods which often require expensive equipment, new approaches involving facile and low cost reactions are attracting increasing attention. Techniques such as chemical bath deposition^[9, 10], successive ionic layer adsorption and reaction^[11] and mild solvothermal synthesis routes^[12] have been successfully applied to synthesize CuInS₂. Publications appearing over the last few years show that various morphologies of Cu-InS₂ can be realized just by varying the growth conditions such as growth temperature and the molar ratio of Cu/In. By employing a solvothermal procedure, nanoparticles,^[13] nanorods,^[14] foam-like nanocrystallites,^[15] quantum dots,^[16] and porous microspheres^[17] of Cu-InS₂ have been synthesized. Due to its versatile

applicability and simplicity, we also chose a solvothermal reaction route ^[12] in order to prepare CuInS₂ films with different nano-morphologies.

Most of the characterization methods applied in the literature to study CuInS₂ films were X-ray diffraction (XRD), scanning electron microscopy (SEM), and energy dispersive X-ray spectroscopy (EDX) in the SEM as well as UV/Vis and Raman spectroscopy. These methods can determine average characteristics but do not allow one to study individual nanostructures. As the structure and chemical composition of the films at the nanoscale are expected to have a strong impact on their electronic, optical, and mechanical properties, we focused our work on the detailed analysis of the morphology, growth, and spatially resolved chemical composition analysis of the various nanostructures. To this end, we use advanced transmission electron microscopy (TEM) techniques such as high resolution TEM (HRTEM) and scanning TEM (STEM). EDX measurements in STEM-mode allow us to differentiate even small spatial deviations in the chemical composition at the nanometer scale.

In this study, we present a modified solvothermal reaction procedure to synthesize homogeneous films with thicknesses down to 200 nm which is based on the synthesis route of Peng et al.^[12] Compared to the previously reported film thicknesses of several microns^[12] the resulting films appear to be well suited for applications in thin film solar cells.

5.2 Experimental

Fabrication of CuInS₂ films

All chemical reagents were of analytical grade and used without further purification. Fluorine-doped tin oxide (FTO) conductive glass (Pilkington) with dimension of 15 x 30 x 2 mm³ was used as substrate for the deposition of the CuInS₂ films. The FTO was washed in diluted nitric acid, acetone, double-distilled water and ethanol in an ultrasonic cleaner for 5 min in each case. Two films, hereafter referred to as film A and film B, were prepared. The general reaction procedure to grow the films was adapted from Peng et al.^[12] (film A); for the second film B we modified the concentration of reactants as well as the heating process. In a Teflon-lined stainless steel autoclave (20 ml) CuSO₄·5H₂O (A: 0.03 M, B: 0.01 M), InCl₃ (A: 0.03 M, B: 0.01 M), and C₂H₅NS

(A: 0.12 M, B: 0.03 M) were dissolved in 8 ml ethanol and stirred for 15 min. The cleaned substrate was placed diagonally, with the FTO surface pointing downwards, in the Teflon liner. The autoclave was closed and heated with different programs. Film A was obtained by heating at 160 °C for 12 h followed by cooling down to room temperature. In the case of sample B, the heating temperature was reduced to 150 °C whereas the heating time was increased to 24 h. This sample was quickly cooled down to room temperature by immediately placing the hot autoclave in a water bath after heating. The obtained colored (A: black, B: brownish) films on FTO were washed afterward using double-distilled water and ethanol.

5.3 Characterization

For the characterization of the films, various analytical techniques were applied. For the determination of the crystal structure of the thin films, XRD patterns were obtained on a Bruker D8 Discovery diffractometer with CuK α radiation ($\lambda = 1.54 \text{ \AA}$). The scanning rate was 0.05°/s and the 2 θ range was chosen from 20° to 65°. The obtained patterns were compared to literature data. The full width of half maximum of the peaks were estimated using the Bruker software EVA, which is based on an integral and statistical approach and which does not take into account the specific shape of the peaks. For general morphology investigations and the determination of the overall chemical composition a Jeol JSM-6500F scanning electron microscope operated at 4.0 kV and equipped with an energy dispersive X-ray detector from Oxford Instruments (Inca Energy) was used. Secondary electron (SE) images were acquired using the implemented Jeol standard detector. SEM top view and cross section samples were prepared using conventional preparation techniques. TEM investigations were done using a FEI Titan 80–300 (S)TEM microscope equipped with a Gatan Tridiem image filter and an EDAX EDX detector for analytical measurements. The Titan can be operated between 80 and 300 kV. A high angle annular dark field (HAADF) detector from Fischione Instruments (Model 3000) is attached to the microscope for STEM imaging. Standard TEM samples were obtained by scratching the film off the substrate and placing it on a holey carbon coated gold grid. Cross sectional TEM specimens were prepared as described by Strecker et al.^[18]. To reduce beam damage effects, some of the TEM investigations were done at 80 kV. The electron diffraction data were evaluated using a calibrated camera constant obtained by

using a Si standard. The UV/Vis absorption of the films was measured at room temperature on a Hitachi U-3501 spectrophotometer. Aside from cross sectional investigations in the SEM, the film thickness was quantified with a profilometer of the type Dektak 150 from Veeco. The average chemical composition of the films was also analyzed via inductively coupled plasma atomic emission spectrometry (ICP-AES) using a VARIAN VISTA RL CCD Simultaneous ICP-AES.

5.4 Results and discussion

SEM and XRD investigation of CuInS₂ films

For the general morphology investigation of the CuInS₂ films we used SE for imaging. Figure 5.1 shows an overview of the different morphologies and thicknesses of the two differently synthesized films where the concentrations, heating times and cooling procedure were varied.

Film A grows in a sphere-like structure and consists of several 3 μm thick crystal spheres (Figure 5.1(a)). The higher magnification top view SE image reveals that these balls consist of numerous individual flakes. From the crosssection SE image in Figure 5.1(b) the film thickness is estimated to be about 25 μm in accordance with the results of the profilometer. The inset displays that the film shows three different regions. Close to the FTO substrate the film is densely packed. On that layer a 1 μm thick flaky structure can be observed on which the crystal spheres are located. Figure 5.1(c) shows an SEM top view image of film B. The SE image reveals a net-like structure, which is again formed by individual flakes. The SEM cross-section image (Figure 5.1(d)) indicates that this structure is similar to the layer at film A close to the FTO substrate. The film is densely packed, while in the upper region a flaky structure occurs (compare to inset in Figure 5.1(b)). The total thickness of this film B is around 400 nm which was also confirmed by profilometer measurements.

We also fabricated films having different thicknesses ranging from 200 nm to 3.5 μm , various flake structures (smaller and bigger flakes) and different flake distances depending on the synthesis parameters. All of them show the occurrence of different regions/layers within the film, i.e., starting with a dense layer close to the FTO substrate, followed by flakes which are, for thicker films, covered by crystalline spheres.

CuInS₂ films possessing a similar sphere-like structure as film A were reported by Peng

et al.^[12] Compared to their results, our films grow in different layers and show more homogeneity and higher density of the spheres by using a lower concentration of the reactants. These differences might arise from a different cleaning process of the substrate in the ultrasonic bath, different substrate size or dissimilar immersion depths of the substrate in the reaction solution.

Both films show a high surface area and therefore a high potential interface density. This fact is especially beneficial for solar cell applications, since there is a large area available for separation of electron-hole pairs when the material is combined with a suitable electron conductor.

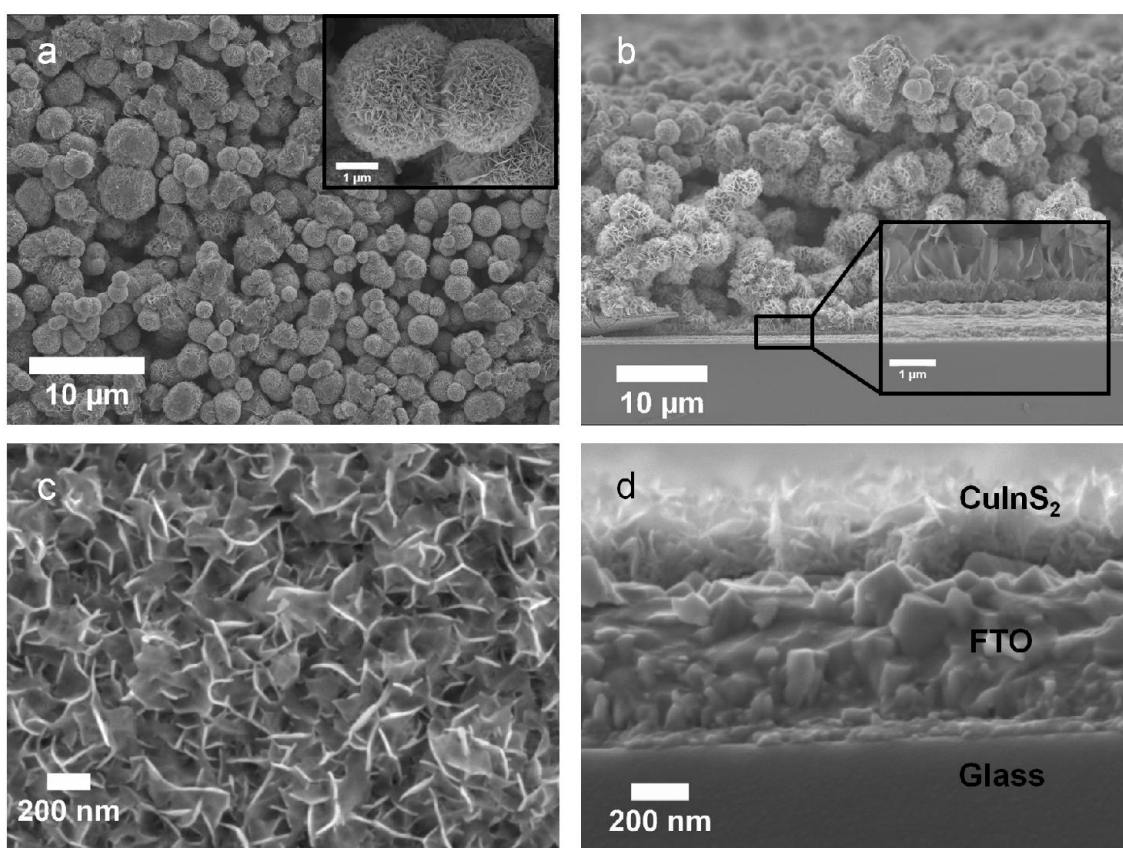


Figure 5.1: SE images of CuInS₂ films deposited on FTO. (a) shows the top view and (b) shows the cross-section of film A, while (c) and (d) show the top view and cross-section of film B.

The average chemical composition of the films was measured using EDX in the SEM. Figure 5.2 displays an EDX spectrum of film A. Only Cu, In, and S are detected and no additional peaks indicating impurities were observed. The quantification leads to 25 ± 1 at.% Cu, 25 ± 1 at.% In and 50 ± 1 at.% S. Thus, a stoichiometric composition of Cu:In:S = 1:1:2 was found.

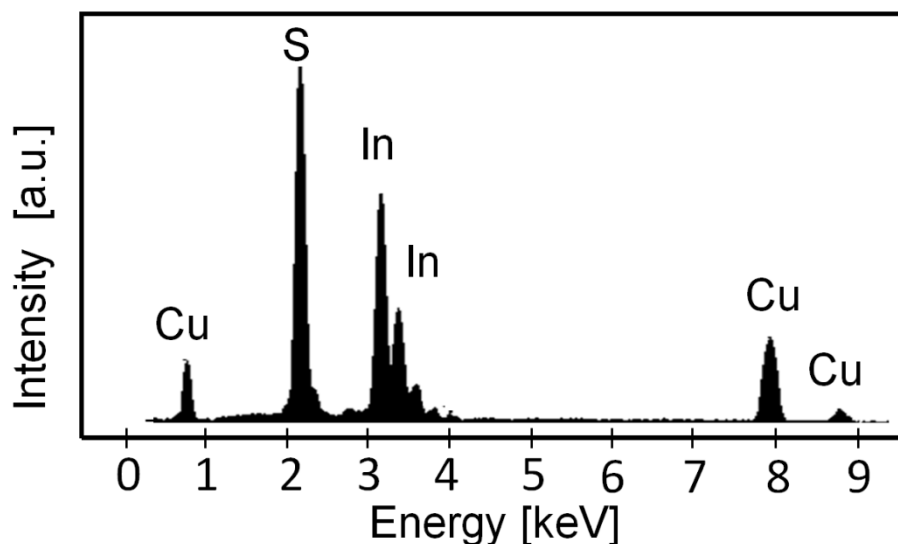


Figure 5.2: EDX spectrum of film A measured in the SEM showing the presence of Cu, In, and S. The quantification reveals a stoichiometric composition of Cu:In:S of 1:1:2. No impurities were observed.

The global crystal structure of the films was investigated by XRD measurements. Figure 5.3 shows the XRD pattern of film A with the characteristic reflections of CuInS₂ in the roquesite structure. This tetragonal crystal type has lattice parameters $a = 0.552$ nm and $c = 1.112$ nm. The obtained reflexes are (112), (220), and (312), all additional reflections originate from the FTO substrate (Figure 5.3). No further reflections can be observed indicating that no major amount of side products like copper and indium sulfides or their oxides have formed. However, an asymmetric peak broadening is observed at the (112) reflection, with a tail at lower 2θ values. In a recent work of Dejene^[19], who studied Cu(In,Ga)(Se,S)₂ thin films with large conglomerated μm sized grains, also asymmetric peak broadening was observed which was attributed to a gradient in composition and associated structure changes. The structure changed from Cu(In,Ga)Se₂ on the surface to Cu(In,Ga)S₂ at the substrate. In our case, the asymmetry is only observed for the (112) reflection. We fitted this asymmetric peak using two pseudo-Voigt functions and determine with that the position of the two overlapping peaks leading to the asymmetric shape. This revealed lattice plane distances of 0.319 and 0.330 nm, respectively. The first value corresponds to the (112) lattice plane spacing of CuInS₂. The second value can be attributed to the FTO substrate or to various copper sulfide phases. Thus, the XRD data suggest that, if at all, only a small amount of a minor phase such as copper sulfide has formed.

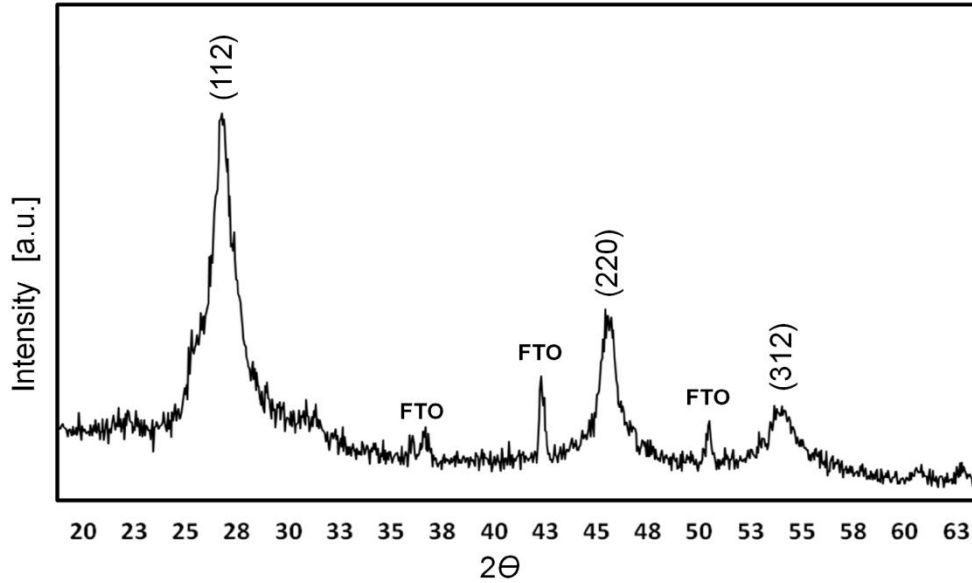


Figure 5.3: XRD pattern of film A revealing the tetragonal roquesite crystal structure.

Despite that the (112) CuInS₂ peak is asymmetric, all peaks observed in the XRD pattern are also rather broad indicating that small crystal sizes occur in the film structures. These were analyzed by applying the Scherrer equation using the most intense peak of the [112] reflection occurring at a 2θ value of 27.9° . The full width of half maximum amounts to 1.25° (0.022 rad). With this value, the average thickness τ of flat crystallites can be estimated by

$$\tau = \frac{K\lambda}{\beta \cos \theta}$$

where K is the shape factor approximated to 0.9, λ is the X-ray wavelength ($\text{CuK}\alpha$), β is the line broadening at the half-maximum intensity in rad, and θ is the Bragg angle. The calculations resulted in an average thickness τ of flat crystallites of 7 nm which is in good agreement with the TEM investigation described later. The XRD patterns acquired with film B also revealed the characteristic reflections of CuInS₂ for the roquesite structure (not shown). No side products or formation of oxides was detected although a small amount of copper sulfides cannot be fully excluded. TEM investigation of CuInS₂ films TEM was used for the determination of the crystal structure and the chemical composition on the nanometer scale. The bright field (BF) image in Figure 5.4(a) and the HAADF-STEM image in Figure 5.4(b) show the densely packed layer with a thickness of 600 nm and the flaky structure in the lower region of film A, close to the substrate (see inset). The film is delaminated from the substrate probably because of the TEM sample

preparation process. In the image various rods can be observed that grow out of the dense layer. Furthermore it can be seen that the rods are surrounded by individual flakes which seem to grow out from branch-like structures. EDX spectra were taken in STEM-mode with a spot of about 1 nm on individual parts of the specimen. The quantification of the EDX spectra that were taken at the rods resulted in 25 ± 2 at.% Cu, 25 ± 2 at.% In, and 50 ± 2 at.% S (Figure 5.4(c)). This is close to a stoichiometric composition of Cu:In:S: 1:1:2. The quantification of the EDX spectra taken from the flakes gives 24.4 ± 1.7 at.% Cu, 25.2 ± 1.6 at.% In, 50.4 ± 2.5 at.% S, and also results in a stoichiometric composition. The EDX data taken from the densely packed layer reveal a non-stoichiometric composition which is rich in Cu. The quantification results in 30 ± 2 at.% Cu, 19 ± 2 at.% In, and 52 ± 2 at.% S. As pointed out by Yukawa et al.^[2], the conductivity type is changing with deviations from the stoichiometric composition, being n-type for the In-rich region and p-type for the Cu-rich region. In the same line, Das et al.^[20], discussed the effect of defect densities such as vacancies and conclude that with increasing the Cu/In ratio the material becomes a p-type semiconductor.

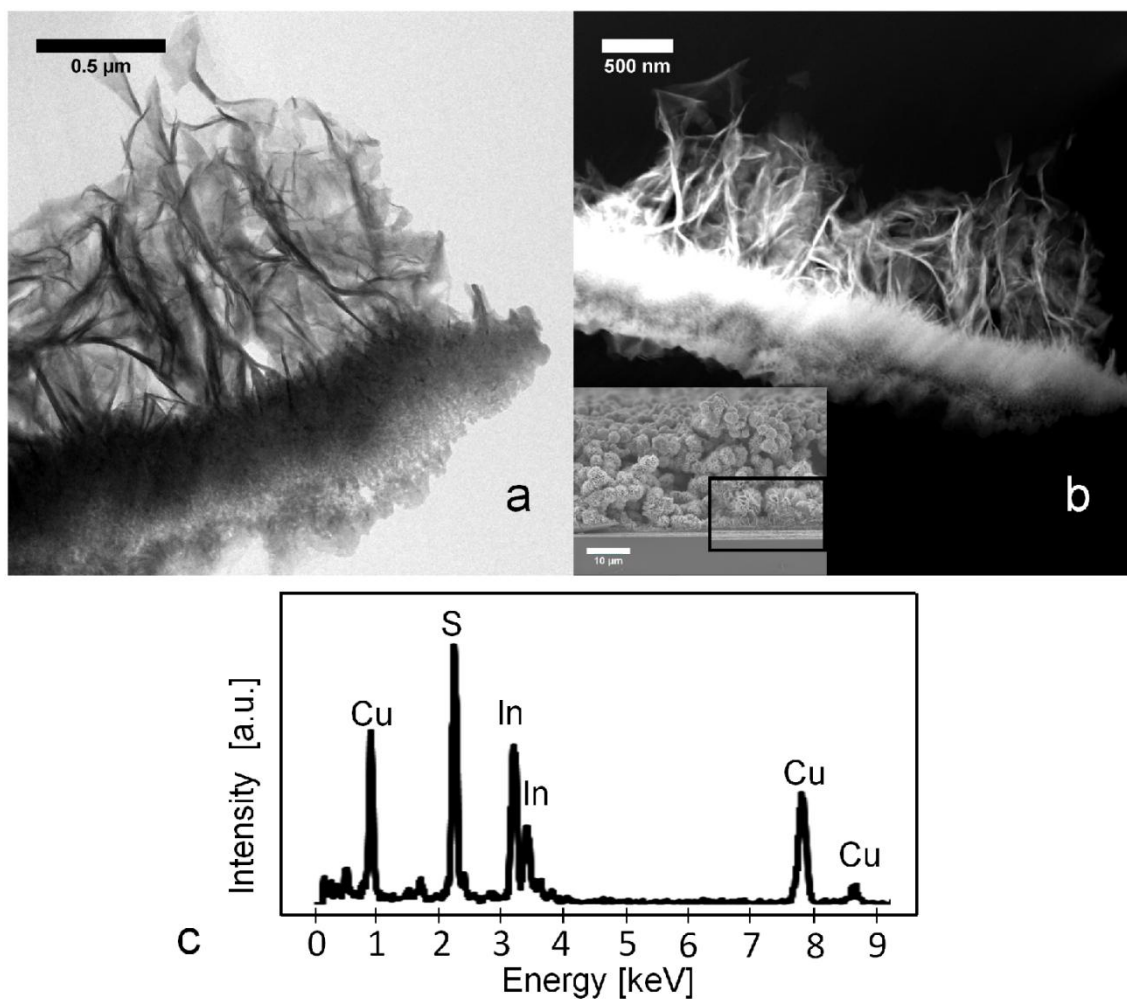


Figure 5.4: BF image (a) and HAADF-STEM image (b) of the CuInS₂ film A. Images show the densely packed layer and the flaky structure close to the FTO substrate (inset Fig. 4b). The EDX spectrum measured on an individual rod indicates the presence of Cu, In, and S (c).

Thus, our result suggests that the densely packed layer is a p-type semiconductor and could possibly be used as hole conductor in solar cells. Regarding the fact that the average chemical composition determined by EDX measurements in the SEM showed a stoichiometric composition and the dense layer is Cu rich, one might expect to discover some areas that are rich in In instead. Since this was not the case, we assume that the penetration depth of the electron beam during the EDX measurements in the SEM was too small to reach the dense Cu-rich layer. Therefore, only the signals of the stoichiometric spheres contribute to the average EDX spectra taken in the SEM. The results of TEM investigation of the sphere-like structure in the upper region of film A are summarized in Figure 5.5. The BF image in Figure 5.5(a) shows the edge of one sphere-like structure. In this image again CuInS₂ rods with a width of about 10 nm and a length

of several hundred nanometers can be observed, which are surrounded by individual flakes. Electron diffraction patterns were taken from individual flakes using a selected area diffraction aperture with a diameter of about 150 nm. The latter demonstrates the crystallinity of the flakes. The obtained spots confirm the tetragonal crystal structure of roquesite and represent (103), (031), (322) crystal planes. Furthermore, the diffraction pattern shows two crystals that are rotated against each other with an angle of about 10°, indicating that the flakes consist of large, thin plate-like crystals which grow above each other. The HRTEM image in Figure 5.5(b) shows one single rod of 10 nm thickness and adjacent flakes. This image confirms that the flakes are thin plate-like crystals. The HRTEM image in Figure 5.5(c) as well as the corresponding fast Fourier transforms, shown in the inset, confirms the tetragonal roquesite crystal structure on a local scale. The HRTEM image in Figure 5.5(d) illustrates that the flakes consist of large plate-like thin crystals, which are rotated with respect to each other giving rise to Moiré fringes. The TEM investigations of the thinner film B are summarized in Figure 5.6. The BF image of the TEM cross-section (Figure 5.6(a)) shows the 200 nm thick compact layer close to the FTO substrate. In the upper region of the film, the flakes occur. In the BF image in Figure 5.6(b), the densely packed layer can be observed as well. The film has delaminated from the substrate during the TEM sample preparation. In these films, we also found the branched structures in which flakes gradually grow out of the rods, which can be seen in the upper region of this image. The total film thickness determined by TEM is about 400 nm. Figure 6c shows the HRTEM image of the compact layer, which was taken from the lower region of Figure 5.6(b). The dense layer is polycrystalline, which is in accordance with the electron diffraction data. The pattern displayed as inset was taken from the dense layer from a circular area with a diameter of 150 nm and possesses spots that again match well with the d values of roquesite for (112), (123), and (132).

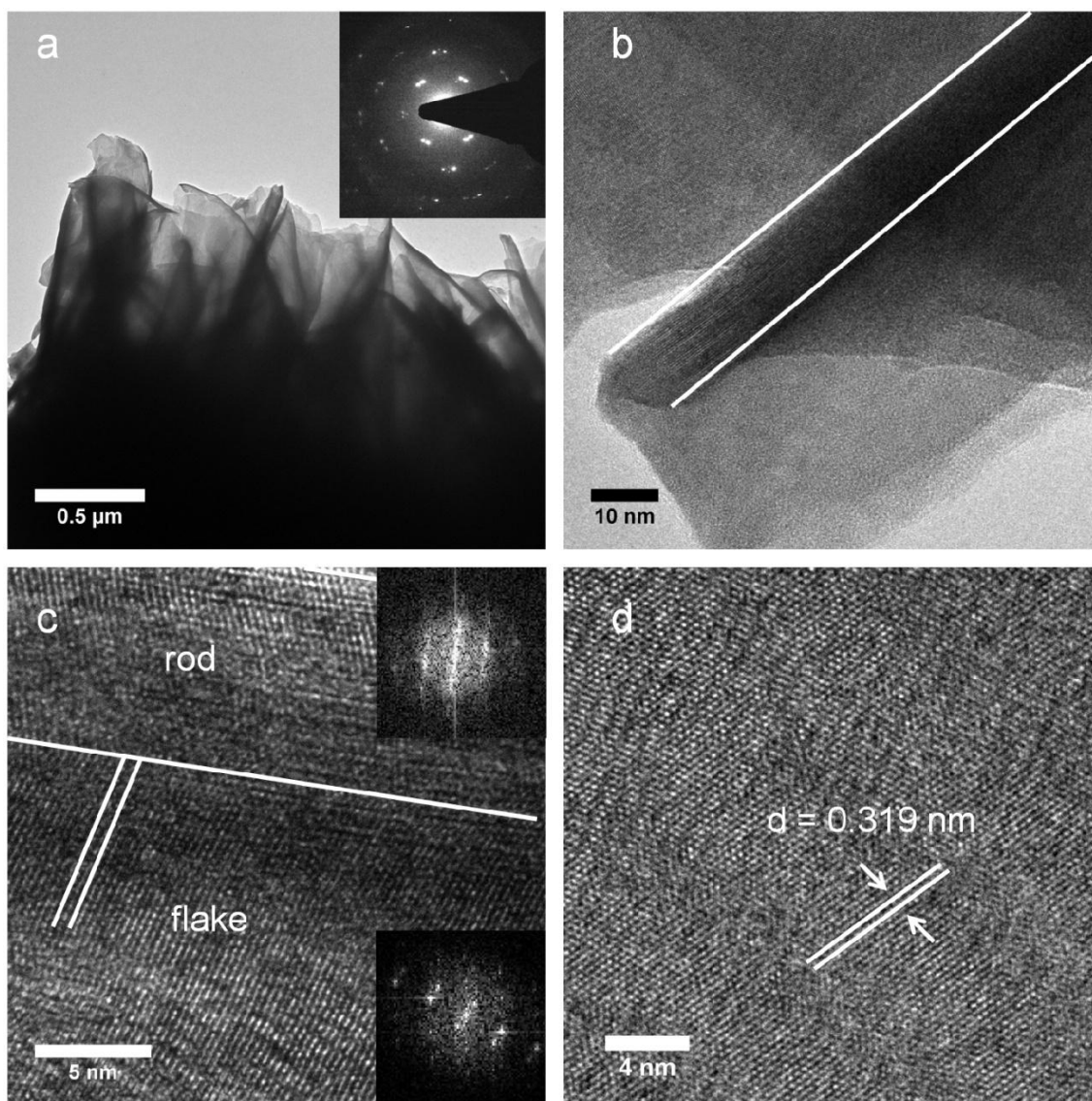


Figure 5.5: BF image (a) showing the edge of one crystal sphere. The diffraction pattern taken from different flakes shows large crystals that are rotated against each other. HRTEM images (b, c) show a single rod with attached flakes, growing out in a preferred orientation. HRTEM (d) indicates that the flakes consist of large crystal grains that are rotated against each other.

The EDX analysis of this film was done in TEM mode. The measured areas possess a diameter of around 120 nm. The spectra which were taken in the area of the densely packed layer show an average chemical composition rich in Cu and with a comparable lower amount of S. The quantification of the EDX spectra results in 30 ± 2 at.% Cu, 17 ± 2 at.% In, and 43 ± 2 at.% S. The measurement in a region with more rods resulted in 28 ± 2 at.% Cu, 24 ± 2 at.% In, 48 ± 2 at.% S and gives, considering the error margin, on average a chemically stoichiometric composition. These results are in good agreement with the EDX measurements of the densely packed layer with the flaky

structure close to the FTO substrate of film A. It is worth to mention that in the areas investigated by TEM, we were not able to detect copper sulfides. Thus, as discussed above, the film is mainly consisting of CuInS₂ in the roquesite structure.

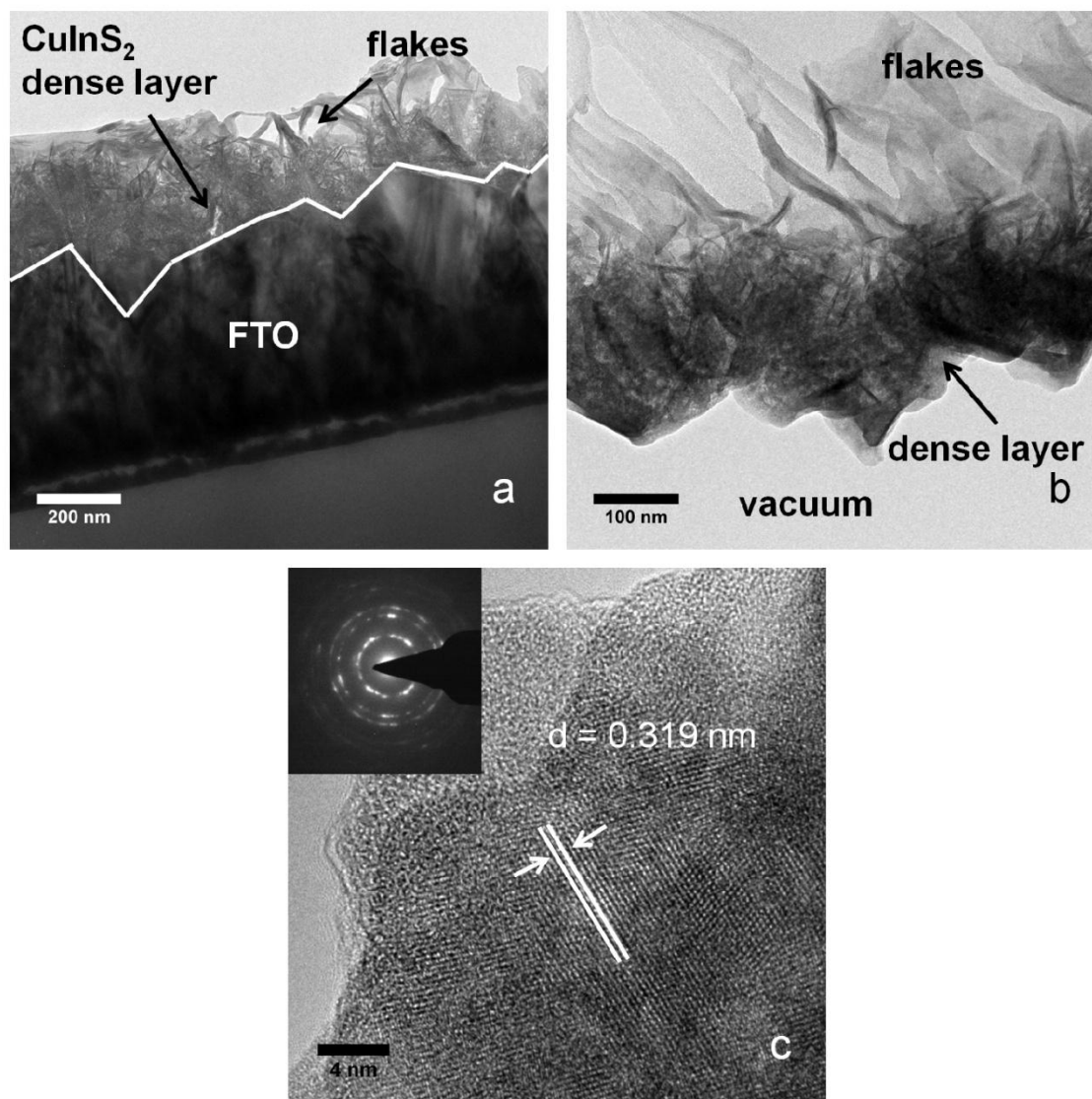


Figure 5.6: (a) BF image of the TEM cross-section of film B. The white line schematically shows the interface between FTO and the dense CuInS₂ layer. (b) BF image of film B showing the film delaminated from the substrate. The tooth-like structure of the bottom of the dense layer originates from the rough delaminated FTO substrate. The densely packed layer and the flakes can be observed. (c) The HRTEM image of the compact layer shows polycrystallinity, confirmed by the diffraction pattern displayed in the inset.

Further investigations

Further information on the average chemical composition and the optical properties of the films was obtained with ICP/AES and UV/Vis measurements. The ICP/AES analysis of film A evidenced an almost stoichiometric composition of 1.0:1.0:2.1. The signal is dominated by the contribution of the 25 μm thick layer made out of the sphere-like structures possessing a stoichiometric composition, while the thin 600 nm Cu-rich layer is only slightly changing the result. Thus, these data agree well with the results of the EDX, XRD, and TEM investigations. The UV/Vis measurement of a CuInS₂ film synthesized under the conditions for film B is shown in Figure 5.7. The spectrum displays absorption over the whole visible spectrum. It is in good agreement with data published in the literature.^[12]

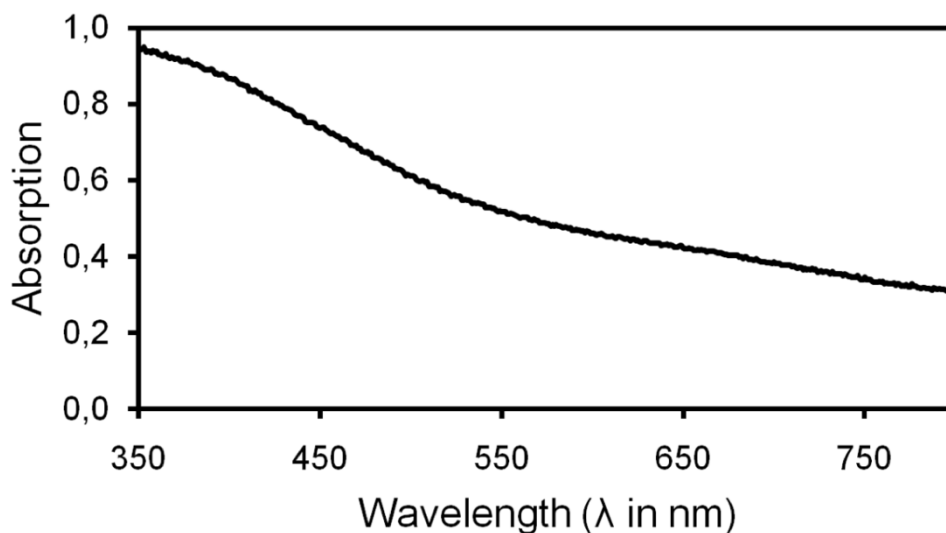


Figure 5.7: UV/Vis spectrum of film B.

Comparison with literature data

Using a solvothermal reaction, Peng et al.^[12] synthesized CuInS₂ films with a sphere-like structure on FTO substrates. They obtained films with a thickness of 8 down to 1 μm by decreasing the starting precursor concentrations. The characterization of the films was done with XRD, SEM and UV/Vis spectroscopy. In our study, we use a similar reaction route while varying process parameters such as the stoichiometry, reaction time, temperature, and cooling procedure. Thereby, we were able to fabricate thinner films down to 200 nm. In addition, compared to Peng's results our films possess different

layers and show more homogeneity and higher density of the sphere-like structure by using a lower concentration of the reactants. The differences observed between Peng's results and our film A can possibly be traced back to a different cleaning process of the substrate in the ultrasonic bath, different substrate size and dissimilar immersion depth of the substrate in the reaction solution.

Qi et al.^[17] fabricated porous CuInS₂ hollow microspheres with a simple solvothermal route. Compared to our sphere-like structures of film A growing in the upper region, their microspheres have a similar dimension and outer appearance. The forming of hollows in the microspheres results from different synthesis precursors and solvents, and is not observed in our films.

Wen et al.^[21] synthesized CuInS₂ microspheres via a mild solvothermal reaction using a biomolecule-assisted synthesis. They showed that the use of L-cysteine as sulfur source is applicable for the synthesis of CuInS₂. With this synthetic approach, they obtained microspheres with a diameter of 500 nm to 1 μm with a flaky structure comparable to our microspheres occurring in the upper region of film A. Compared to their results our microspheres have a diameter up to 3 μm. With XRD measurements, they found the tetragonal roquesite structure and they confirmed its occurrence using electron diffraction patterns obtained in the TEM.

Das et al.^[20] determined the effect of Cu/In molar ratio on microstructural and optical properties of microcrystalline CuInS₂ powder. They also used a solvothermal reaction albeit with different reactants. For all samples XRD measurements showed the characteristic reflections of the tetragonal roquesite structure. In addition, with a higher amount of In in the reaction solution, reflections of In₂S₃, and with more Cu, additional CuS was observed. More Cu or a stoichiometric Cu/In ratio in the reaction solution resulted in smooth microspheres. On the other hand, a higher amount of In in the reaction solution led to a more flaky structure. In comparison, in this study a molar ratio of Cu/In of 1 gives rise to a flaky structure (film A).

5.5 Summary

In conclusion, two different CuInS₂ films with varying morphologies and thicknesses have been successfully prepared on a FTO substrate using a mild solvothermal synthesis route with different synthesis parameters. The films were characterized in detail with the help of SEM and TEM. Secondary electron images of the thicker film (film A) indicate that the film grows in three different layers. The film consists of an about 600 nm thick densely packed layer close to the FTO substrate followed by a 1 μm thick flaky structure. In the upper region of the film up to 3 μm thick microspheres consisting of several flakes occur. The thinner film (film B) consists of an about 200 nm densely packed layer as well and a net-like structure in the upper region comprised of intergrown flakes. The TEM investigation of both films shows that regardless of the morphology (open flakes or microspheres), the flakes grow out of nanometer scale rods of about 10 nm thickness. The flakes consist of large crystals that grow in a preferred orientation. This could be confirmed with electron diffraction. In addition, the electron diffraction patterns of the films revealed the reflexes of the tetragonal roquesite crystal structure. The EDX analysis of the films in the TEM resulted in a Cu-rich composition of the densely packed layer, which indicates a p-type semiconductor. The EDX analysis of the rods and the flakes resulted in a stoichiometric composition of Cu:In:S of 1:1:2 in the thinner films as well as in the thicker films and the microspheres. With XRD and ICP/AES measurements of the thicker film, a roquesite structure and a stoichiometric composition of the microspheres was confirmed. The UV/Vis measurements showed absorption over the whole visible range. Both films show a high surface area and therefore a high potential interface density. Primarily the thinner films are anticipated to be of interest for solar cell applications, since they have an adequate thickness and there is a large area available for separation of electron-hole pairs, when the material is combined with a suitable electron conductor.

5.6 Chapter references

- [1] B. Tell, J. L. Shay, H. M. Kasper, *Phys. Rev. B* **1971**, 4, 2463.
- [2] T. Yukawa, K. Kuwabara, K. Koumoto, *Thin Solid Films* **1996**, 286, 151-153.
- [3] J. A. Hollingsworth, K. K. Banger, M. H. C. Jin, J. D. Harris, J. E. Cowen, E. W. Bohannon, J. A. Switzer, W. Buhro, A. F. Hepp, *Thin Solid Films* **2003**, 431, 63-67.
- [4] M. C. Zouaghi, T. Ben Nasrallah, S. Marsillac, J. C. Bernede, S. Belgacem, *Thin Solid Films* **2001**, 382, 39-46.
- [5] H. J. Muffler, C. H. Fischer, K. Diesner, M. C. Lux-Steiner, *Sol. Energy Mater. Sol. Cells* **2001**, 67, 121-127.
- [6] S. i. Kuranouchi, T. Nakazawa, *Sol. Energy Mater. Sol. Cells* **1998**, 50, 31-36.
- [7] R. Scheer, I. Luck, M. Kanis, M. Matsui, T. Watanabe, T. Yamamoto, *Thin Solid Films* **2001**, 392, 1-10.
- [8] J. Möller, C. H. Fischer, H. J. Muffler, R. Könenkamp, I. Kaiser, C. Kelch, M. C. Lux-Steiner, *Thin Solid Films* **2000**, 361-362, 113-117.
- [9] P. Guha, D. Das, A. B. Maity, D. Ganguli, S. Chaudhuri, *Sol. Energy Mater. Sol. Cells* **2003**, 80, 115-130.
- [10] H. M. Pathan, C. D. Lokhande, *Appl. Surf. Sci.* **2004**, 239, 11-18.
- [11] Y. Shi, Z. Jin, C. Li, H. An, J. Qiu, *Appl. Surf. Sci.* **2006**, 252, 3737-3743.
- [12] S. Peng, F. Cheng, J. Liang, Z. Tao, J. Chen, *J. Alloys Compd.* **2009**, 481, 786-791.
- [13] S. Han, M. Kong, Y. Guo, M. Wang, *Mater. Lett.* **2009**, 63, 1192-1194.
- [14] J. Xiao, Y. Xie, R. Tang, Y. Qian, *J. Solid State Chem.* **2001**, 161, 179-183.
- [15] G. Z. Shen, D. Chen, K. B. Tang, Z. Fang, J. Sheng, Y. T. Qian, *J. Cryst. Growth* **2003**, 254, 75-79.
- [16] J. Feng, J. Han, X. Zhao, *Prog. Org. Coat.* **2009**, 64, 268-273.
- [17] Y. Qi, K. Tang, S. Zeng, W. Zhou, *Microporous Mesoporous Mater.* **2008**, 114, 395-400.
- [18] A. Strecker, U. Salzberger, J. Mayer, *Prakt. Metallogr.* **1993**, 30, 482-495.
- [19] F. B. Dejene, *J. Mater. Sci.* **2011**, 46, 6981-6987.
- [20] K. Das, S. K. Panda, S. Gorai, P. Mishra, S. Chaudhuri, *Mater. Res. Bull.* **2008**, 43, 2742-2750.
- [21] C. Wen, X. Weidong, W. Juanjuan, W. Xiaoming, Z. Jiasong, L. Lijun, *Mater. Lett.* **2009**, 63, 2495-2498.

6 Systematic study of the reactant concentration and reaction times on CuInS₂ films

6.1 Introduction

During the research of new low cost materials for solar cells, an easy and cheap manufacturing process is of high interest. A promising low cost semiconductor material is CuInS₂, which possesses outstanding physical and optical properties for solar cell application. Depending on the synthesis and the resulting chemical composition it can form a n-type or p-type semiconductor. Thereby a Cu-rich chemical composition leads to a p-type and an In-rich chemical composition to a n-type semiconductor.^[1, 2] CuInS₂ thin films can be synthesized with a mild solvothermal process, which is an easy and low cost synthesis method. The synthesis of such films is already described in literature and introduced in chapter 5.^[3] In the present thesis the solvothermal synthesis route of Peng et al.^[4] was modified. The investigation of structured CuInS₂ thin films with a Cu-rich compact layer and a stoichiometric flaky structure in the upper film region, with a high surface area, was presented in chapter 5. There the results for two films, which were synthesized with different reagent concentrations and reaction times (12 and 24 h) were described regarding the morphology, crystal structure and the chemical composition. In the following chapter, further investigations on CuInS₂ films, synthesized with the solvothermal method, were summarized. The influence of doubling the concentration of reactants and changing the reaction time from 0.5 h up to 24 h on the film thickness, morphology and chemical composition is investigated systematically. This was realized with SEM, XRD and TEM based techniques as well as EDX in the SEM and TEM.

6.2 Experimental details

CuInS₂ films were prepared using a solvothermal synthesis route according to Wochnik et al.^[3] (see chapter 5.2). (FTO) conductive glass (Pilkington) with the dimension of 15 x 30 x 2 mm³ was used as substrate for the deposition of the CuInS₂ films. The substrates were cleaned in diluted nitric acid, acetone, double-distilled water and ethanol in an ultrasonic cleaner for 5 min. In a Teflon-lined stainless steel autoclave (20 mL) CuSO₄ · 5H₂O, InCl₃ and C₂H₅NS were dissolved in 10 mL ethanol and stirred for 15 min. The washed substrate was placed diagonally (FTO surface pointing downwards) in the Teflon liner. The autoclave was closed and heated at 150 °C for different times. Two different reactant concentrations were used. The lower concentration is referred as A and the higher as B. The reactant concentration and the used reaction times for all synthesized films are summarized in Table 6.1. The obtained brownish colored films on FTO were washed afterwards using double-distilled water and ethanol.

Table 6.1: Reactant concentration and used reaction times for all synthesized films.

Film	Concentration CuSO ₄ · 5H ₂ O [mmol]	Concentration InCl ₃ [mmol]	Concentration Thioacetamide [mmol]	Reaction time [h]
1A	0.1	0.1	0.3	0.5
2A	0.1	0.1	0.3	3
3A	0.1	0.1	0.3	6
4A	0.1	0.1	0.3	9
5A*	0.05	0.05	0.2	22
6A	0.1	0.1	0.3	24
Film	Concentration CuSO ₄ · 5H ₂ O [mmol]	Concentration InCl ₃ [mmol]	Concentration Thioacetamide [mmol]	Reaction time [h]
1B	0.2	0.2	0.5	0.5
2B	0.2	0.2	0.5	3
3B	0.2	0.2	0.5	6
4B	0.2	0.2	0.5	9
5B	0.2	0.2	0.5	18
6B	0.2	0.2	0.5	22

For film 5A* only half concentration was used.

6.3 Characterization

The general morphology investigations of the different films were done using a Jeol JSM-6500F SEM equipped with an energy dispersive X-ray detector from Oxford Instruments (Inca Energy). It was operated at 4.0 kV and secondary electron (SE) images were acquired using the implemented Jeol standard detector. SEM top view and cross-section samples were prepared by conventional preparation techniques. TEM characterization was done using a FEI Titan 80 – 300 kV (S)TEM microscope equipped with a Gatan Tridiem image filter, an EDAX EDX detector for analytical measurements and a HAADF detector from Fischione Instruments (Model 3000). Cross-sectional TEM specimens were prepared as described in chapter 3.9. Electron diffraction data were analyzed using a calibrated camera constant obtained by applying a Si standard. For determination of the crystal structure of the thin films, XRD patterns were taken on a diffractometer D8 Discovery from Bruker with CuK_α radiation ($\lambda = 1.54 \text{ \AA}$). The scanning rate was $0.05^\circ/\text{s}$ and the 2θ range was chosen from 20° to 65° . The obtained patterns were compared to literature data.

6.4 Results

Figure 6.1 shows the SE images from the films synthesized with the lower reactants concentration A and different reaction times. All films reveal the typical flaky surface of the CuInS₂ films obtained by this reaction method. In Figure 6.1(a) film 1A is shown, which was synthesized with a reaction time of 0.5 h. The image displays that the FTO substrate is completely coated with the CuInS₂ film. At higher magnification (inset in Figure 6.1(a)) the porous surface built of small flakes can be seen. A SEM cross section could not be obtained because of the low film thickness. In Figure 6.1(b) the SE image of film 2A synthesized with a reaction time of 3 h is given. The top view of the film reveals a structured film at lower magnification. Higher magnification indicates that the film consists of more compact and thicker flakes compared to film 1A. A film thickness of 250 nm was observed. The morphology of film 3A (reaction time 6 h) is presented in Figure 1(c). The flaky structure of the film can be seen already at a lower magnification. The flakes have a more open structure compared to film 1A and 2A as visible at higher magnification. The cross section shows like for film 2A a thickness of 250 nm. Film 4A

(Figure 6.1(d)) possesses a similar surface as film 3A. However, at higher magnification it can be observed that the flakes become thinner and that a more open structure is formed. The cross section of the film shows a thickness of 350 nm. Film 5A is displayed in Figure 6.1(e). The film was synthesized with half of the concentration as for the other films and by using a reaction time of 22 h. In comparison to the other films the SE image at higher magnification indicates thinner flakes. This means that the lower concentration could have an influence on the flake thickness. The cross section of the film reveals a film thickness of around 400 nm. In Figure 6.1(f) film 6A is shown, which was prepared with concentration A and heated for 24 h. This film was already described in a previous work (see chapter 5). The structure and thickness of the flakes, as well as the film thickness of around 400 nm are similar to film 4A. These results suggest that an increasing reaction time has an influence on the film thickness and the surface morphology until a reaction time of approximately 9 h. Increasing the reaction time further does not result in significant changes in film morphology when using a low concentration A. The thicknesses of the films 1A – 6A are summarized in Table 6.2.

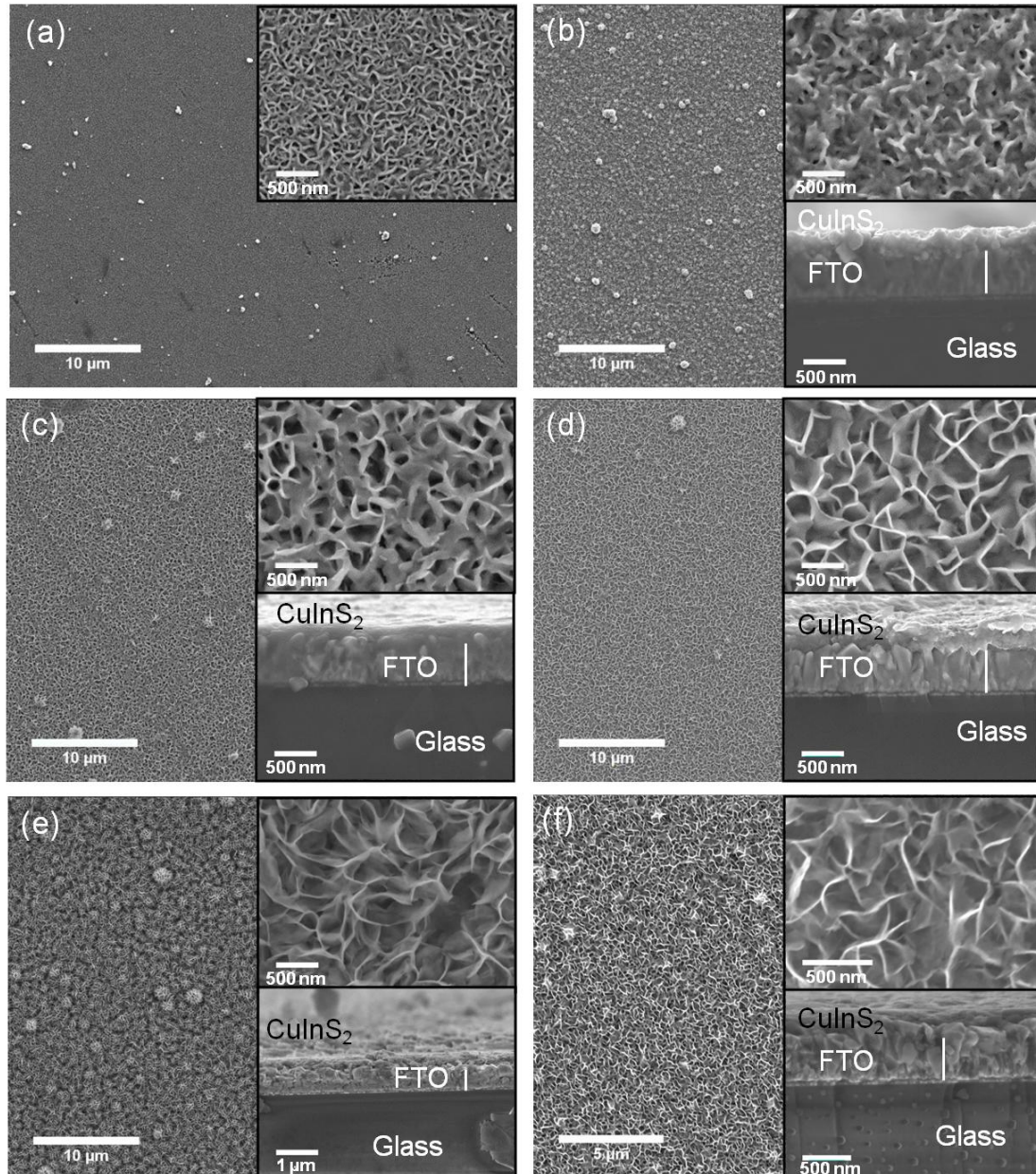


Figure 6.1: SE images of the CuInS_2 films synthesized with reactant concentration A for different reaction times. Figure (a) shows film 1A (0.5 h), (b) film 2A (3 h), (c) film 3A (6 h), (d) film 4A (9 h), (e) film 5A (22 h) synthesized with half of the reagent concentration and (f) film 6A synthesized for 24 h (note the different scale bar). It can be seen that the flaky structure of the films is changing from short compact flakes to longer and thinner flakes by increasing the reaction time from 0.5 h to 9 h. After 9 h no significant changes in the film thickness and the surface morphology could be observed. The thinner flakes in (e) result from a lower concentration.

Table 6.2: Film thicknesses of the films synthesized with reactant concentration A for different reaction times.

Film	Film thickness [nm]
1A	-
2A	250
3A	250
4A	350
5A	400
6A	400

In Figure 6.2 the SEM images of films synthesized with a higher reactant concentration B are displayed. In Figure 6.2(a) shows film 1B prepared with a reaction time of 0.5 h is given. It can be seen that the film consists of a structured surface. The image at higher magnification indicates the flaky structure with more compact flakes, whereby it seems that the flakes are grown together. The cross section reveals a film thickness of about 200 nm. Film 2B (reaction time 3 h) is pictured in Figure 6.2(b). Already with a lower magnification the flaky surface of the film can be observed. At a higher magnification it can be seen, that the morphology of this film is similar to film 4A (Figure 6.1(d)) synthesized with half of the reactants concentration but heated with a 3 times longer reaction time. In contrast to film 4A, film 2B has a much longer thickness of around 800 nm. Film 3B (reaction time 6 h) is shown in Figure 6.2(c). The film possesses a similar morphology as film 2B (b). Here a film thickness of 900 nm was measured. In Figure 6.2(d) film 4B (reaction time 9 h) can be seen. At lower magnification a more open and wide structure, compared to the other films synthesized at shorter reaction can be observed. At a higher magnification we can find bigger and thinner flakes, which grow on top of smaller and shorter ones. The cross section reveals a film thickness of approximately 950 nm. The film thickness might differ slightly from this value, because the flakes could be squeezed during the SEM sample preparation. Film 5B (reaction time 18 h) and film 6B (reaction time 22 h) are displayed in Figure 6.2(e) and Figure 6.2(f). Both films show a similar flaky structure and are comparable to film 4B. For both films (5B, 6B) a thickness of 900 nm was measured in the SEM. These results indicate that a longer reaction time than 9 h has no significant influence on the film thickness and

surface morphology like flake size and thickness. The same trend was observed for the films synthesized with reaction concentration A (Figure 6.1(a) - (f)). The measured film thicknesses of film 1B – 6B are summarized in Table 6.3.

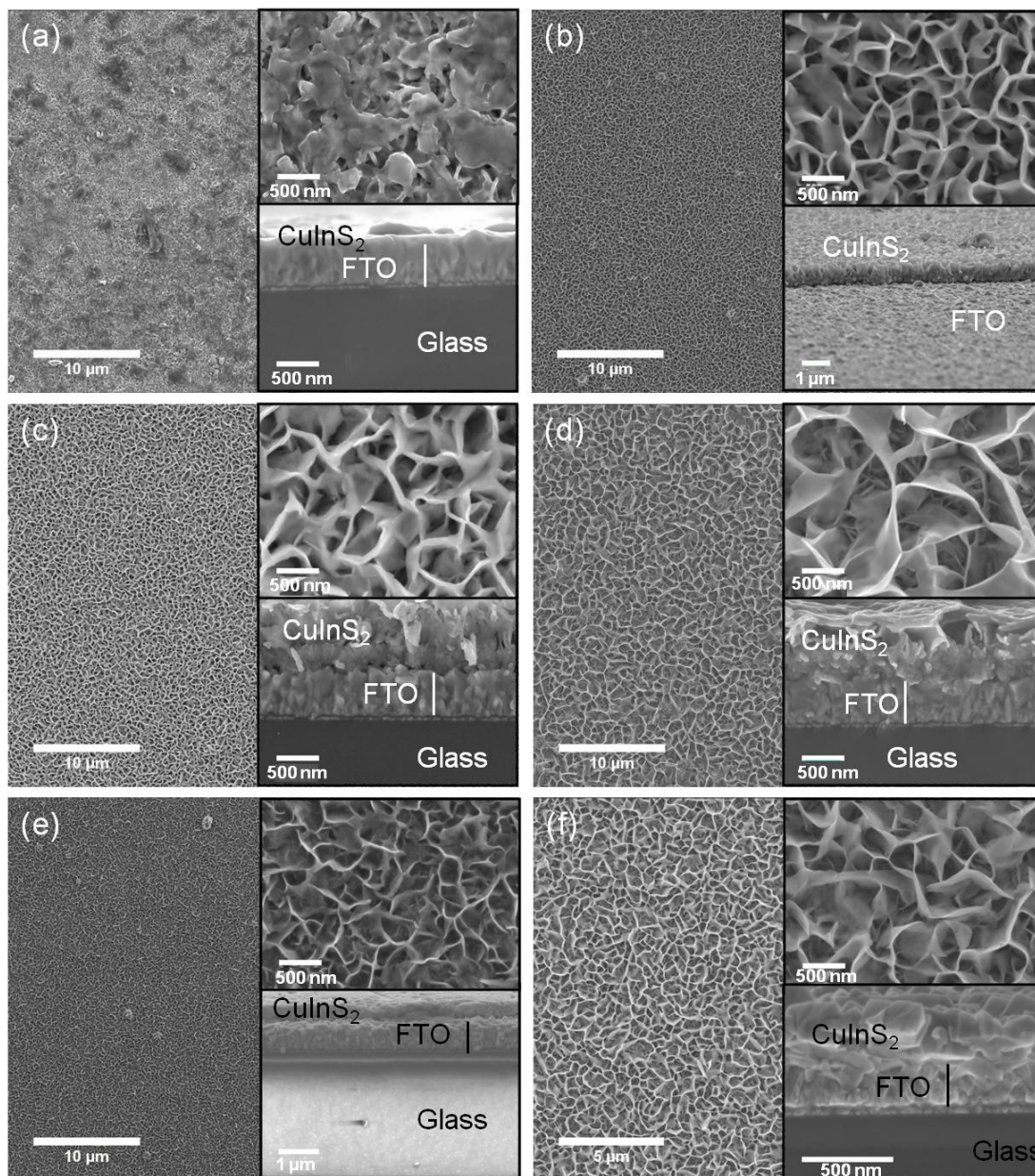


Figure 6.2: SE images of the CuInS₂ films synthesized with reactant concentration B for different reaction times. Figure (a) shows film 1B (0.5 h), (b) film 2B (3 h), (c) film 3B (6 h), (d) film 4B (9 h), (e) film 5B (18 h) and (f) film 6B synthesized for 22 h (note the different scale bars). It can be again observed that the flaky structure of the films is changing from short compact flakes to longer and more open flakes by an increase of the reaction times from 0.5 h to 9 h. Also the film thickness is increasing. After 9 h no changes could be observed. The same trend was observed by the films synthesized with reactant concentration A.

Table 6.3: Film thicknesses of the films synthesized with reactant concentration B for different reaction times.

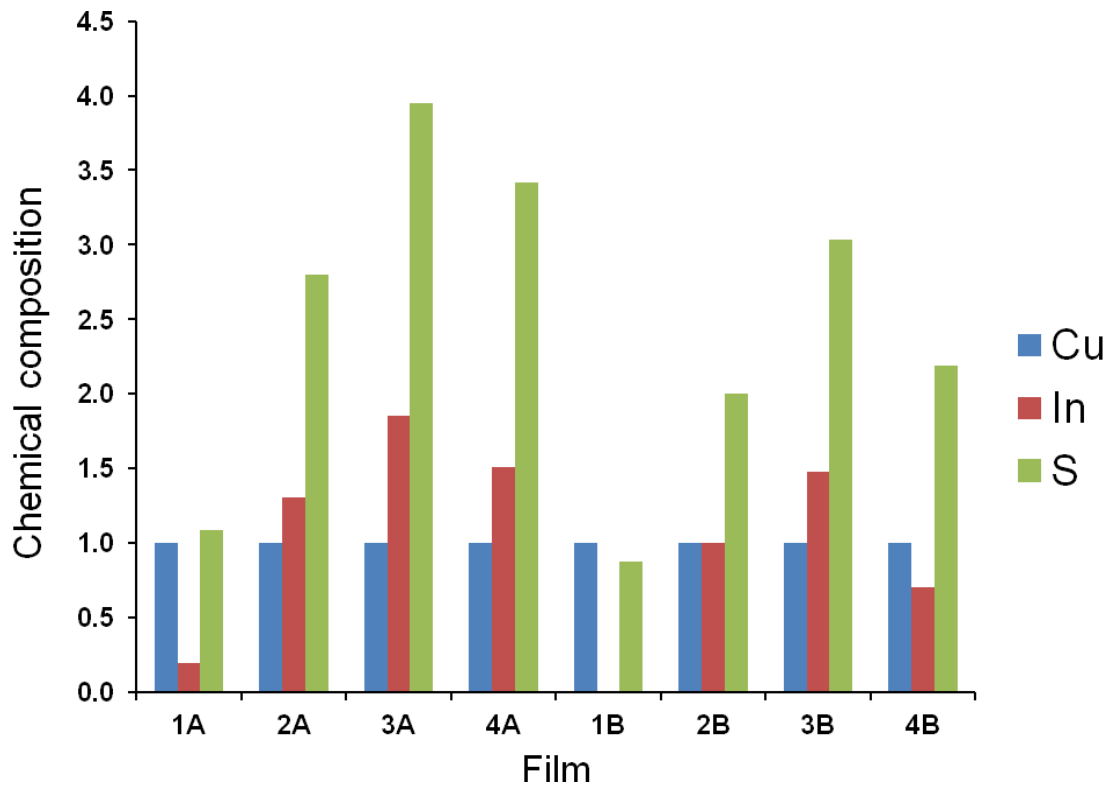
Film	Film thickness [nm]
1B	200
2B	800
3B	900
4B	950
5B	900*
6B	900

*determined in the TEM

The average chemical composition of the films synthesized with reactant concentration A and B and applying reaction times of 0.5 – 9 h was analysed by EDX measurements in the SEM. As discussed in chapter 5, signals from the substrate such as O, Si, Sn, F always contribute to the measurements due to the low film thickness. Taken this in consideration, the Cu:In:s ration has been calculated and is summerized in Table 6.4. The chemical composition of the different synthesized films is shown in Figure 6.3, whereby Cu is normed as 1. It can be seen that the films 1A and 1B, each synthesized for 0.5 h consist of more or less only Cu and S. Nearly no In could be detected. The quantification of the films 2A and 2B (reaction time 3 h) gives in both cases an almost stoichiometric Cu:In:S composition of 1:1:2. Compared to the films 2A and 2B, the films 3A and 3B show a non stoichiometric composition. In both cases the films are rich in In and S. However the rate of In:S is 1:2 in both films. In contrast to the films descibed above the films 4A and 4B show adifferent chemical composition. Film 4A has an In rich composition and again a larger amount of S while film 4B has a slightly Cu rich composition. It can be concluded, that both reaction concentrations A and B reveal similar trends. This indicates that the growth mechanism of the films seems to take place in a similar way independent of the concentration of reactants. However, the concentration has a strong impact on the film thickness.

Table 6.4: Average chemical composition of the films synthesized with reactant concentration A and B with reaction times between 0.5 – 9 h measured in the SEM.

Film	Reaction time [h]	Chemical composition		
		Cu	In	S
1A	0.5	1.0	0.2	1.0
2A	3	0.8	1.0	2.0
3A	6	1.0	1.9	3.9
4A	9	1.0	1.5	3.4
1B	0.5	1.0	0.0	0.9
2B	3	1.0	1.0	2.0
3B	6	1.0	1.5	3.0
4B	9	1.0	0.7	2.2

**Figure 6.3: Graphical illustration of the chemical composition of the different synthesized films. Cu is normed as 1.**

A detailed investigation of the chemical composition of film 2A (reaction time 3 h) and two films with longer reaction times, film 5B (18 h) and film 6A (24 h) was done by EDX measurements in the TEM. For film 2A several measurements were done in STEM mode with a spot size of about 1 nm. A BF image of the film is shown in Figure 6.4(a), which reveals a 300 nm thick, nanocrystalline film consisting of nanorods, flakes and nanoparticles. The quantification of the EDX measurements from the nanocrystalline areas in between the rods resulted in a chemical Cu:In:S composition of 1:1:1. The measurements from the rods resulted in $45,6 \pm 3 \text{ at.}\%$: $15,8 \pm 2 \text{ at.}\%$: $38,7 \pm 3 \text{ at.}\%$ of Cu:In:S leading to a composition of 1:0.4:1.2. These results are not in agreement with the EDX measurements in the SEM, which gave a nearly average stoichiometric chemical composition. But the measurements in the TEM allow a more detailed analysis of the film composition than EDX measurements done in the SEM. Most likely the contribution from the substrate introduce larger errors in the quantification in particular for thin films. An exemplary BF image from film 5B is given in Figure 6.4(b). The film shows the well-known structure consisting of the compact layer close to the FTO substrate and the out growing rods and flakes (compare chapter 5). The EDX measurements of this film were also done in STEM mode and the quantification resulted for the compact layer close to the FTO substrate in $44.7 \pm 3 \text{ at.}\%$: $12.6 \pm 2 \text{ at.}\%$: $41.5 \pm 3 \text{ at.}\%$ of Cu:In:S and resulted in a composition of 1:0.3:0.9. The measurements in the middle of the compact layer points to $33.8 \pm 3 \text{ at.}\%$: $20.5 \pm 2 \text{ at.}\%$: $49.6 \pm 3 \text{ at.}\%$ and leads to a Cu:In:S composition of 1:0.6:1.5. In the flakes $35.2 \pm 3 \text{ at.}\%$: $24.8 \pm 3 \text{ at.}\%$: $49.8 \pm 3 \text{ at.}\%$ were measured, which gives a stoichiometric Cu:In:S composition of 1:1:2. The Cu rich compact layer close to the FTO substrate and the increase of the In amount leading in a stoichiometric composition in the flaky structure was already observed before and is discussed in the publication in chapter 5. The same result was obtained for film 6A (reaction time 24 h) referred as film B in the previous study (see chapter 5). A bright field image of this film is given in Figure 6.4(c) which shows the compact layer and the flakes in the upper region. Electron diffraction patterns were taken from film 3A (Figure 6.4(d)), film 5B (Figure 6.4(e)) and 6A (Figure 6.4(f)), using a selected area diffraction aperture with a diameter of around 150 nm. The analysis reveals the characteristic reflections of CuInS₂ corresponding to (112), (204) and (312) lattice planes of the Roquesite crystal structure. The presence of Cu_xS phases can not be excluded because of similar values and an error of about 3% in the determination of lattice planes by TEM.

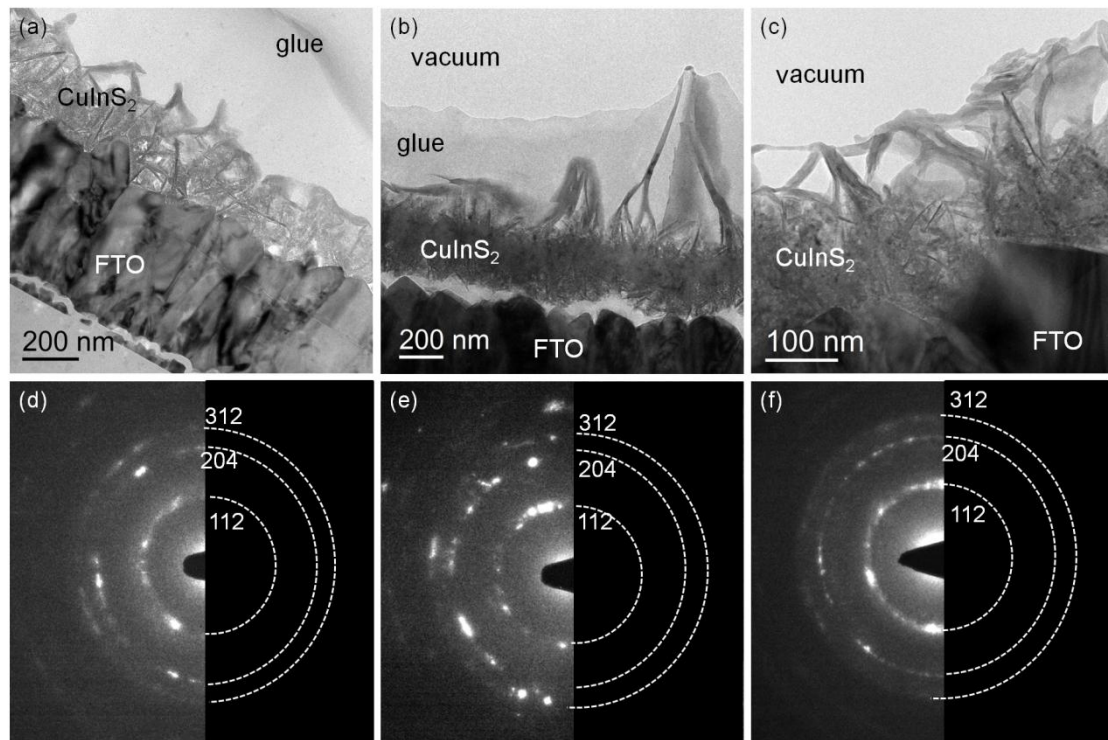


Figure 6.4: BF images of film 2A (a), film 5B (b) and film 6A (c). The corresponding diffraction patterns are shown in (d) taken from film 2A, (e) from film 5B and in (f) from film 6A. The characteristic reflections of (112), (204) and (312) from CuInS_2 in Roquesite structure were found. The presence of Cu_xS phases cannot be excluded.

For an additional characterization of the crystal structure and to exclude additional phases, XRD measurements from selected samples were realized. XRD offers a higher resolution and lower error bar concerning determination of lattice plane distances. Exemplarily for our results the spectrum of film 3B (reaction time 6 h) is given in Figure 6.5. Besides the reflections of the FTO (marked with *) only reflections of CuInS_2 , which can be referred to the (110) and (204) plane were found. No further reflections of additionally phases can be observed and thus Cu_xS phases can be excluded. The XRD pattern taken from the films 2B, 3A, 5B, 6A and 6B gave the same result (spectra shown in Figure A1 - A5 in Appendix). For the films 1A, 1B and 5A no XRD measurements were performed, because of the marginal film thickness.

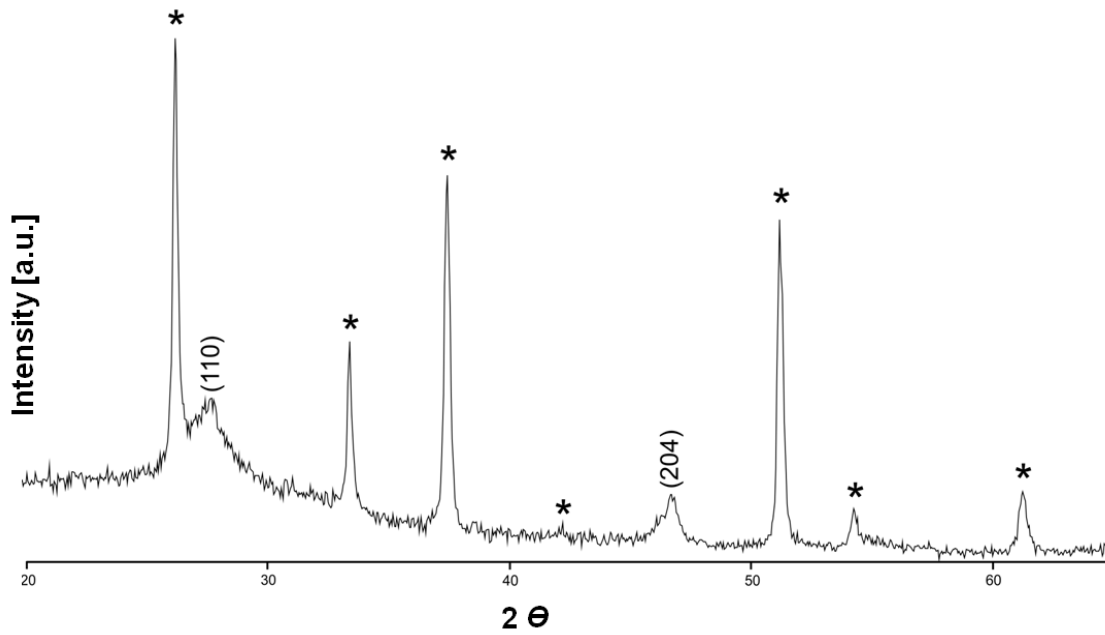


Figure 6.5:XRD pattern of film 3B. Besides the reflections of FTO (marked with *) the reflections of CuInS₂ assigned to (110) and (204) are marked.

Further detailed characterization of the rods and the out growing flakes are done in the TEM. From film 6A HRTEM images were taken and FFT analysis from particular areas was done. The typical d values and the appropriate hkl values, as well as the particular angles between the reflections for CuInS₂ in Chalcopyrite, Zinblende and Wurtzite structure are calculated and given in Table 6.5.

Table 6.5: Calculated d values, hkl and particular angles between the reflections for CuInS₂ in Chalcopyrite, Zincblende and Wurtzite structure.

Crystal system	d values	hkl	Calculated angle*
tetragonal (Chalcopyrite)	3.20	(112)	
	1.96	(204)	
	1.67	(312)	
cubic (Zincblende)	3.19	(111)	
	1.95	(220)	
	1.67	(311)	
hexagonal (Wurtzite)	3.22	(0,0,0,2)	
	1.95	(1,1,-2,0)	
	1.67	(1,1,-2,2)	

*calculated with the program DigitalMicrograph

Figure 6.6(a) shows a HRTEM image of a rod. The analysis of the FFT (inset) of the rod reveals again the typically d values at 3.20 Å, 1.96 Å and 1.67 Å, which were also obtained in the electron diffraction experiment of the films. The measured angles between the reflections reveal that the rods are growing in the hexagonal Wurtzite structure. A zone axis in the [-1100] direction could be determined. The HRTEM image in Figure 6.6(b) indicates a flake, which grew out of a rod. Also the FFT of the flake reveals reflections with the d values of 3.20 Å and 1.96 Å. The measured angles between these reflections indicate that the flakes are growing in the Chalcopyrite or in the Zincblende structure. A zone axis of [20-1] for Chalcopyrite or Zincblende was determined. The measured angles are summarized in Table 6.6.

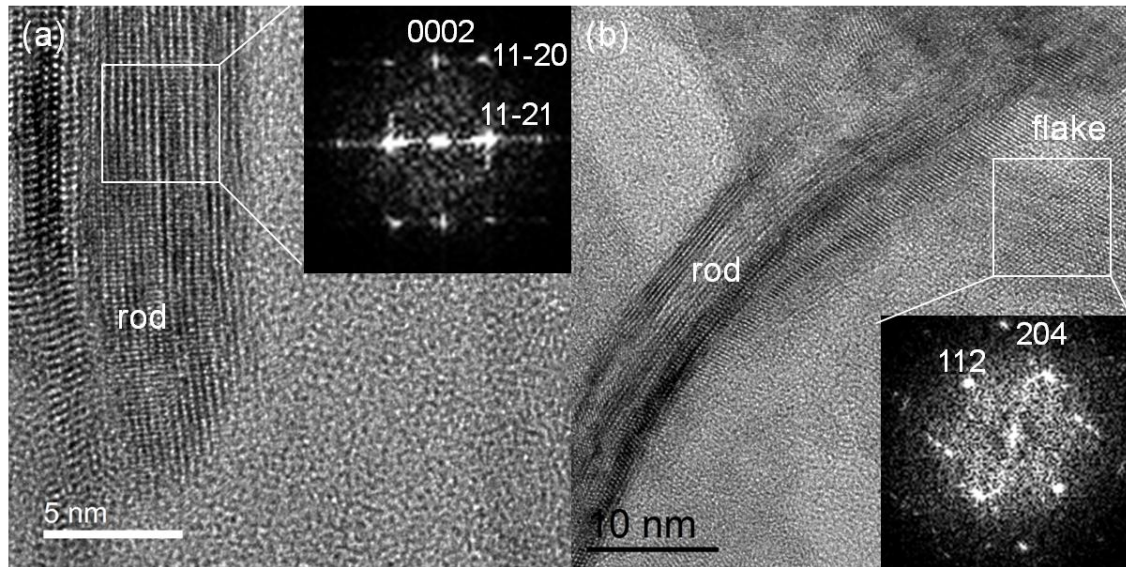


Figure 6.6: HRTEM images of film 6A. (a) shows a HRTEM image of a rod. The FFT (inset) reveals reflections of CuInS₂. The measured angles indicate the Wurtzite structure. (b) displays a HRTEM image from a rod and a out-growing flake. The FFT (inset) analysis of the flake reveals again the typical reflections of CuInS₂. The measured angles indicate the Chalcopyrite or Zincblende structure.

Table 6.6: Measured angles between the atomic plane distances obtained from FFT analysis.

	<i>d</i> values (<i>hkl</i>)	Measured angle
Rod (Figure 6.6(a))	3.20 (112) 1.96 (220) 1.67 (311)	$\left. \begin{array}{l} 89.95^\circ \\ 31.11^\circ \end{array} \right\} 59.12^\circ$
Flake (Figure 6.6(b))	3.20 (112) 1.96 (220)	$\left. \begin{array}{l} 35.37^\circ \end{array} \right\}$

6.5 Discussion

The obtained results of the morphology investigations in the SEM showed that the concentration of reactants have a high influence on the film thickness. Films synthesized with a lower concentration of reactants are inherently thinner than films with higher reactants concentration. A longer reaction time than 9 h leads to no significant changes in the film thickness for both investigated reaction concentrations. This means that the lower concentration of 0.1:0.1:0.3 mmol Cu:In:S precursors results to a maximal film thickness of 400 nm and the higher concentration of 0.2:0.2:0.5 mmol Cu:In:S precursors to 900 nm. The influence of the concentration of reactants on the morphology of the films is low. However, closer examination of the morphology showed that the size and thickness of the flakes are slightly thicker for the shorter reaction times. The reaction time has a high influence on the film thickness and morphology in both used reactant concentrations. With increasing reaction times up to 9 h the flakes become thinner and larger. However, after 9 h reaction time for both concentrations the morphology is not changing anymore. The quantification of the EDX measurements from the different synthesized films, realized in the SEM, showed a similar trend in the chemical composition, for both used reactants concentrations (Figure 6.3). These EDX measurements indicate that the growth of the films starts with a coppersulfide phase, because in the films, synthesized for 0.5 h, nearly no In was detected. The amount of In and S increases with longer reaction times. The (Cu-In-S)-system can be described by the quasi-binary Cu₂S-In₂S₃ phase diagram.^[5] The formation of mainly CuInS₂ in the Roquesite structure at around 50 to 52% mole percent In₂S₃ is known and is probably valid in our reaction conditions by used equimolar amounts of Cu:In. Our observation leads us to the conclusion that the In is slowly reacting. Because of the In-rich composition at a reaction time of 6 h we propose that the aggregation of Cu_xS and In₂S₃, formed in the reaction solution (confirmed by further investigations (see chapter 7)), take place successively, starting with Cu_xS. This assumption is confirmed by the TEM investigation of the films synthesized for longer reaction times (film 5B and 6A), which indicates a gradient in the chemical composition starting with the Cu-rich compact layer leading to the stoichiometric composition of the flaky structure existing in the upper flaky region. The detailed TEM investigation of film 2A synthesized for 3 h showed also a Cu-rich composition. The electron diffraction experiments and the XRD measurements

reveal no reflections of additionally Cu_xS or In₂S₃ phases. This means that a p-type CuInS₂ is built already after 3 h with the right phase. Consequently this result indicates that the reaction time has influence on the morphology and the film thickness until 9 h and on the chemical composition which gets stoichiometric after 18 h.

The HRTEM investigations of the crystal structure of film 6A revealed that the rods grow in the hexagonal Wurtzite structure and the flakes in the hexagonal Chalcopyrite structure. Because of similar *d* values, similar angles between the lattice planes and consequently similar XRD, electron diffraction and FFT pattern the distinction of the Chalcopyrite and Zinblende structure is difficult. So the Zinblende structure cannot be excluded for the flakes. However, the transition temperature from Chalcopyrite in Zinblende phase is 979 °C as found by Rincon et al.^[6] This temperature was not reached in our reaction conditions. Hence, the formation of the Zinblende phase is unlikely.

The synthesis and characterization of CuInS₂ in Wurtzite or Zinblende structure is frequently reported in literature. Huang et al.^[7] for example synthesized CuInS₂ nanocrystals in Zinblende and Wurtzite structure. Therefore they used a simple solvothermal synthesis method. For Zinblende nanocrystals they used oleylmine and for Wurtzite nanocrystals ethylenediamine as solvent. The reaction temperature was 160 °C and the reaction time 12 h. By similar reaction conditions for our films we observe rods in the Wurtzite structure with ethanol as solvent.

Pan et al.^[8] synthesized CuInS₂ nanocrystals in Zinblende and Wurtzite structure by a hot-injection method using Cu(dedc)₂ and In(dedc)₂ precursors, while dedc is diethylenedithiocarbamat. They used oleylamine as the activation agent and oleic acid or dodecanthiol as the capping agent. The reaction temperature was 250 °C. The choice of the capping agent allows them a precise control of the crystalline structure.

Qi et al.^[9] synthesized nanostructured Wurtzite CuInS₂ with a one step solvothermal synthesis route. They obtained nanoplates, hollow spheres and solid microspheres. For the synthesis they used InCl₃·4H₂O, CuCl₂·2H₂O, thiourea and ethanolamine. The reaction was done at 180 °C for 24 h. They found that the metastable Wurtzite CuInS₂ can be completely transformed into CuInS₂ in Chalcopyrite structure by heating up to 600 °C. They found that the solvent ethanolamine plays an important role in the synthesis of Wurtzite CuInS₂.

Koo et al.^[10] reported about the synthesis of Wurtzite-Chalcopyrite polytypism in CuInS₂ nanodisks. For the synthesis they used InCl₃, CuCl, thiourea and oleylamine. The reaction was done in the absence of air and using a heating temperature of 240 °C. The obtained nanodisks exhibit a coexistence of Wurtzite and Chalcopyrite domains interface across (002)_w/(112)_{ch} stacking faults. The work of Koo et al. showed the possible coexistence of both phases during one synthesis step. In our films we found a similar phenomenon by the rods and the outgrowing flakes. We didn't use any additionally reagents, like coordinating or activating agents. Similar nanostructures of CuS and Cu₂S like nanodisks or nanorods in hexagonal structure have been observed in several studies including synthesis with a solvothermal reaction.^[11, 12] The observation, that the film starts to grow with Cu_xS phases (0.5 h reaction time) and that the accretion of Cu_xS and In₂S₃ seems to be successive leads to the consideration, that the nanocrystals and the rods start growing with a hexagonal Cu_xS phase. The rods get transformed to a stoichiometric CuInS₂ phase after reacting with In by keeping the crystal structure. While the nanocrystals and flakes obtain the Chalcopyrite structure.

6.6 Summary and Conclusion

In this study, the influence of the reactant concentration and the reaction time on the thickness, morphology and chemical composition of CuInS₂ thin films is investigated. Films with two different concentrations of the reaction solutions A and B and with different reaction times of 0.5 h, 3 h, 6 h, 9 h, 18 h, 22 h and 24 h were synthesized on a FTO substrate. With SEM investigations it was found that the reactant concentration has a high influence on the film thickness. The lower reactant concentration A leads to a maximal film thickness of 400 nm and the higher concentration B to a maximal film thickness of 900 nm. However the reactant concentration has a low influence on the morphology. In contrast the reaction time showed a high influence in the film morphology. The surface of the films consisting of nanostructured flakes becomes with increasing reaction time a more open structure with larger and longer flakes until a reaction time of 9 h. Longer reaction times showed no significant changes in the morphology. The chemical composition of the films was measured with EDX in the SEM and TEM. The quantification reveals that the films exhibit different chemical compositions by varying the reaction times. Both investigated reaction concentrations show a similar trend. With these investigations a growth mechanism of the films could

be proposed. The accumulation of Cu_xS and In₂S₃ formed in the reaction solution is successively starting with a Cu_xS phase. This leads to a non stoichiometric composition with Cu-rich or In-rich films for designated reaction times shorter than 18 h, by formation of the dominated phase of CuInS₂ in Chalcopyrite structure. However a composition gradient was found but supposedly no impurities of additional phases. This result indicates the possibility to adjust CuInS₂ films with p-type on n-type semiconducting character. Reaction times of 18 h or longer lead to the already known stoichiometric composition in the upper flaky region of the films and the Cu-rich compact layer.^[3] In addition it could be shown that the stoichiometric flaky structure of these films consisting of rods and outgrowing flakes possess different CuInS₂ modifications. FFT investigations of HRTEM images showed that the rods grow in a Wurtzite structure whereas the flakes grow in Chalcopyrite structure.

6.7 Chapter references

- [1] T. Yukawa, K. Kuwabara, K. Koumoto, *Thin Solid Films* **1996**, *286*, 151-153.
- [2] H. Bihri, M. Abd-Lefdil, *Thin Solid Films* **1999**, *354*, 5-8.
- [3] A. S. Wochnik, C. Heinzl, F. Auras, T. Bein, C. Scheu, *J. Mater. Sci.* **2012**, *47*, 1669-1676.
- [4] S. Peng, F. Cheng, J. Liang, Z. Tao, J. Chen, *J. Alloys Compd.* **2009**, *481*, 786-791.
- [5] O. V. Parasyuk, S. V. Voronyuk, L. D. Gulay, G. Y. Davidyuk, V. O. Halka, *J. Alloys Compd.* **2003**, *348*, 57-64.
- [6] C. Rincon, *Phys. Rev. B: Condens. Matter* **1992**, *45*, 12716-12719.
- [7] W.-C. Huang, C.-H. Tseng, S.-H. Chang, H.-Y. Tuan, C.-C. Chiang, L.-M. Lyu, M. H. Huang, *Langmuir* **2012**, *28*, 8496-8501.
- [8] D. Pan, L. An, Z. Sun, W. Hou, Y. Yang, Z. Yang, Y. Lu, *J. Am. Chem. Soc.* **2008**, *130*, 5620-5621.
- [9] Y. Qi, Q. Liu, K. Tang, Z. Liang, Z. Ren, X. Liu, *J. Phys. Chem. C* **2009**, *113*, 3939-3944.
- [10] B. Koo, R. N. Patel, B. A. Korgel, *Chem. Mater.* **2009**, *21*, 1962-1966.
- [11] A. Ghezelbash, B. A. Korgel, *Langmuir* **2005**, *21*, 9451-9456.
- [12] M. B. Sigman, Jr., A. Ghezelbash, T. Hanrath, A. E. Saunders, F. Lee, B. A. Korgel, *J. Am. Chem. Soc.* **2003**, *125*, 16050-16057.

7 Investigation of the growth of CuInS₂ microspheres

This chapter is based on the following publication:

Angela S. Wochnik, Anna Frank, Christoph Heinzl, Jonas Häusler, Julian Schneider, Ramona Hoffmann, Sonja Matich, Christina Scheu. *To be submitted.*

7.1 Introduction

Recently, the preparation of nano- and micro-structured semiconductor materials with biomaterial like morphologies has become of high interest in research^[1]. Due to the physical and chemical properties, applications in various areas for example as high surface materials for catalysis and structured materials can be found.^[1, 2] CuInS₂ is a non toxic wide-band gap I-III-VI₂ ternary chalcogenide semiconductor material with excellent electronic and optical properties.^[3, 4] It crystallizes in a tetragonal roquesite structure. The elementary cell contains eight tetrahedrons where the centers of each are occupied by S atoms, each coordinated by two Cu and two In atoms.^[5] CuInS₂ compound has been considered as a high attractive material for solar cell application and has been intensively studied. It exhibits a direct band gap of 1.5 eV and an absorption coefficient of $< 10^5 \text{ cm}^{-1}$.^[6] Depending on the synthesis, CuInS₂ is easy to convert into a n/p carrier type. Former studies showed that Cu-rich CuInS₂ can serve as a p-type semiconductor.^[7] Further investigations indicated that the increase of Cu improves the efficiency of solar cells.^[5, 8] The band gap energy is as well adjustable with the Cu- and In-concentration in the CuInS₂.^[9, 10] Due to its high performance and high output stability a further application as cathode material for photochemical devices is reviewed.^[11, 12] Numerous different structures and morphologies of CuInS₂ such as nanorods,^[13, 14] nanotubes,^[14] nanoparticles,^[15] foam-like nano-crystallites^[16] and microspheres have been successfully synthesized with different techniques like cost-intensive and extensive manufacturing methods, for example chemical vapor deposition,^[17] spray pyrolysis^[18]

and electro deposition,^[19] or via low cost methods like chemical bath deposition,^[20, 21] successive ionic layer deposition^[22] and mild solvothermal synthesis route.^[10] Via the solvothermal synthesis route different CuInS₂ microsphere could be observed by Qi et al.,^[1] Peng et al.,^[23] Hu et al.^[24] and Gou et al.^[25]. In a previous work we reported about the synthesis of CuInS₂ films via a mild solvothermal synthesis route modified from Peng et al.^[10] and the dependence of the thickness and morphology of the reactants concentration.^[26] In the present study we investigate the growth mechanism of the previously observed CuInS₂ microspheres which occur when a high concentration of reactants during the mild template free solvothermal synthesis is used. Additionally, we studied the morphology and the chemical compositions of the microspheres prepared at different reaction times.

7.2 Experimental details

7.2.1 Synthesis

The synthesis of CuInS₂ microspheres was performed via a mild solvothermal route adapted from Peng et al.^[10] and applied in our previous work.^[26] The used reagents were of analytical grade and used without further purification. Three differently synthesized types of microspheres were prepared, using different reaction times. In a teflon-lined stainless steel autoclave (20 ml) CuSO₄ · 5H₂O (0.03 M), InCl₃ (0.03 M) and thioacetamide (0.12 M) were dissolved in 10 ml ethanol and stirred for 15 min. The closed autoclave was heated at 160 °C for 12 h for sample 1, 150 °C for 18 h for sample 2 and at 150 °C for 24 h for sample 3. Afterwards the autoclaves were cooled down to room temperature in a water bath. The obtained black product was filtered, washed with ethanol and dried at air.

7.2.2 Characterization

The characterization of the microspheres was performed by different analytical techniques. X-ray diffraction (XRD) was used to investigate the crystal phase of the microspheres. Therefore a Bruker D8 Discovery diffractometer with CuK α radiation ($\lambda = 1.54 \text{ \AA}$) was applied. The 2θ range was 20 to 65° and the scanning rate 0.05°/s with a scanning speed of 0.1 s. The obtained patterns were compared to literature data or reference spectra. For the investigation of the morphology and the average chemical composition of the microspheres a Jeol JSM-6500F scanning electron microscope (SEM)

was used equipped with an energy dispersive X-ray (EDX) detector from Oxford Instruments (Inca Energy). The experiments were done with an acceleration voltage of 5.0 kV. Secondary electron (SE) imaging was executed using the attached Jeol standard detector. Additional investigation of the average chemical composition of the microspheres was performed via inductively coupled plasma atomic emission spectrometry (ICP-AES) using a VARIAN VISTA RL CCD Simultaneous ICP-AES. For the characterization of the growth and the investigation of the inner area of the microspheres a Zeiss NVision40 focused ion beam (FIB) microscope with integrated SEM was applied. For FIB cross-sectioning this microscope was used as well. The SEM investigation was done at 2.5 kV and the FIB sectioning was performed at 30 kV. The polishing of the TEM lamella was realized with 40 pA and 10 pA. For further characterization of the microstructure a transmission electron microscopy (TEM) was used. The TEM investigation was performed with a FEI Titan 80 – 300 ((S)TEM) microscope equipped with a Gatan Tridiem image filter and an EDAX EDX detector. The microscope is equipped with a high angle annular dark field (HAADF) detector from Fischione Instruments (Model 3000) for STEM imaging. The instrument was operated at 80 and 300 kV. The electron diffraction data were evaluated using a calibrated camera constant obtained by using a Si standard.

7.3 Results

The SEM images of the differently synthesized microspheres are displayed in Figure 7.1. The microspheres exhibit a size of 1-3 μm and the outer part is built out of several individual nano-flakes. Differently composed microspheres can be observed from particular reactions at 12 h (sample 1) and 18 h (sample 2) shown in Figure 7.1(a) and Figure 7.1(c) with on the one hand more compact nano-flakes in the following named microspheres A, and on the other hand more open and wide nano-flakes named microspheres B. In Figure 7.1(a) it can be seen that in sample 1 more microspheres of type A can be seen. Compared to this, in Figure 7.1(c) the microspheres of type B dominate. Figure 7.1(b) and (d) show a higher magnification of the mainly observed microsphere species of each sample. The sample 3 shown in Figure 7.1(e) reveals mostly microspheres B. In the higher magnification of sample 3 (Figure 7.1(f)), larger flakes growing on the surface of microspheres A can be noted. It seems that they will be transformed into microspheres B.

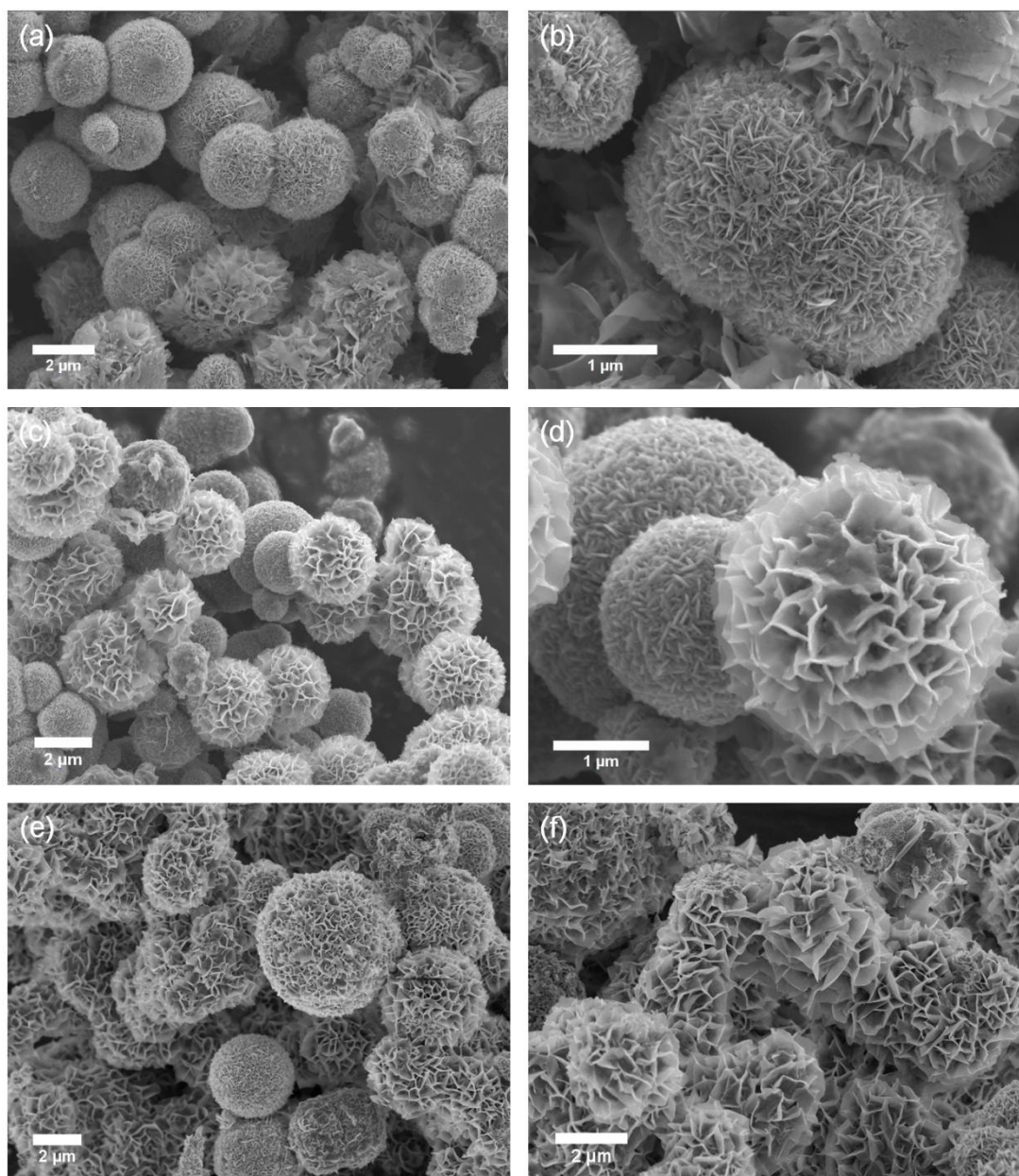


Figure 7.1: SE images illustrating the morphology of microspheres synthesized at different reaction times. The images show that the microspheres have a size of 1-3 μm and that the outer parts are built of individual nano-flakes. The samples 1 (12 h), 2 (18 h) and 3 (24 h), shown in Figure 7.1(a) 1(c) and 1(e), exhibit microspheres with rather compact nano-flakes on the surface (microspheres A) as well as such possessing a more open flaky surface structure (microspheres B). With longer reaction time the amount of microspheres B increases. The higher magnified images of sample 1 and 2 (Figure 7.1(b) and (d)) reveal the microstructure of the dominant microspheres species of each sample in detail. In Figure 7.1(f) it can be seen that on the surface of the compacter microspheres A a finer flaky structure occurs (right upper corner). Please note the different scale bars.

The quantification of several EDX measurements obtained in the SEM resulted for sample 1 in 26 ± 2 at% Cu, 24 ± 2 at% In and 50 ± 2 at% S and gives an average stoichiometric Cu:In:S composition of 1:1:2. The measurements for sample 2 resulted in 30 ± 2 at% Cu, 20 ± 2 at% In and 50 ± 2 at% S, that gives an average non-stoichiometric Cu:In:S composition of 1.5:1:2.5. The ICP-AES analysis verifies the EDX measurements in the SEM (for sample 1 = 1.1:1:2.1 and sample 2 = 1.3:1:2.5). Sample 3 was also analyzed with EDX in the SEM and gave a chemical composition of 29 ± 2 at% Cu, 22 ± 2 at% In and 49 ± 2 at% S resulting in a non stoichiometric composition of Cu:In:S = 1.3:1:2.2. The investigation of the crystal structure was realized by XRD measurements and the result is shown in Figure 7.2. The XRD pattern from sample 1 is given in Figure 7.2(a). The characteristic reflections of (112), (200), (204) and (132) from CuInS₂ in the tetragonal roquesite structure, with the lattice parameter of $a = 0.552$ nm and $c = 1.112$ nm, can be observed. Additional reflections with less intensity of CuS were found, which can be assigned to (004), (103), (006), (110), (108) and (116) planes of this phase (marked red). The XRD pattern from sample 2 (Figure 7.2(b)) also reveals the characteristic reflections of (112), (200), (204) and (132) belonging to CuInS₂. Additionally, further reflections (less intensive) were found and can be attributed to (200), (211), (400) and (422) from In₂S₃ (marked yellow). However, the reflections attributed to the (211) and (422) planes can also arise from the (100) and (200) of CuInS₂ in Wurtzite structure (marked blue). Reflections from CuS cannot be excluded which might be the (103) and (110) planes of this phase (marked red). In the XRD pattern of sample 3 most of the mentioned reflections of CuInS₂, CuS, In₂S₃ were found as well (spectra shown in associated content Figure 7.7). The observed 2θ values are summarized in Table 7.1 in comparison to literature data.

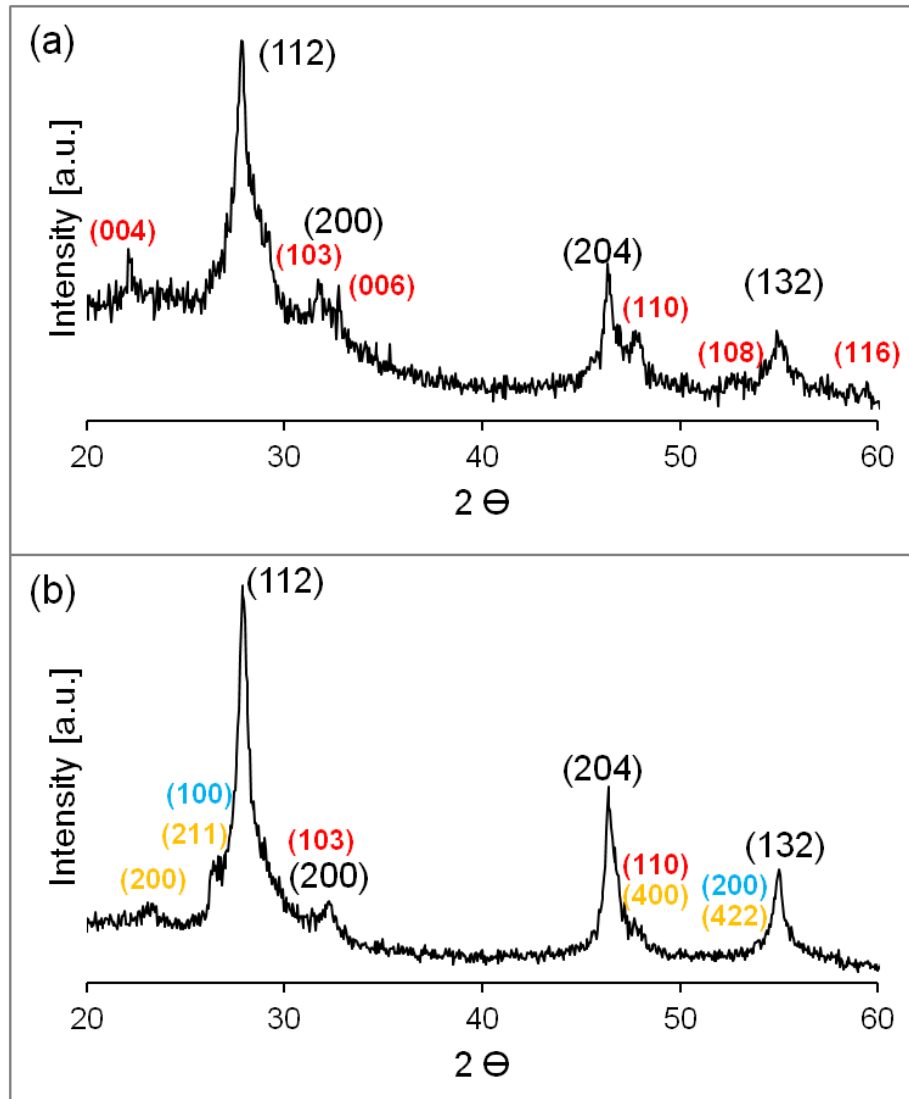


Figure 7.2: (a) XRD pattern of sample 1. Beside the characteristic reflections of CuInS₂, additional reflections of a minor CuS phase (marked red) can be observed. (b) XRD pattern of sample 2 reveals also the characteristic reflections of CuInS₂. Here, additional reflections are found, which can be attributed to In₂S₃ (marked yellow) and CuInS₂ in Wurtzite structure (marked blue).

Table 7.1: 2θ and d values observed in the X-ray and electron diffraction patterns from CuInS₂ in Roquesite and Wurtzite structure as well as CuS and In₂S₃ compared to literature data.^[27-30] 2θ values are listed in deg, d values in Å.

$d_{(obs)}$	$2\theta_{(obs)}$	CuInS ₂ Roquesite		CuInS ₂ Wurtzite		CuS		In ₂ S ₃	
		d	2θ	d	2θ	d	2θ	d	2θ
4.00	22.19	-	-	-	-	4.07 (004)	21.13	-	-
3.79	23.40	-	-	-	-	-	-	3.79 (200)	23.44
3.36	26.51	-	-	3.38 (100)	26.37	-	-	3.38 (211)	26.37
3.19	27.92	3.20 (112)	28.24	-	-	-	-	-	-
2.77	32.39	2.76 (200)	32.68	-	-	2.79 (103)	32.01	-	-
2.73	32.76	-	-	-	-	2.71 (006)	33.03	-	-
1.95	46.51	1.96 (204)	46.84	-	-	-	-	-	-
1.90	47.81	-	-	-	-	-	-	1.90 (400)	47.81
1.89	48.00	-	-	-	-	1.88 (110)	48.31	-	-
1.73	52.73	-	-	-	-	1.72 (108)	53.06	-	-
1.68	54.30	-	-	1.69 (200)	54.20	-	-	1.69 (422)	54.30
1.66	55.15	1.67 (132)	55.36	-	-	-	-	-	-
1.55	59.46	-	-	-	-	1.54 (116)	59.77	-	-

Figure 7.3 displays the SE images from sample 2 taken by FIB/SEM after sectioning with Ga ions. The images reveal that the microspheres are compact in the middle and that the flaky structure is only established at the outer shell. Figure 7.3(a) shows a sliced microsphere with a more compact flaky structure (microsphere A). Here the shell is

around 200 nm thick. Figure 7.3(b) reveals a sliced microsphere B with the open and wide flaky structure, which has a thickness of about 460 nm. Additionally, a different contrast can be observed in the outer area of the compact core (marked with a white dotted line).

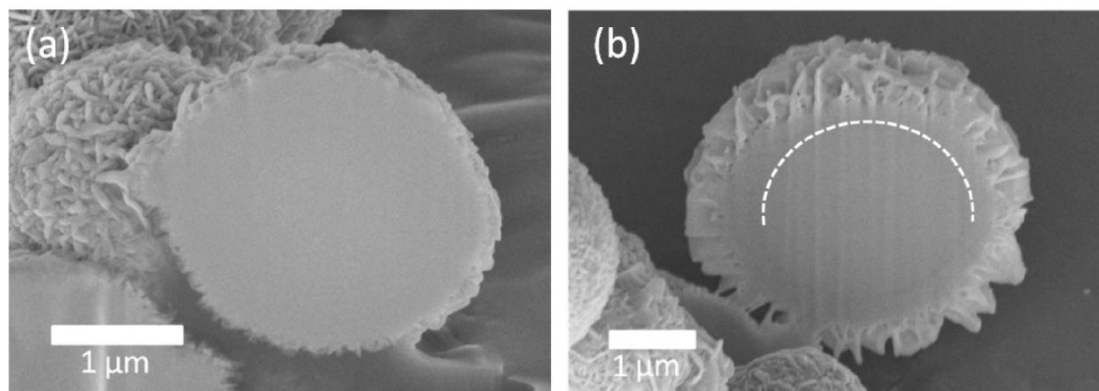


Figure 7.3: SE images from two sliced microspheres taken by FIB/SEM. The microspheres reveal a compact core with a flaky structure on the outside. Figure 7.3(a) shows a sliced microsphere A, with a compact flaky structure of around 200 nm. Figure 7.3(b) reveals a cross-section of microsphere B with the more open and wide flaky structure. The flakes exhibit a thickness of around 460 nm. The core indicates a phase contrast in the outer area (marked with a white dotted line).

To investigate the growth mechanism of the different microspheres, TEM lamellae were prepared from sample 1 and 2 with FIB sectioning. Additionally, a TEM sample from sample 2 was prepared with a conventional TEM sample preparation method to exclude alteration caused by ion milling in the FIB. In the HAADF-STEM image in Figure 7.4(a) the overview of the TEM lamella from sample 1 is shown. The microspheres located in this lamella are only from the sphere type B, which possesses a compact core surrounded by a flaky structure. This flaky structure consists of many individual rods and outgrowing flakes, which was also obtained and characterized for CuInS₂ thin films, as we reported earlier.^[26] Additionally, at higher magnification in the bright field TEM image in Figure 7.4(b) a phase contrast (bright ring) can be observed inside the microspheres. This indicates a higher amount of In at this area. Diffraction patterns were taken from a circular area with a diameter of 150 nm and indicate that the areas are polycrystalline. The diffraction pattern, taken in the middle of the microsphere and in the outer area at the phase contrast, show only the characteristic reflections for (112) (204) and (132) planes of CuInS₂. No further reflections can be found. Beside this the

diffuse rings in the diffraction pattern indicate small crystal sizes. For the diffraction pattern taken in the flaky area, additionally (103) and (110) reflections from CuS were found (marked red) beside the reflections from CuInS₂. These reflections are also observed in the XRD pattern from sample 1 in Figure 7.2(a). The found d values are summarized in Table 7.1 in comparison to literature data.

The ADF/HAADF-STEM image in Figure 7.4(c) reveals an overview of the TEM lamella of sample 2. Figure 7.4(d) shows a cross-section microsphere ADF/HAADF-STEM image at higher magnification of type B with more open flakes, consisting of rods and flakes as described for sample 1.^[26] The image reveals that the microsphere exhibits a porous core followed by a compact area and a flaky structure at the outside. The flaky structure is about 460 nm thick. This property can also be observed for the microspheres shown in Figure 7.4(c). To draw conclusions to the growth of the microspheres we investigated the crystal structure at the different areas with electron diffraction experiments. The diffraction pattern taken in the middle of the microsphere (Figure 7.4(d) (marked with the white arrow) gives the characteristic reflections of CuInS₂ in the Roquesite crystal structure. The observed values correspond well to the d values of the (112), (200), (204) and (132) planes (compare Table 7.1). Additional reflections were found (marked red dotted), which match to the d values of (103) and (110) from CuS. However, the reflection attributed to the (110) of CuS matches also to the (400) of In₂S₃. Another reflection at $d = 3.36 \text{ \AA}$ (marked yellow) was found which matches to the d value of the (211) plane of In₂S₃ as well as to the (100) plane of CuInS₂ in the Wurtzite structure. This could be also found in the XRD pattern from the sample 2 (Figure 7.2(b)). The diffraction pattern taken at the compact area between the porous core and the flaky structure shows only the typical d values from CuInS₂ which correspond to (112) (204) and (132) planes (marked white). No further reflections can be observed. However, this area seems to consist of smaller crystals. The diffraction pattern taken in the flaky area gives again the characteristic reflections from CuInS₂. Additional reflections from (103) and (110) planes of CuS were found (marked red). Also a reflection at $d = 0.336 \text{ \AA}$ could be observed here which can again originate from In₂S₃ or CuInS₂ in Wurtzite structure.

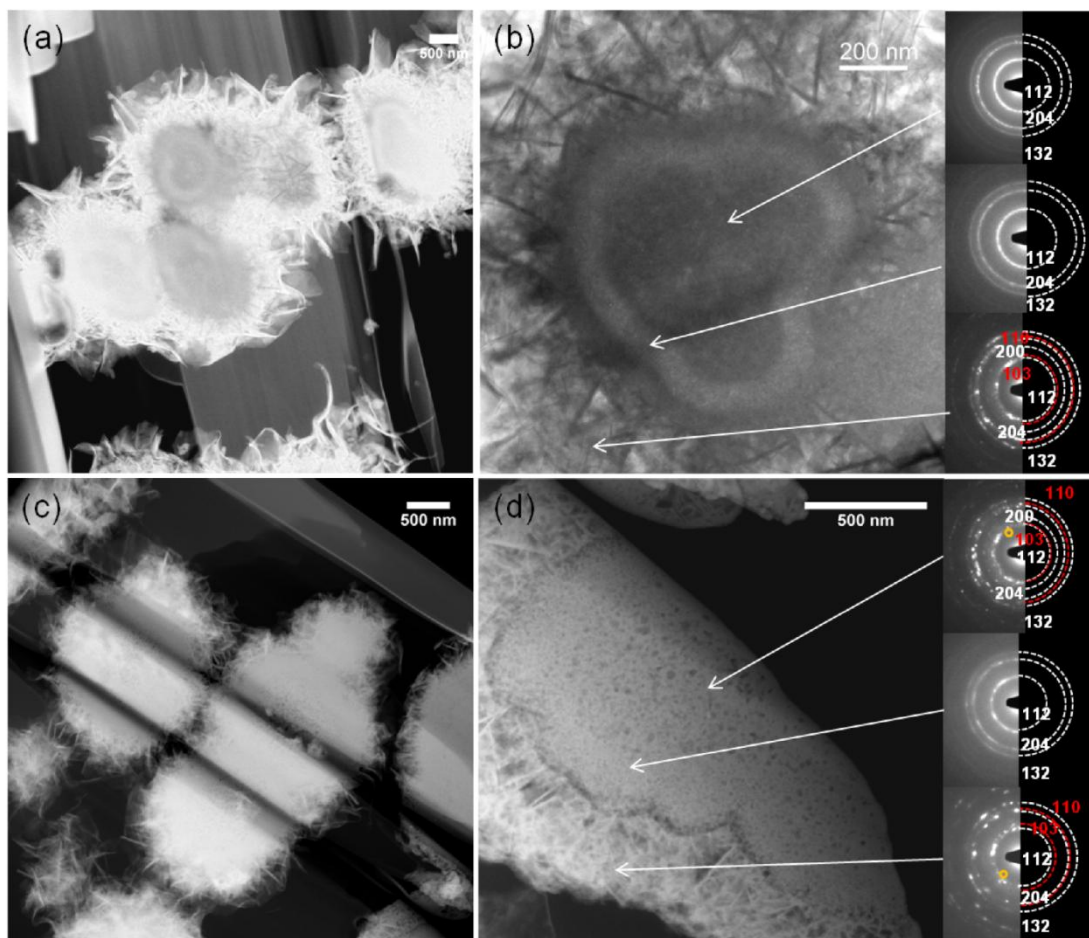


Figure 7.4: (a) reveals an overview ADF/HAADF-STEM image of the lamella from sample 1. The ADF/HAADF-STEM image in (b) shows a cross-section of a microsphere B at higher magnification. The bright field TEM image indicates that the core is compacted with a flaky structure at the outside. Additionally, a phase contrast can be observed inside the microsphere. (c) ADF/HAADF-STEM image shows the overview of the TEM lamella from sample 2, consisting of sliced microspheres of type B. (d) The image reveals that the microsphere exhibits a porous core followed by a compact area and a flaky structure at the outside. Diffraction patterns were taken at various locations as indicated by the arrows.

The investigation of the chemical composition of the microspheres was done with EDX measurements in the TEM in STEM mode at 80 and 300 kV with a spot size of about 1 nm. Numerous spectra were taken at different positions of several microspheres. The EDX measurements from the microspheres B obtained of the TEM lamella from sample 1 (Figure 7.4(a), (b)) resulted in a stoichiometric Cu:In:S composition of 1:1:2 in the middle and a Cu:In:S composition of 1.2:1:2.1 in the flakes. EDX measurements

performed at the phase contrast (bright ring in the microsphere (Figure 7.4(b)) gives a chemical composition of 0.8:1:1.5. This result proves a higher amount of In in this area.

The quantification of the spectra from the microspheres B of the TEM lamella in sample 2 (Figure 7.4(c), (d)), taken in the middle of the microspheres, give a chemical composition of Cu:In:S of 1.9:1:3.5. The spectra taken at the compact area between the porous core and the flakes indicate a Cu:In:S composition of 0.96:1:2.03 and in the flaky area of Cu:In:S = 0.9:1:1.9. Additionally, at the interface between the core and the flaky structure, some areas were found which show a high amount in In and less Cu and S. Here the quantification gives a composition of Cu:In:S = 0.5:1:0.6. The quantification of the spectra taken of the microspheres B found in the conventional prepared TEM specimen from sample 2 (images not shown) confirmed the results obtained from the measurements of the FIB lamella. Additionally, microspheres A could be observed in this TEM specimen. These microspheres gave for the spectra taken at different positions a stoichiometric composition of 1:1:2.

7.4 Discussion

According to the different reaction times we found two different microspheres A with a more compact surface structure and B with a more wide and open flaky surface structure. With increased reaction time species B dominates. The TEM investigations of the various microspheres synthesized at varied reaction times gave distinct chemical compositions. To understand the different morphology and composition of the obtained microspheres A and B further experiments were done. Under the same reaction condition as for sample 2 (18 h, 150 °C), we investigated the reaction between InCl₃ and thioacetamide as well as between CuSO₄ and thioacetamide. For the reaction without the copper precursor, In₂S₃ was formed as a yellow solid. This was proofed by XRD measurement (spectra shown in associated content Figure 7.8). The reaction without InCl₃ leads to a black solid. The XRD measurements were not distinct. Out of this reason, the reaction product was investigated using TEM. Nanoparticles in different shape and sizes were observed. Electron diffraction patterns taken at different agglomerates showed reflections either from CuS or Cu₂S. The observed 2θ values are summarized in

Table 7.2 in comparison to literature data shown in associated content. Bright field images of the obtained nanoparticles and the belonging electron diffraction pattern are shown in Figure 7.9(a) and Figure 7.9(b) (associated content). The percentage of CuS was predominating. According to literature it is known that in aqueous solution copper sulfate and thioacetamide react under H_2S formation to CuS , Cu_2S and S .^[31] Gibbs phase triangle of the system $\text{Cu} - \text{In} - \text{S}$ shows the possibility of the formation of CuInS_2 out of CuS or Cu_2S and In_2S_3 .^[32-34] In Figure 7.5 the observed microspheres B with the different chemical compositions of sample 1 and 2 are schematically illustrated. In Figure 7.5(a) a microsphere with a stoichiometric core, an In-rich zone and stoichiometric flakes (slightly higher Cu percentage, CuS is also obtained with XRD measurements, Figure 7.2(a), and electron diffraction, see Figure 7.4(b)) is drawn. This type of microsphere B was mainly found in sample 1 with a reaction time of 12 h (named B1). The other type of microspheres B is given in Figure 7.5(b) and occurs mainly in sample 2 with a reaction time of 18 h (named B2). Here we found a Cu-rich core, followed by a thin stoichiometric area. Close to the stoichiometric flakes a higher amount of In was detected by EDX measurements in the TEM in STEM mode. CuS could also be observed with XRD measurements and electron diffraction (see Figure 7.2(b) and Figure 7.4(d)). In_2S_3 or CuInS_2 in Wurtzite structure (phase transformation) cannot be excluded because of the additionally reflections in XRD and electron diffraction patterns.

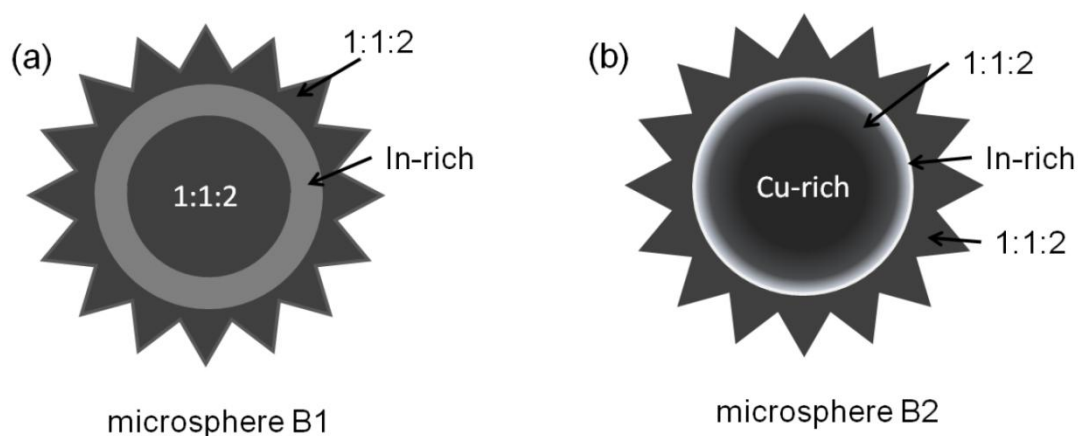


Figure 7.5: Schematically illustration of the different chemical compositions found for microspheres B in sample 1 and 2. Microstructure (a) is mainly found in sample 1 (B1) and (b) in sample 2 (B2).

Due to the electron diffraction patterns of the core of sample 1 and 2 (Figure 7.4), which indicates smaller crystals for sample 1 compared to sample 2, we conclude that they are built up of different sized precursor particles (CuS or/and Cu₂S, In₂S₃) because of the different reaction times. Smaller particles, built after 12 h, can form CuInS₂ spheres faster and with a more stoichiometric composition, whereas bigger particles, built after 18 h, cannot complete the formation of CuInS₂ over the whole sphere and lead to non stoichiometric cores. The microspheres with stoichiometric composition are named A1 in the following and the non stoichiometric spheres A2. In Figure 7.6 we show our proposed growth mechanism for each type of microsphere. The growth mechanism of sample 1 is described in Figure 7.6(a). For the shorter reaction time smaller precursor particles agglomerate to form microspheres A1, with a stoichiometric composition. Some of these microspheres A1 can turn into microspheres B1. In the case of sample 2 the growth mechanism is described in Figure 7.6(b). During the longer reaction time larger precursor particles are built, which can agglomerate to Cu-rich microspheres A2 (not proofed). Most of these microspheres A2 can grow to microspheres B2. Conversion of microspheres B1 into B2 during longer reaction times cannot be excluded because of possible phase transformation, solid diffusion or decomposition of the core (porosity was observed during TEM investigations; see Figure 7.4(d)). For example, Qi et al. described CuInS₂ hollow microspheres and proposed a decomposition of the core (see discussion below).^[1]

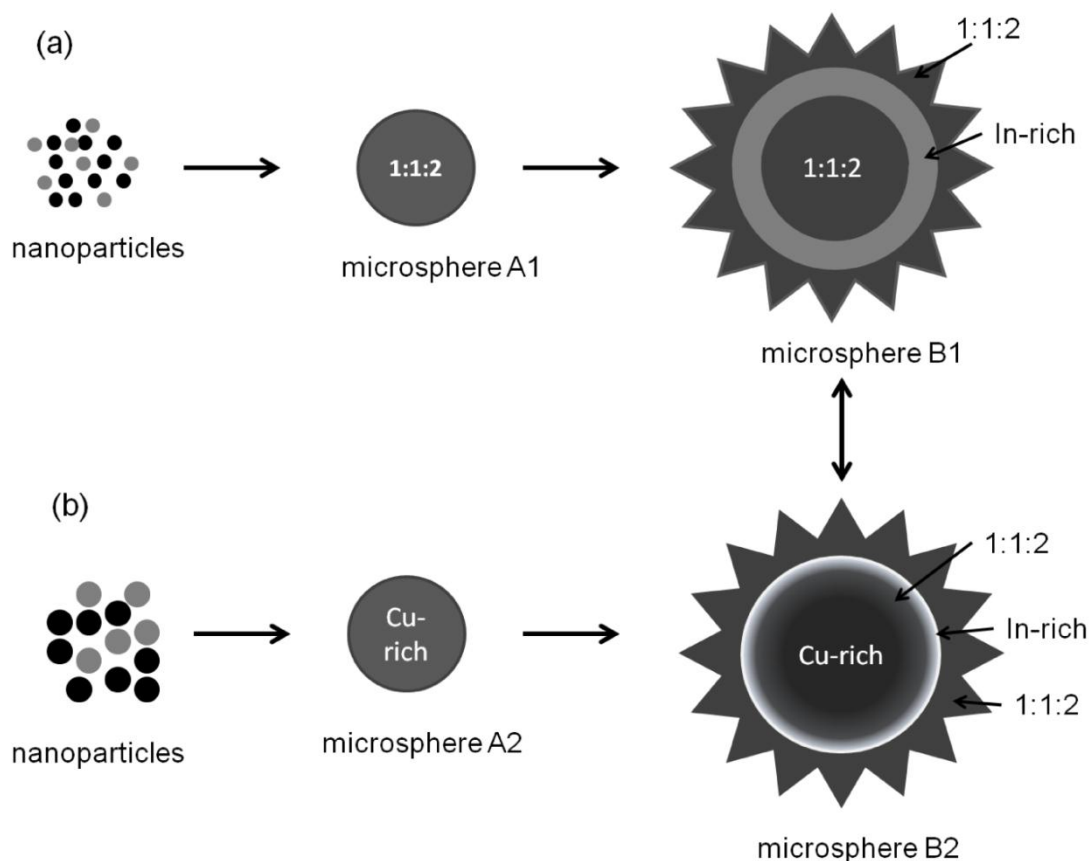


Figure 7.6: Proposed growth mechanism of the obtained microspheres in sample 1 and 2. In (a) the formation of CuInS₂ microspheres A1 and B1 begins out of smaller nanoparticles because of shorter reaction times (sample 1, 12 h). Here a more stoichiometric composition is detected. In (b) the formation of the second microsphere type A2 and B2 out of bigger particles is shown (sample 2, 18 h). The composition of these spheres is non stoichiometric over the whole sphere.

The In-rich areas in the microspheres B result from distinct attachment of nanoparticles at the outer shell. For example, if In₂S₃ is added to a Cu-rich sphere, In could diffuse inside to form stoichiometric CuInS₂. The formation of CuInS₂ out of solid CuS and In₂S₃ is also known in literature. Peña et al. described the formation of CuInS₂ via chemical bath deposition of In₂S₃-CuS thin films.^[35] Perhaps solid diffusion plays an important role in this case, as we assume for our samples. The presence of microspheres B2 in sample 1 (and the other way around) cannot be excluded.

Comparison with literature

Qi et al.^[1] synthesized porous CuInS₂ hollow microspheres. With a template free one step solvothermal synthesis route they were able to prepare CuInS₂ microspheres constructed by nanoparticles and nanoflakes. For their synthesis they used InCl₃·4H₂O, CuSO₄·5H₂O, thiourea and *N,N*-dimethylformamide (DMF). The standard reaction was realized at 160 °C for 25 h. The obtained black product was characterized with XRD, SEM, TEM and UV-VIS. To investigate the growth mechanism, they used XRD and TEM studies from microspheres synthesized at 3 h, 4 h, 7.5 h and 15 h. They discovered that the microspheres synthesized at 3 h consist of nanoparticles and nanoflakes and exhibits a core. In the XRD and electron diffraction pattern taken in the TEM they found reflections from CuInS₂ and CuS. The CuS phase disappeared after 15 h and the microspheres became hollow. This was explained by the theory that CuS nanoflake microspheres did not only undergo a hollowing process but also go through a further phase transformation. The growth mechanism is described by Qi et al. as followed: In the case of the nanoparticle microspheres DMF works as reductant and solvent. Cu²⁺ ions are reduced to Cu⁺ by DMF and reacts with In³⁺ and S²⁻ to form CuInS₂ nanoparticles. This nanoparticles form nanoparticle-spheres. A sufficient drifting force leads to the formation of a primary core. With second crystallization on the external surface the shell continued to grow and the core disappears. In the case of the microspheres consisting of nanoflakes still unreduced Cu²⁺ ions exist which react with S²⁻ to CuS. The originated CuS spheres act as template and copper source. CuS nanoparticles on the surface of the spheres are reduced to Cu₂S, which reacts in-situ with In³⁺ and S²⁻ to CuInS₂ nanoparticles coated on the surface of the primary formed CuS spheres. By dissolving CuS nanoparticles a hole is forming. Dissolved CuS is also reduced to Cu₂S and the reaction with In³⁺ and S²⁻ to CuInS₂ finally is a second crystallization on the external surface.

Peng et al.^[23] synthesized CuInS₂ microspheres with a solvothermal synthesis route using InCl₃·4H₂O, CuSO₄·5H₂O, thioacetamide and ethanol. The reaction was realized at 160 °C for 36 h. The characterization of the product was done by XRD, SEM, IR spectroscopy and UV-VIS. The influence of the synthesis conditions on morphology was studied by altering solvents, reactants and the variation of reaction temperatures and heating. Different microspheres with different microstructures built of diverse

nanoflakes and nanocrystals with different sizes were obtained. Compared to our morphology some of their microspheres are similar but most differ in the morphology and average chemical composition due to the use of different reagents. A detailed structure investigation using TEM was not performed by Peng and co-workers.

Hu et al.^[24] reported about the large-scale growth of porous CuInS₂ microspheres. In their work they used InCl₄·4H₂O, CuSO₄·5H₂O, KSCN or thiourea as sulfur source and ethylene glycol as solvent. The reaction conditions were 200°C for 12 h. The characterization of the product was realized by XRD and SEM. The microsphere looks slightly similar compared to the microspheres obtained in our work. However no further investigations were done to determine the crystal structure and composition on the nanometer scale.

Gou et al.^[25] prepared CuInS₂ microspheres via a solvothermal synthesis method with thioglycolic acid as sulfur source. Further reactants were InCl₄·4H₂O and CuSO₄·5H₂O. Water or ethanol was used as solvent. They characterized the obtained product with XRD, SEM and UV-VIS spectroscopy. The results of their XRD measurements show beside CuInS₂ impurities of Cu₂S, CuS and In₂S₃. The SEM images of their products consist of highly monodispersive spheres with diameters of 2 – 5 μm with a distinct surface microstructure. The surface morphology of their microspheres depends on the concentration of the sulfur source and the used solvent. The morphology of the obtained microspheres by Gou et al. is not comparable with our synthesized microspheres. The different distinct surface microstructure is ascribed to the different used sulfur source.

7.5 Conclusion

In conclusion, we reported about a mild, template free solvothermal method to prepare CuInS₂ microspheres. For three samples with different reaction conditions (sample 1, 12 h, 160 °C; sample 2, 18 h, 150 °C and sample 3, 24 h, 150 °C) we obtained two distinct microspheres in the SEM. On the one hand we found microspheres named A with a more compact structure, and on the other hand microspheres named B with a more open, flaky structure. With increasing the reaction time microspheres B dominate. EDX measurements in the SEM gave an average composition of Cu:In:S for sample 1 of 1:1:2, for sample 2 of 1.5:1:2.5 and for sample 3 of 1.3:1:2.2. These results could be proofed with ICP-AES analysis for sample 1 and 2. To take a look inward the microspheres we sliced some of them in the FIB/SEM microscope. We found that the microspheres are compact in the middle with a flaky shell. It was also possible to prepare a TEM lamella for detailed characterizations. Thus we found two different chemical compositions for microspheres B according to the different reaction times. The microspheres B1 obtained for shorter reaction times seem to be compact with a stoichiometric composition and consist of smaller crystals. Additionally, an In-rich shell was found. In contrast, microspheres B2 consist of larger crystals due to the longer reaction time and seem to be porous in the core. The composition is Cu-rich in the core, followed by a compact stoichiometric area and also In-rich areas close to the flaky structure. In both cases, the obtained flakes on the shell have a nearly stoichiometric composition. XRD and electron diffraction patterns gave, beside CuInS₂, also reflections from CuS and In₂S₃. Out of these results we were able to propose a growth mechanism for the obtained microspheres.

7.6 Associated content

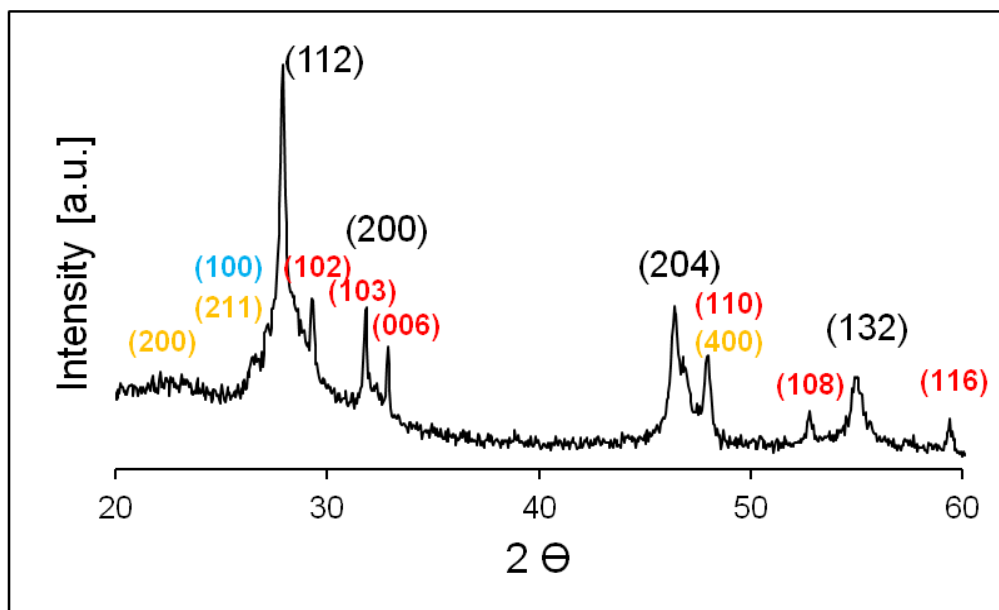


Figure 7.7: XRD pattern of sample 3 (24 h). Reflections of CuInS₂, CuS (red) and In₂S₃ (yellow) are assigned. The additional presence of CuInS₂ in Wurtzite structure cannot be excluded (reflection marked blue).

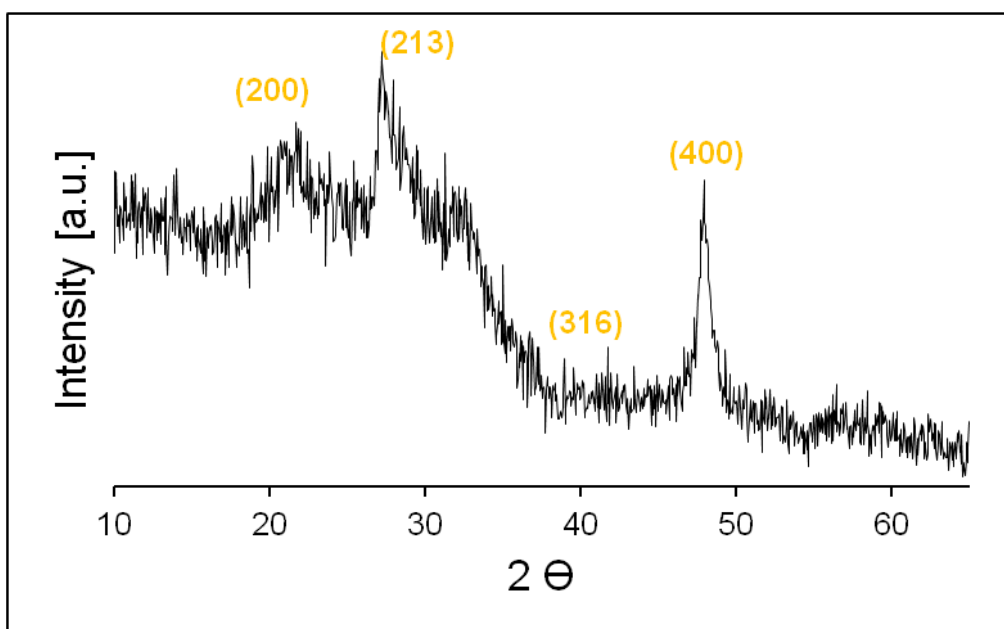


Figure 7.8: XRD pattern obtained from the reaction of InCl₃ and thioacetamide in ethanol for 18 h at 150 °C. Sharp reflections of In₂S₃ can be observed (marked yellow). The amorphous background can be attributed to the remaining organic material.

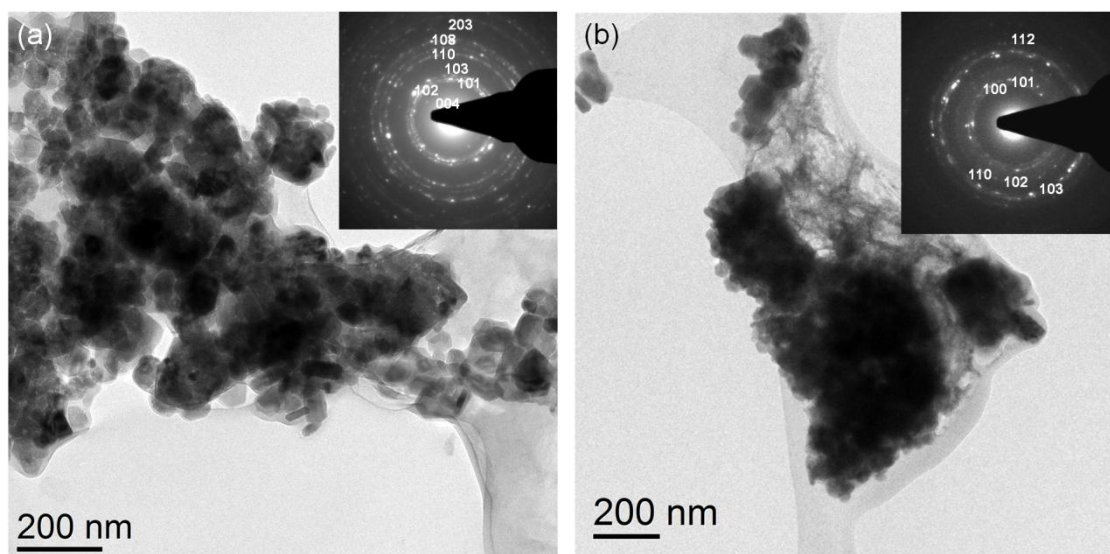


Figure 7.9: Bright field TEM images of the reaction between CuSO₄ and thioacetamide in ethanol for 18 h at 150 °C. (a) Mainly agglomerated CuS particles were formed and confirmed by electron diffraction.^[29] (b) shows the agglomeration of Cu₂S nanoparticles. The reflections in the electron diffraction pattern can be attributed to β-Cu₂S (Chalcocite).^[36]

Table 7.2: 2θ and d values observed in the electron diffraction patterns from CuS and Cu₂S compared to literature data^[29, 36]. 2θ values are listed in deg, d values in Å.

$d_{(obs)}$	CuS		Cu ₂ S	
	d	2θ	d	2θ
4.00	4.07 (004)	21.13	-	-
3.36	-	-	3.36 (100)	26.50
3.19	3.20 (101)	27.78	-	-
3.00	3.03 (102)	29.43	3.01 (101)	29.75
2.77	2.79 (103)	32.01	-	-
2.73	2.71 (006)	33.03	-	-
2.37	-	-	2.40 (102)	37.41
1.95	-	-	1.95 (110)	46.54
1.89	1.88 (110)	48.31	1.86 (103)	48.94
1.73	1.72 (108)	53.06	-	-
1.68	-	-	1.68 (112)	54.55
1.57	1.56 (203)	59.77	-	-

7.7 Chapter references

- [1] Y. Qi, K. Tang, S. Zeng, W. Zhou, *Microporous Mesoporous Mater.* **2008**, *114*, 395-400.
- [2] D. G. Shchukin, H. Moehwald, *Langmuir* **2005**, *21*, 5582-5587.
- [3] S. Schorr, V. Riede, D. Spemann, T. Doering, *J. Alloys Compd.* **2006**, *414*, 26-30.
- [4] Q. Lu, J. Hu, K. Tang, Y. Qian, G. Zhou, X. Liu, *Inorg. Chem.* **2000**, *39*, 1606-1607.
- [5] M. Reitinger, D. Offerlbauer, P. H. Louf, P. Schattschneider, D. S. Su, E. Zeitler, *Micron* **2000**, *32*, 141-146.
- [6] B. Tell, J. L. Shay, H. M. Kasper, *Phys. Rev. B* **1971**, *4*, 2463.
- [7] T. Yukawa, K. Kuwabara, K. Koumoto, *Thin Solid Films* **1996**, *286*, 151-153.
- [8] H. W. Schock, *Sol. Energy Mater. Sol. Cells* **1994**, *34*, 19-26.
- [9] T. Todorov, E. Cordocillo, J. F. Sanchez-Royo, J. Carda, P. Escribano, *Chem. Mater.* **2006**, *18*, 3145-3150.
- [10] S. Peng, F. Cheng, J. Liang, Z. Tao, J. Chen, *J. Alloys Compd.* **2009**, *481*, 786-791.
- [11] S. Ikeda, T. Nakamura, S.-M. Lee, T. Yagi, T. Harada, T. Minegishi, M. Matsumura, *ChemSusChem* **2011**, *4*, 262-268.
- [12] D. Cahen, G. Dagan, Y. Mirovsky, G. Hodes, W. Girit, M. Lubke, *J. Electrochem. Soc.* **1985**, *132*, 1062-1070.
- [13] J. Xiao, Y. Xie, R. Tang, Y. Qian, *J. Solid State Chem.* **2001**, *161*, 179-183.
- [14] Y. Jiang, Y. Wu, S. Yuan, B. Xie, S. Zhang, Y. Qian, *J. Mater. Res.* **2001**, *16*, 2805-2809.
- [15] S. Han, M. Kong, Y. Guo, M. Wang, *Mater. Lett.* **2009**, *63*, 1192-1194.
- [16] G. Z. Shen, D. Chen, K. B. Tang, Z. Fang, J. Sheng, Y. T. Qian, *J. Cryst. Growth* **2003**, *254*, 75-79.
- [17] J. A. Hollingsworth, K. K. Banger, M. H. C. Jin, J. D. Harris, J. E. Cowen, E. W. Bohannon, J. A. Switzer, W. Buhro, A. F. Hepp, *Thin Solid Films* **2003**, *431*, 63-67.
- [18] M. C. Zouaghi, T. Ben Nasrallah, S. Marsillac, J. C. Bernede, S. Belgacem, *Thin Solid Films* **2001**, *382*, 39-46.
- [19] S. i. Kuranouchi, T. Nakazawa, *Sol. Energy Mater. Sol. Cells* **1998**, *50*, 31-36.
- [20] H. M. Pathan, C. D. Lokhande, *Appl. Surf. Sci.* **2004**, *239*, 11-18.
- [21] P. Guha, D. Das, A. B. Maity, D. Ganguli, S. Chaudhuri, *Sol. Energy Mater. Sol. Cells* **2003**, *80*, 115-130.
- [22] Y. Shi, Z. Jin, C. Li, H. An, J. Qiu, *Appl. Surf. Sci.* **2006**, *252*, 3737-3743.
- [23] S. Peng, J. Liang, L. Zhang, Y. Shi, J. Chen, *J. Cryst. Growth* **2007**, *305*, 99-103.
- [24] H. Hu, B. Yang, X. Liu, R. Zhang, Y. Qian, *Inorg. Chem. Commun.* **2004**, *7*, 563-565.
- [25] X. Gou, S. Peng, L. Zhang, Y. Shi, J. Chen, P. Shen, *Chem. Lett.* **2006**, *35*, 1050-1051.
- [26] A. S. Wochnik, C. Heinzl, F. Auras, T. Bein, C. Scheu, *J. Mater. Sci.* **2012**, *47*, 1669-1676.
- [27] I. V. Bodnar', I. T. Bodnar, A. A. Vaipolin, *Cryst. Res. Technol.* **1984**, *19*, 1553-1557.
- [28] Q. Yunxia, L. Qiangchun, T. Kaibin, L. Zhenghua, R. Zhibiao, L. Xianming, *Journal of Physical Chemistry, American Chemical Society* **2009**, *113*, 3939-3944.
- [29] H. Fjellvag, F. Gronvold, S. Stolen, A. F. Andresen, R. Mueller Kaefer, A. Simon, Z. *Kristallogr.* **1988**, *184*, 111-121.
- [30] N. S. Rampersadh, A. M. Venter, D. G. Billing, *Physica B: Condensed Matter* **2004**, *350*, e383-e385.
- [31] H. Hofmann, G. Jander, *Qualitative Analyse*, 1 ed., **1992**.
- [32] S. Fiechter, Y. Tomm, M. Kanis, R. Scheer, W. Kautek, *Phys. Status Solidi B* **2008**, *245*, 1761-1771.

- [33] J. J. M. Binsma, L. J. Giling, J. Bloem, *J. Cryst. Growth* **1980**, *50*, 429-436.
- [34] S. Fiechter, K. Diesner, Y. Tomm, *Inst. Phys. Conf. Ser.* **1998**, *152*, 27-30.
- [35] Y. Pena, S. Lugo, M. Calixto-Rodriguez, A. Vazquez, I. Gomez, P. Elizondo, *Appl. Surf. Sci.* **2010**, *257*, 2193-2196.
- [36] N. V. Belov, Butuzov, V.P., *Doklady Akademii Nauk SSSR* **1946**, *54*, 717.

8 L-cysteine assisted growth of CuInS₂ films

This chapter is based on the following publication:

Angela S. Wochnik, Anna Frank, Thomas Bein and Christina Scheu. *To be submitted.*

8.1 Introduction

In recent years, the development of alternative semiconductor materials for solar cells has become a very active research field. The requirements for these materials include low cost, efficient manufacturing processes, as well as low toxicity. Several of these features can be found in copper indium disulfide (CuInS₂), which became one of the most popular and promising candidates for absorber materials in photovoltaic applications. Additional advantages of this material include its good long-term stability, a high absorption coefficient ($\alpha \approx 10^5 \text{ cm}^{-1}$) and a direct band gap of 1.53 eV.^[1] In particular, CuInS₂ is less toxic than CuInSe₂.^[2] Known manufacturing methods include for example chemical vapor deposition,^[3] spray pyrolysis^[4] and electro deposition.^[5] Moreover, CuInS₂ films can be obtained via low-cost methods such as chemical bath deposition,^[6, 7] successive ionic layer deposition^[8] and mild solvothermal synthesis routes.^[9] In a previous paper, we have presented the synthesis of CuInS₂ thin films using a simple, low-cost solvothermal method that had been developed by Peng et al.^[9] and modified in our study. Depending on the reagent stoichiometry and thermal treatments, we were able to synthesize CuInS₂ films with different thicknesses and morphologies, using thioacetamide as a sulfur source.^[10] However, thioacetamide is a toxic and carcinogenic substance. Hence, to prepare CuInS₂ thin films via a nontoxic route, we developed an alternative route by changing the sulfur source to L-cysteine and modifying the synthesis conditions accordingly.

Biomolecule-assisted synthesis has proven to be a novel, environmentally friendly and promising method to prepare various nanomaterials, making use of the unique features of biomolecules including the capability to engage in self-assembly processes.^[11] Biomaterials such as proteins, DNA, peptides and amino acids have been used to control

the size and shape of various nanomaterials.^[12, 13] L-cysteine [Cys, HSCH₂CH(NH₂)COOH] is a thiol-containing amino acid that is inexpensive and environmentally friendly. Additionally, it has a strong affinity to metal ions to form metal-ligand complexes which can be used as precursor for the synthesis of sulfidic nanocrystals.^[14] L-cysteine-assisted synthesis strategies involving solvothermal processes for preparing, e.g. PbS, Bi₂S₃, Ag₂S, In₂S₃ and CuInS₂ nanostructures such as nanocrystals and microspheres, have been reported.^[11-16] Liu et al.^[11] synthesized CuInS₂ nanocrystals via a L-cysteine-assisted growth using a solvothermal process. They obtained a product containing agglomerations of irregular microspheres and nanocrystals. Wen et al.^[16] produced CuInS₂ powders using L-cysteine as sulfur source. The powders consisted of microspheres made up of nanosheets. The thickness of the nanosheets was found to vary from 50 to 100 nm.

To the best of our knowledge, there have been no reports on the synthesis of CuInS₂ thin films using L-cysteine or another amino acid as the sulfur source. Herein we report about a solvothermal route to prepare CuInS₂ films on fluorine-doped tin oxide (FTO) conductive glass substrate by using L-cysteine as sulfur source. With this method we are able to prepare films with different thicknesses and morphologies by varying the concentration of reactants.

8.2 Experimental details

All reagents were of analytical grade and were used without further purification. Fluorine-doped tin oxide conductive glass (Pilkington) with dimensions of 15 x 15 x 2 mm was used as substrate for the deposition of the CuInS₂ films. All substrates were washed in dilute nitric acid, acetone, doubly-distilled water and ethanol in an ultrasonic cleaner for 5 min respectively. The reaction procedure to grow the films was adapted from Peng et al.^[9] and from our previous work^[10]. Only the sulfur source was changed from thioacetamide to L-cysteine. Three films were prepared using different concentrations of reactants, hereafter referred to as films A, B and C, respectively. In a teflon-lined stainless steel autoclave (20 ml) CuSO₄ · 5H₂O (A: 0.06 M, B: 0.02 M, C: 0.01 M), InCl₃ (A: 0.06 M, B: 0.02 M, C: 0.01 M), and L-cysteine (A: 0.15 M, B: 0.05 M, C: 0.03 M) were dissolved in 10 ml ethanol and stirred for 15 min (summarized in Table 8.1). The pH of the reaction solution was around 5, which is the

isoelectric point of L-cysteine. The cleaned substrates were placed diagonally, with the FTO surface pointing downwards, in the teflon liner and were completely immersed in the solvent. The closed autoclave was heated at 150 °C for 18 h and cooled down to room temperature in a water bath. The obtained black to brownish films were washed using doubly-distilled water and ethanol and dried with compressed air. The films displayed a thickness gradient which means that the films appeared darker at the lower end, where the substrate was deposited at the bottom of the autoclave and brighter on the other end. Variation of reaction time, temperature and positioning of the substrate in the autoclave does not influence the homogeneity, morphology and thickness of the films in a drastically fashion. Because of the best results with the named conditions the further characterization was done on the brighter, thinner parts of the films A, B and C.

Table 8.1: Different concentrations of reactants of the three prepared films A, B and C (150 °C, 18 h).

	CuSO₄ · 5H₂O	InCl₃	L-cysteine
Film A	0.06 M	0.06 M	0.15 M
Film B	0.02 M	0.02 M	0.05 M
Film C	0.01 M	0.01 M	0.03 M

8.3 Characterization

To characterize the films, several analytical methods were used. To determine the crystal structure, X-ray diffraction (XRD) patterns were acquired with a Bruker D8 Discovery diffractometer with CuK_α radiation ($\lambda = 1.54 \text{ \AA}$). The scanning rate was 0.05°/s. The 2θ range was 20 to 65°. The obtained patterns were compared to literature data. The full width at half maximum of the peaks was estimated by using a Gaussian function and the grain size was determined using the Scherrer equation. For general morphology investigations and the determination of the average chemical composition we used a Jeol JSM-6500F scanning electron microscope (SEM) operated at 5.0 kV and equipped with an energy dispersive X-ray (EDX) detector from Oxford Instruments (Inca Energy). Secondary electron (SE) imaging was done using the attached Jeol standard

detector. SEM cross-section and top view samples were prepared using conventional preparation techniques. The samples were carbon coated prior to the insertion into the SEM. For further characterization, transmission electron microscopy (TEM) investigations were done with a FEI Titan 80 – 300 (S)TEM microscope equipped with a Gatan Tridiem image filter and a EDAX EDX detector. The instrument was operated at 300 kV. The microscope is equipped with a high angle annular dark field (HAADF) detector from Fischione Instruments (Model 3000) for scanning TEM (STEM) imaging. Cross section TEM specimen preparation was accomplished as described by Strecker et al.^[17]. The electron diffraction data were evaluated using a calibrated camera constant obtained by using a Si standard. Electron energy loss spectroscopy (EELS) was performed in the diffraction mode using a dispersion of 0.3 eV per channel and acquisition times between 10 s and 50 s. This allows one to study the S-L₂₃ edge at around 165 eV and the Cu-L₂₃ edge at around 930 eV with a sufficient signal-to-noise ratio. UV/Vis absorption measurements of the films were done on a Perkin-Elmer 330 spectrometer.

8.4 Results

For the general investigation of the CuInS₂ films, SE imaging was used. Figure 8.1 shows an overview of the different morphologies and thicknesses of the three films synthesized with different concentrations of reactants but using the same heating times and cooling procedures. Film A, which exhibits a black color, was synthesized with the highest concentration of 0.06:0.06:0.15 M Cu:In:S; it is shown in Figure 8.1(a). At higher magnification (Figure 8.1(b)) it can be observed that the film possesses a mixed structure of small crystals with a rod like morphologies and plates that are growing out of the film. The SEM cross sectional view of film A (Figure 8.1(c)) shows a film thickness of about 350 nm. Plate-like shapes growing out of the film can be observed here as well. The CuInS₂ is completely covering the FTO substrate and no cracks or voids are observed at the film/substrate interface region.

A SEM image of film B, which displays a dark brown color, is presented in Figure 8.1(d). This film was synthesized with a three times lower concentration of reactants than film A. Figure 8.1(e) (taken at higher magnification) reveals that the film is built as a compact layer containing agglomerations of CuInS₂ nanoparticles. Hence the film is anticipated to

offer a high surface area. The cross section of the film (Figure 8.1(f)) indicates a thickness of 200 nm and indicates also a good wetting behavior of the film on the substrate. Figure 8.1(g) shows the top view of film C. The film has a bright brown color and was synthesized with half the concentration of reactants compared to film B. This film possesses a compact structure similar to film B, but seems to consist of larger agglomerates of nanoparticles (Figure 8.1(h)). The cross section of film C (Figure 8.1(i)) indicates a very thin film that appears to be more flat than films A and B. Furthermore, it can be observed that the FTO substrate is completely coated by the CuInS₂ film.

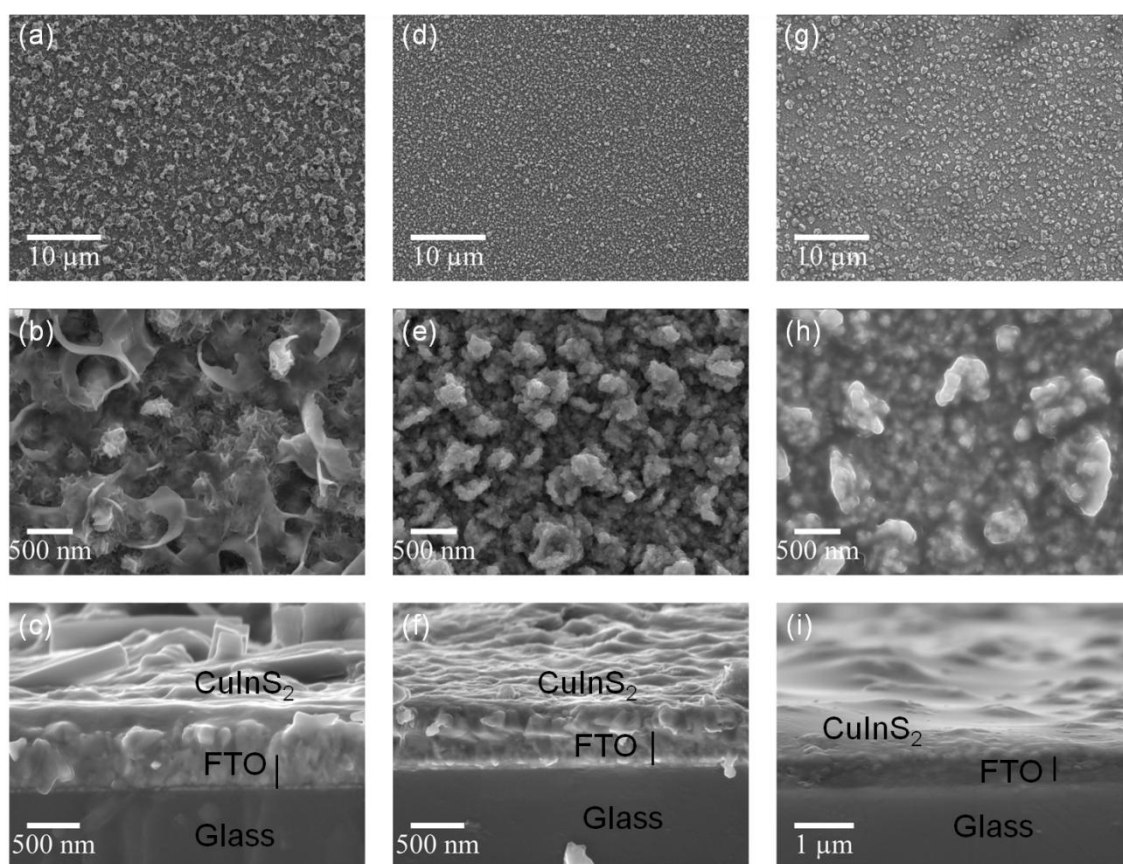


Figure 8.1: SE images of three CuInS₂ films synthesized with different concentrations of reactants on FTO substrates. (a) and (b) (higher magnification) show top views while (c) shows the cross section of film A. (d) and (e) (higher magnification) display top views and (f) shows the cross section of film B. (g) and (h) (higher magnification) show top views and (i) shows the cross section of film C.

The average chemical composition of the films was measured using EDX in SEM. The EDX spectra of film A, B and C measured in the SEM indicate signals of Cu, In, and S. The detected Sn and O stem from the FTO substrate and Si and O from the glass. No additional peaks indicating impurities were observed. The quantification of several

spectra of film A leads to an average composition of 11 ± 2 at% Cu, 12 ± 2 at% In, 28 ± 2 at% S and 48 ± 2 at% Sn. The quantification of spectra from film B leads to 5 ± 2 at% Cu, 6 ± 2 at% In, 11 ± 2 at% S and 78 ± 2 at% Sn, and for film C the results were 4 ± 2 at% Cu, 4 ± 2 at% In, 10 ± 2 at% S and 82 ± 2 at% Sn. Thus, in all cases an approximate stoichiometric composition of 1:1:2 was obtained. The appearance of Sn, O and In signals and the significant error in the quantification are due to the small thickness of the films, especially for film C. Therefore, additionally EDX measurements in the TEM in STEM mode were done as described below.

The investigation of the global crystal structure of the films was done via XRD. Figure 8.2(a) shows the XRD pattern of film A with the characteristic reflections of CuInS₂ in the roquesite structure. Roquesite is a tetragonal crystal type with lattice parameters $a = 0.552$ nm and $c = 1.112$ nm. The obtained reflections are (112), (204) and (312), all additional reflections originate from the FTO substrate. No further reflections indicating impurities or byproducts like copper and indium sulfides or their oxides can be observed. The XRD pattern of film B (Figure 8.2(b)) also reveals the characteristic reflections for CuInS₂ for the roquesite structure. Again, no side products such as other sulfides or oxides were detected. The CuInS₂ peaks are rather broad, indicating that small domain or crystal sizes occur in the film structures. These were analyzed by applying the Scherrer equation using a K shape factor of 0.9. The calculations resulted in an average crystallite size of 7 nm for film A and 10 nm for film B. Due to small thickness of film C the XRD measurements were not successful. However, the crystal structure was investigated by electron diffraction experiments and the results are given below.

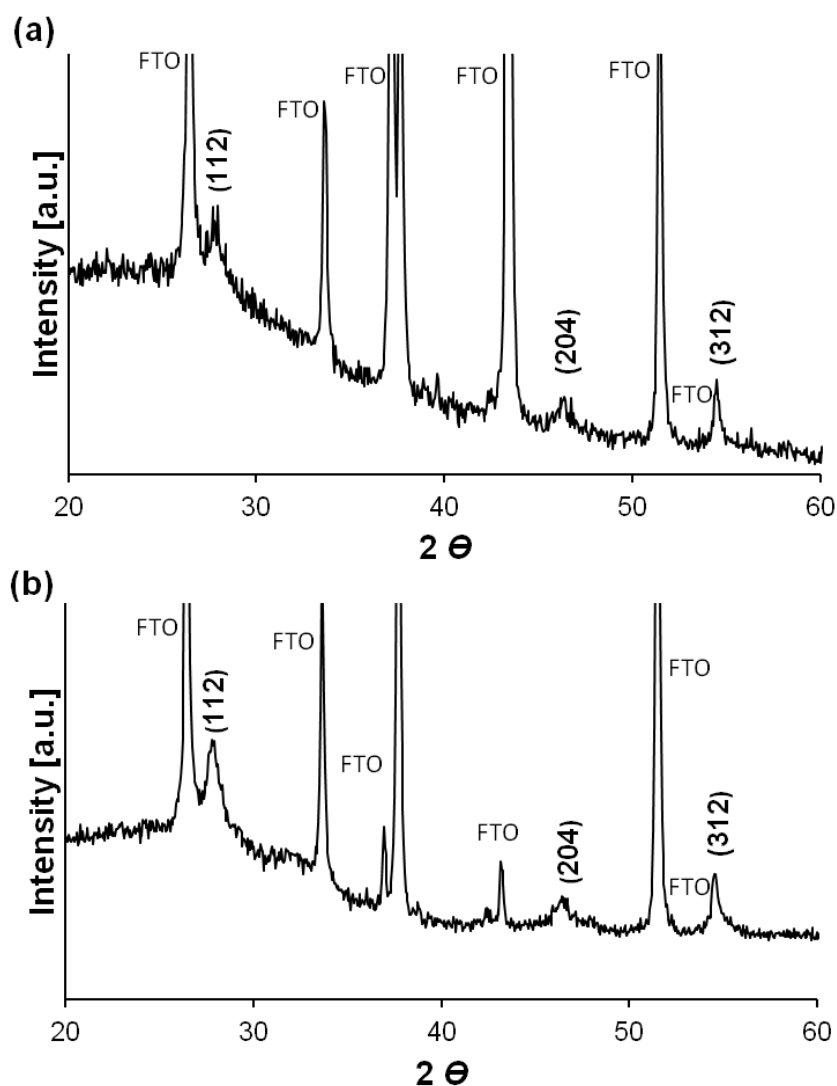


Figure 8.2: XRD pattern of film A (a) and B (b) reveals the tetragonal Roquesite crystal structure. Additional peaks result from the FTO substrate. A zoom-in is shown for better visualisation.

The absorption behavior of the films was studied using UV/Vis spectroscopy. The spectra of film A (black), film B (red dotted) and film C (blue dotted) are given in Figure 8.3. In all cases, the spectra display absorption over the whole visible spectrum. Importantly film B, which shows a dark brown color and a thickness of only up to 250 nm, shows a high absorption. Finally, film C with a bright brown color and a thickness of less than 50-100 nm still possesses significant absorption.

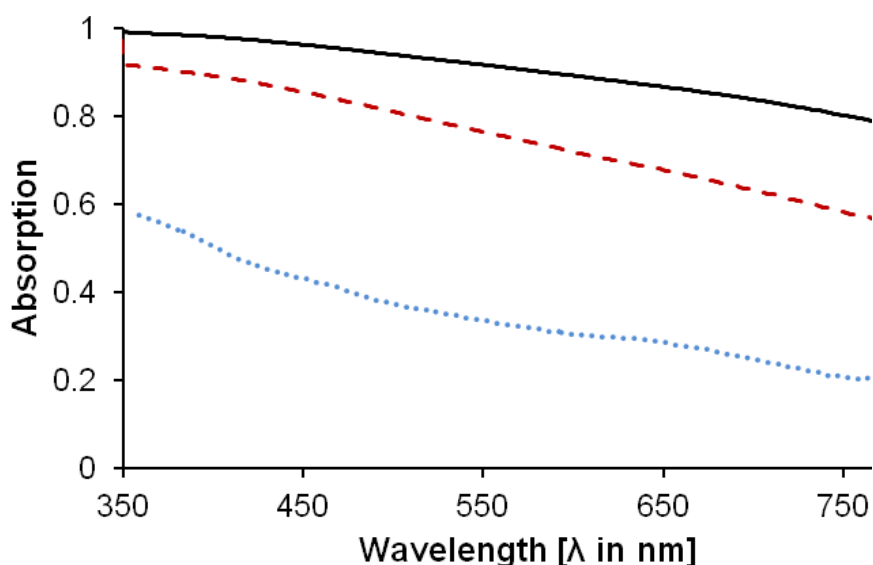


Figure 8.3: UV /Vis spectra of film A (black), B (red dotted) and C (blue dotted).

The investigations on the different films described above indicate that film B and C are better suitable for thin absorber solar cell applications due to their small thickness and high surface area. Hence, TEM investigations were only done on film B and C, and not for the thickest film A. The TEM studies of the thinner films B and C were performed to determine the crystal structure and the chemical composition on the nanometer scale. The bright field image in Figure 8.4(a) shows the CuInS₂ structure of film B. The film adheres well to the rough FTO substrate. No delamination or cracks could be observed. The film is built of a mixed structure indicating a compact polycrystalline part (made out of ≈ 10 nm sized nanoparticles) and plates that seem to grow out at the top of the layer. The film thickness determined by TEM for the compact layer is about 150 - 250 nm, which is in accordance with the SEM measurements. Additionally, the film contains thicker parts of up to 600 nm consisting of agglomerations of nanoparticles (size < 10 nm), which can also be observed in the SEM image (Figure 8.1(e)) and are possibly formed in the reaction solution and accumulate to the surface of the film growing on the FTO substrate. The ADF-STEM image in Figure 8.4(b) taken at higher magnification shows a thinner area of the film. Here the film is thinned out from the ion milling during the cross-section sample preparation. This image reveals again the mixed structure consisting of a compact polycrystalline part and plates on top of the layer. Additionally, it can be observed that these plates with a thickness of 10-50 nm are built of several 1-2 nm thin layers. The diffraction pattern in Figure 8.4(c) was taken from a circular area of

a different part of the layer with a diameter of 150 nm. The diffraction pattern indicates a polycrystalline layer and possesses spots that match well with the d values of roquesite for (112), (204) and (312). All additional reflections can be attributed to the FTO substrate. However, Cu(I)-sulfides and the FTO substrate show similar d-values and thus their presence cannot be excluded. The phase diagram of the (Cu-In-S)-system resulting from a binary system of Cu₂S-In₂S₃ indicates the formation of predominant CuInS₂ in the roquesite structure with around 50 to 52% mole percent In₂S₃ for the given conditions.^[18] As we used Cu and In in equimolar composition, we assume that the system is in that region of the phase diagram. However, the formation of mixed phases like CuInS₂ with Cu₂S and In₂S₃ cannot be excluded as will be discussed later.

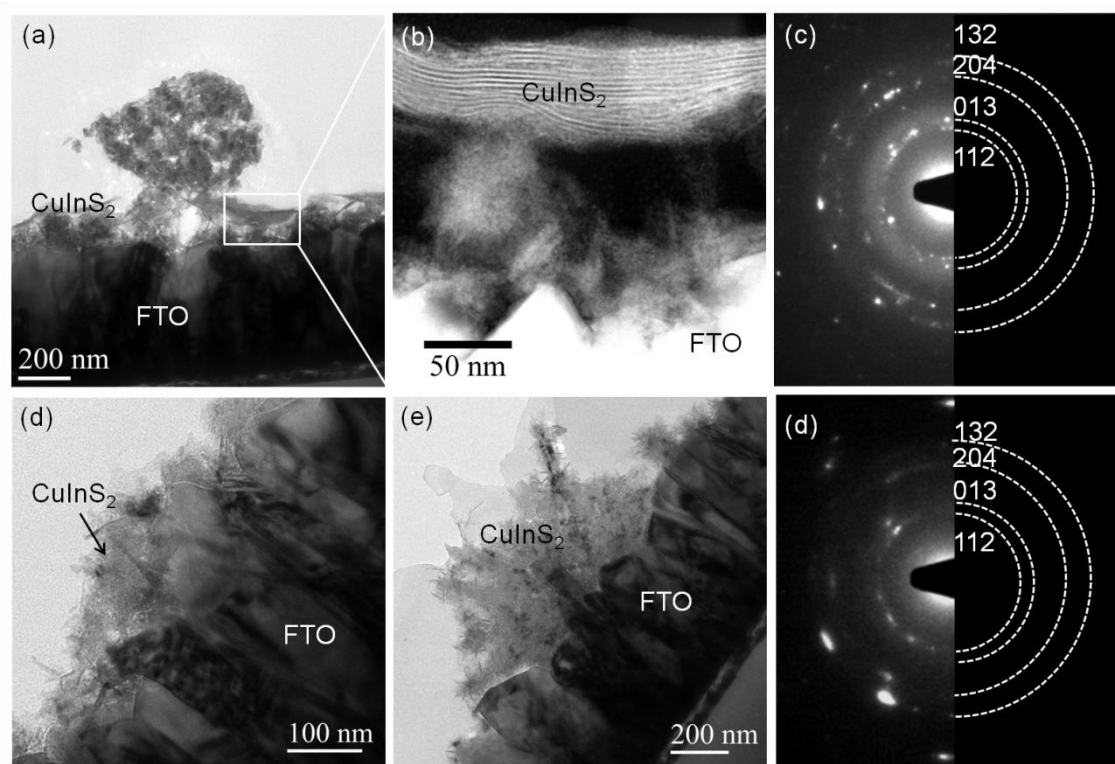


Figure 8.4:(a) BF image and (b) ADF-STEM image of film B show a mixed structure (polycrystalline layer and plates). Plates are 10 – 50 nm thick, consisting of 1 – 2 nm layers. (c) Diffraction pattern shows reflections of CuInS₂ in roquesite structure. BF images (d, e) of film C show 50 – 100 nm thick film and thicker areas (up to 500 nm). (f) Diffraction pattern features spots of CuInS₂ in roquesite structure. Note the different scale bars.

The EDX analysis of the film B was done in the STEM mode with a spot size of about 1 nm. 30 EDX spectra were taken at different positions of the film. The quantification of the EDX spectra of the compact layer resulted in about 27 ± 3 at% Cu, 23 ± 3 at% In and 50 ± 3 at% S and gives, considering the error margin, an average chemical composition of Cu:In:S = 1:1:2 and therefore proof the results of the EDX measurements in the SEM.

The TEM investigation of film C is summarized in Figure 8.4(d-f). The BF image of the TEM cross section in Figure 8.4(d) shows a compact part of the film with a thickness of about 50–100 nm. The diffraction pattern (Figure 8.4(f)) taken from a circular area with a diameter of 150 nm indicates that this area is polycrystalline. It possesses spots that correspond well with the d values of roquesite for (112), (204), (312) and (316). The bright field image in Figure 8.4(e) reveals that the film has, besides the 50 – 100 nm thick compact layer, additional thicker parts (up to 500 nm). This thicker area results from agglomerations of particles that can be observed in the SEM image shown in Figure 8.1(h). In this sample the film is built of nanocrystals (< 10 nm) and small rods (\approx 10 nm wide, 100 nm long) that form tree-like structures. The EDX analysis of film C was performed in STEM mode again. The quantification of the spectra measured at different areas of the thinner parts and the middle of the thicker parts of the film resulted in 27 ± 2 at% Cu, 23 ± 2 at% In and 50 ± 2 at% S and gives, similar as in film B, an average chemical composition of Cu:In:S = 1:1:2. These results are comparable to the EDX measurements of this film taken in the SEM.

To investigate the growth mechanism of the films the reaction of L-cysteine with CuSO₄ was analyzed. When L-cysteine and CuSO₄ are dissolved in ethanol a grey solid is formed. The solid was washed with double distilled water to remove remaining L-cysteine. XRD shows a broad feature at around $2\theta = 23^\circ$ indicating the presences of an amorphous phase and sharp reflections. These reflections that match well with a Cu-cysteine complex in a monoclinic crystal structure with the lattice parameters $a = 1.41$ nm, $b = 0.45$ nm and $c = 0.98$ nm as described by Dokken et al.^[19] Additionally, weak reflections of Cu₂S can be found in the XRD spectra (Figure 8.5).

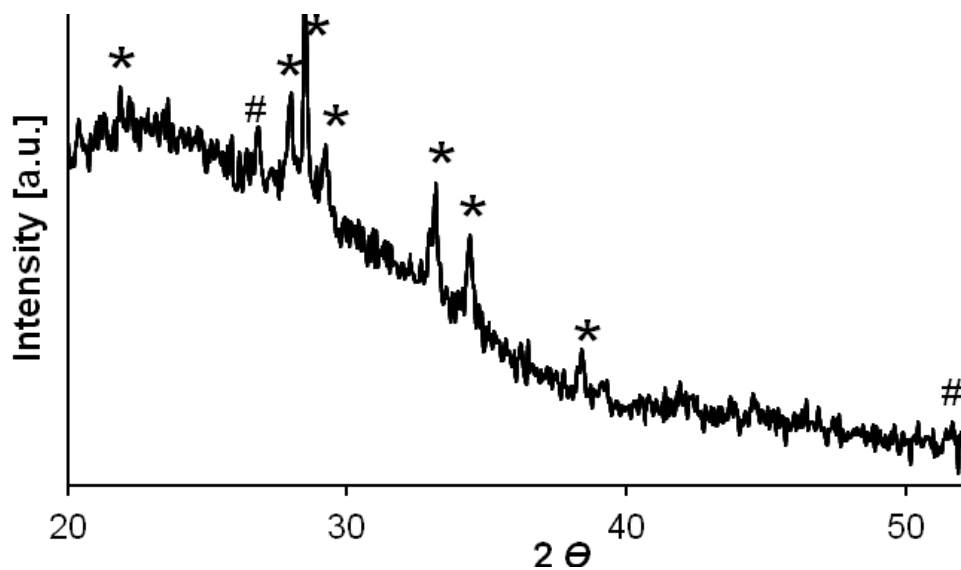


Figure 8.5: XRD pattern of the grey reaction product of L-cysteine and CuSO₄. Reflections assigned with * match with a Cu-cys complex published by Dokken et al.^[19], and reflections assigned with # can be attributed to Cu_xS phases.

TEM analysis of the grey solid shows 3 - 5 nm sized crystals embedded in an amorphous material. The high resolution TEM and BF image is given in Figure 8.6(a) and (b). Further EELS measurements and electron diffraction experiments in the TEM confirmed the presence of Cu₂S. The S-L₂₃ and Cu-L₂₃ edges in the spectra show similarities to the one of Cu_xS when compared with data from the literature (Figure 8.7).^[20] The obtained polycrystalline electron diffraction patterns reveal reflections with d values of 3.31 Å and 1.95 Å and can be assigned to (002) and (110) of Cu₂S in the hexagonal structure, to the (120) and (019) of Cu_{1.81}S in the tetragonal structure or to the (341) and (573) of Cu₂S in the orthorhombic structure (diffraction pattern shown in Figure 8.6(c), the according planes are listed in Table 8.2). The same reflections were found in the XRD pattern (Figure 8.5). No evidence of CuS or Cu_xO was found.

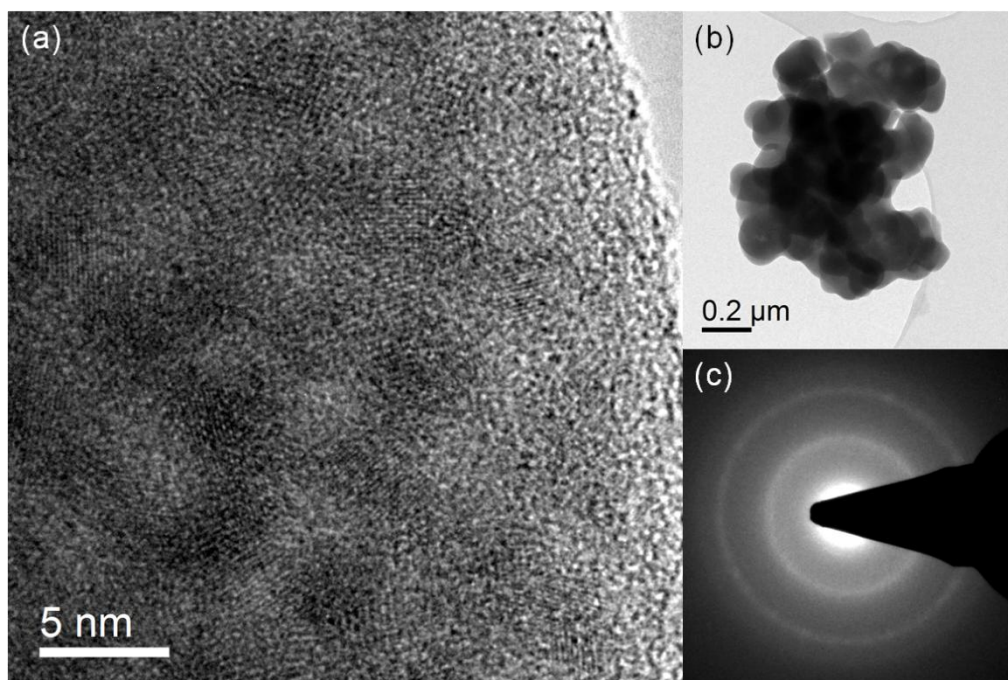


Figure 8.6: (a) High resolution TEM image of the reaction product of L-cysteine and CuSO₄ in ethanol shows 2 - 5 nm crystals embedded in amorphous material. (b) BF image shows the investigated agglomerated particles. (c) Diffraction pattern of the agglomerate reveals reflections that match with Cu_xS phases.

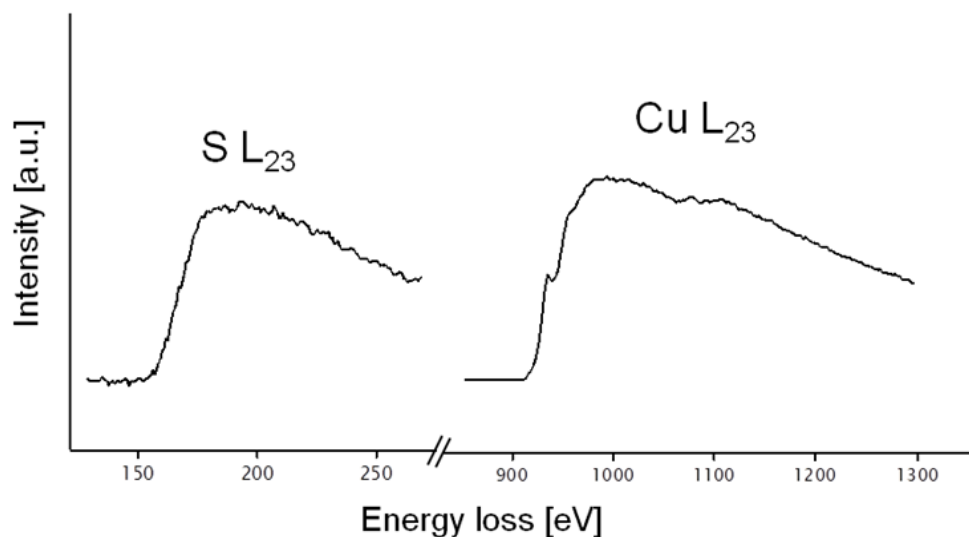


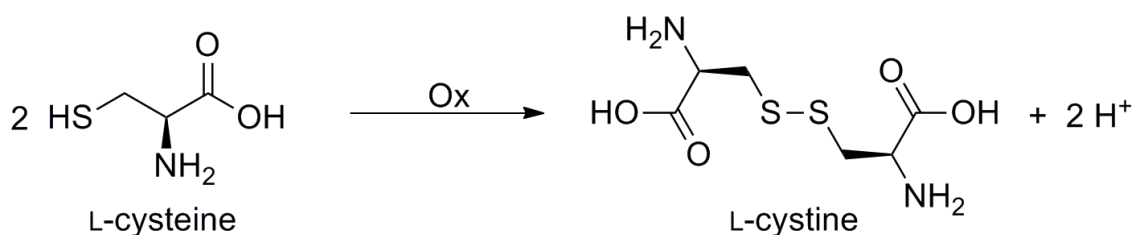
Figure 8.7: EELS spectra taken from the product of L-cysteine and CuSO₄. The obtained edges indicate the presence of Cu_xS when compared with literature.^[20]

Table 8.2: Observed d and 2θ values of the electron diffraction pattern of the grey solid.

observed		Cu ₂ S ^[21] hexagonal	Cu _{1.81} S ^[22] tetragonal	Cu ₂ S ^[23] orthorhombic
d value / Å	2θ			
3.31	26.86	(002)	(120)	(341)
1.95	46.51	(110)	(019)	(573)

8.5 Discussion

Based on our findings the growth mechanism of the films can be described as follows: A redox reaction takes place when L-cysteine (the sulfur source) reacts with Cu(II) ions from the aqueous CuSO₄ solution to Cu(I) while the thiols are oxidized to disulfides (L-cysteine, see Figure 8.8). Cu(I) interacts with the excess thiols. In addition, due to the favorable soft-acid base interaction a Cu(I)-cystine complex can be formed. This mechanism is already known in literature.^[24, 25] In our reaction solution Cu₂S was found. This means that the reduction potential of L-cysteine is sufficient to reduce Cu(II) to Cu(I), while it is itself oxidized to L-cystine (Figure 8.8). Free In³⁺ can react with S²⁻, which stems from the decomposition of L-cysteine and L-cystine to form (InS₂)⁻ dissolved in the solution. The latter mechanism has been observed in the literature in similar systems.^[11, 16, 26] The (InS₂)⁻ can react with Cu⁺ in solution to form the ultimate product CuInS₂.

**Figure 8.8: Oxidation from L-cysteine to L-cystine.**

As already mentioned above, the (Cu-In-S)-system can be described with the help of the quasi-binary Cu₂S-In₂S₃ phase diagram. This phase diagram indicates the formation of mainly CuInS₂ in the roquesite structure at around 50 to 52 % mole percent In₂S₃^[18]. In our reaction we use Cu:In at equimolar composition, so the formation of CuInS₂ in the

roquesite structure is plausible and can be supported with the EDX measurement in the SEM and TEM. Although the formation of mixed phases cannot be excluded, most if not all of the Cu(I) created in the reaction solution has been transferred to CuInS₂. The different film morphologies can be explained with the use of different reactant concentrations. Film A synthesized with the highest concentration of Cu:In:S of 0.6:0.6:1.5 consists of smaller crystals up to 7 nm (determined by the Scherrer equation). During the reaction procedure the film starts to grow with CuInS₂ nuclei to form a polycrystalline compact film with rods and flakes on the top. In film B with a lower reactant concentration of Cu:In:S: 0.2:0.2:0.5, the formed CuInS₂ nuclei lead to bigger crystals of up to 10 nm which form a compact layer and larger agglomerations of these crystals. It is worth to mention that we only use L-cysteine as reducing species while in literature studies additional reducing species are added.^[11, 16]

As mentioned above, Wen et al.^[16] synthesized CuInS₂ powder with L-cysteine as sulfur source. They obtained microspheres made up of nanosheets. The thickness of the nanosheets was found to vary from 50 to 100 nm. The characterization of the powder was done with XRD, SEM, X-ray photoelectron spectroscopy (XPS) and TEM. Despite using a different Cu source and solvent, a powder with similarly composed nanospheres was obtained during our reaction as side product in the autoclave.

Liu et al.^[11] synthesized CuInS₂ nanocrystals via an L-cystine-assisted growth using a solvothermal process. In contrast to our reaction route they used CuCl₂ · 2H₂O. They also investigated the synthesis using different solvents and reaction times. They obtained a product of agglomerates of irregular microspheres and nanocrystals with ethanol as solvent. The SEM investigation of their product offers a structure of nanocrystals similar to the SEM top view of our film B (Figure 8.1(e)). XRD data revealed the tetragonal roquesite structure, which was confirmed using electron diffraction patterns obtained in the TEM in accordance to our studies.

Additional sulfidic nanostructures obtained with L-cysteine-assisted synthesis are reported in the literature. However, the obtained structures are different in shape and size compared to each other and to our results. For example, Zhao et al.^[15] reported about the fabrication of In₂S₃ hollow spheres possessing a porous surface structure and consisting of nanoflakes using L-cysteine as complexing agent and sulfur source. Min et al.^[27] synthesized iron sulfide via a solvothermal method using L-cysteine. They

obtained, depending on the experimental conditions such as reactant ratio, volume ratio of solvents and reaction temperature different morphologies of Fe_{0.958}S like nanofibers and micro-flowers composed of nanoflakes. Zuo et al.^[13] reported about the L-cysteine-assisted synthesis of PbS nanocube-based pagoda-like hierarchical architectures using a solvothermal synthesis method. Xiang et al.^[14] synthesized Ag₂S nanospheres using L-cysteine as sulfur source and Chen et. al.^[28] reported about the L-cysteine-assisted growth of core-satellite ZnS-Au nanoassemblies. Thus, depending on the synthetic details sulfur-based nanostructures can be successfully prepared using L-cysteine as a sulfur source.

8.6 Conclusion

In this study L-cysteine was used for the first time to prepare CuInS₂ thin films in a solvothermal synthesis route. It is shown that L-cysteine acts as a reducing species and is sufficient to reduce Cu²⁺ from the used CuSO₄ in aqueous solution to Cu⁺ to induce the formation of CuInS₂. All three resulting CuInS₂ films, synthesized with different concentrations of reactants, show different morphologies and differ in the film thickness and structure. Thus depending on the concentration of the reagents the film growth can be strongly modified (compare Figure 8.1(a)-(i)). The TEM investigation reveals different film thicknesses as well. A mixed structure of a polycrystalline compact layer and plates in the case of film B and rods in the case of film C was observed. For all films, EDX measurements in the SEM resulted in an average stoichiometric composition of Cu:In:S = 1:1:2. This result was confirmed with EDX measurements in STEM mode in the TEM. This leads us to the conclusion that the films grow with a stoichiometric composition. The XRD investigation of the films shows the characteristic reflections of CuInS₂ in the roquesite structure. No additional impurities were found. These results were confirmed by electron diffraction studies in the TEM. Moreover, all three films A, B and C show significant absorption over the whole visible spectrum. Therefore the films are viewed as possible candidates for thin absorber layers in solar cell designs.

8.7 Chapter references

- [1] B. Tell, J. L. Shay, H. M. Kasper, *Phys. Rev. B* **1971**, *4*, 2463.
- [2] F. M. Courtel, R. W. Paynter, B. Marsan, M. Morin, *Chem. Mater.* **2009**, *21*, 3752-3762.
- [3] J. A. Hollingsworth, K. K. Banger, M. H. C. Jin, J. D. Harris, J. E. Cowen, E. W. Bohannon, J. A. Switzer, W. Buhro, A. F. Hepp, *Thin Solid Films* **2003**, *431*, 63-67.
- [4] M. C. Zouaghi, T. Ben Nasrallah, S. Marsillac, J. C. Bernede, S. Belgacem, *Thin Solid Films* **2001**, *382*, 39-46.
- [5] S. i. Kuranouchi, T. Nakazawa, *Sol. Energy Mater. Sol. Cells* **1998**, *50*, 31-36.
- [6] H. M. Pathan, C. D. Lokhande, *Appl. Surf. Sci.* **2004**, *239*, 11-18.
- [7] P. Guha, D. Das, A. B. Maity, D. Ganguli, S. Chaudhuri, *Sol. Energy Mater. Sol. Cells* **2003**, *80*, 115-130.
- [8] Y. Shi, Z. Jin, C. Li, H. An, J. Qiu, *Appl. Surf. Sci.* **2006**, *252*, 3737-3743.
- [9] S. Peng, F. Cheng, J. Liang, Z. Tao, J. Chen, *J. Alloys Compd.* **2009**, *481*, 786-791.
- [10] A. S. Wochnik, C. Heinzl, F. Auras, T. Bein, C. Scheu, *J. Mater. Sci.* **2012**, *47*, 1669-1676.
- [11] H.-T. Liu, J.-S. Zhong, B.-F. Liu, X.-J. Liang, X.-Y. Yang, H.-D. Jin, F. Yang, W.-D. Xiang, *Chin. Phys. Lett.* **2011**, *28*.
- [12] Q. Lu, F. Gao, S. Komarneni, *J. Am. Chem. Soc.* **2003**, *126*, 54-55.
- [13] F. Zuo, S. Yan, B. Zhang, Y. Zhao, Y. Xie, *J. Phys. Chem. C* **2008**, *112*, 2831-2835.
- [14] J. Xiang, H. Cao, Q. Wu, S. Zhang, X. Zhang, A. A. R. Watt, *J. Phys. Chem. C* **2008**, *112*, 3580-3584.
- [15] P. Zhao, T. Huang, K. Huang, *The Journal of Physical Chemistry C* **2007**, *111*, 12890-12897.
- [16] C. Wen, X. Weidong, W. Juanjuan, W. Xiaoming, Z. Jiasong, L. Lijun, *Mater. Lett.* **2009**, *63*, 2495-2498.
- [17] A. Strecker, U. Salzberger, J. Mayer, *Prakt. Metallogr.* **1993**, *30*, 482-495.
- [18] O. V. Parasyuk, S. V. Voronyuk, L. D. Gulay, G. Y. Davidyuk, V. O. Halka, *J. Alloys Compd.* **2003**, *348*, 57-64.
- [19] K. M. Dokken, J. G. Parsons, J. McClure, J. L. Gardea-Torresdey, *Inorg. Chim. Acta* **2009**, *362*, 395-401.
- [20] F. Hofer, P. Golob, *Ultramicroscopy* **1987**, *21*, 379-383.
- [21] N. V. Belov, Butuzov, V.P., *Doklady Akademii Nauk SSSR* **1946**, *54*, 717.
- [22] I. S. Chaus, N. M. Kompanichenko, V. G. Andreichenko, Y. I. Gornikov, I. A. Sheka, *Ukr. Khim. Zh. (Russ. Ed.)* **1987**, *53*, 566-568.
- [23] G. A. Harcourt, *Am. Mineral.* **1942**, *27*, 63-113.
- [24] M. Ahmed, M. S. Iqbal, N. Tahir, A. Islam, *World Appl. Sci. J.* **2011**, *14*, 210-214.
- [25] D. Cavallini, M. C. De, S. Dupre, G. Rotilio, *Arch. Biochem. Biophys.* **1969**, *130*, 354-361.
- [26] S. Gorai, S. Bhattacharya, E. Liarokapis, D. Lampakis, S. Chaudhuri, *Mater. Lett.* **2005**, *59*, 3535-3538.
- [27] Y. L. Min, Y. C. Chen, Y. G. Zhao, *Solid State Sci.* **2009**, *11*, 451-455.
- [28] W.-T. Chen, Y.-J. Hsu, *Langmuir* **2009**, *26*, 5918-5925.

9 Optimization of sol-gel synthesized TiO₂ blocking layers

9.1 Introduction

In recent years titanium dioxide thin films have attracted more and more research interest due to their chemical, electrical and optical properties allowing various applications in different fields such as microelectric devices and solar cells.^[1] Especially in solar cells such as dye sensitized or extremely thin absorber solar cells, TiO₂ thin films are applied as blocking layers to prevent short circuiting.^[2-4] Numerous studies have shown that the use of a blocking layer has a positive effect on the solar cell performance.^[5, 6] Various techniques can be used to grow TiO₂ blocking layers such as electrodeposition,^[3] magnetron-sputtering,^[7] chemical vapor deposition^[8], chemical spray pyrolysis,^[9, 10] and the sol-gel method^[1, 11]. Many investigations were done on differently prepared films regarding their structure, optical and electrical properties and thus the influence on solar cell efficiency.^[10, 12, 13] Also, experiments were conducted concerning the effect of layer thickness and calcination temperatures on the blocking layer.^[1, 14] The sol-gel method has some benefits compared to other techniques like controllability and reproducibility and is convenient for the preparation of nano-structured thin films.^[15, 16] Different deposition methods on substrates e.g. dip and spin coating can be used.^[11, 17] The synthesis of TiO₂ blocking layers prepared via a sol-gel method is reported in literature with different precursors, solvents or catalysts. The effect of different parameters like the pH value of the sol-gel system, catalyst concentration and calcinations on the particle size, crystal phase or structure was investigated.^[1, 18] In this work, we synthesized TiO₂ blocking layers in Anatase modification via a sol-gel method, using a calcination temperature of 450 °C. The deposition on FTO coated glass was done by spin-coating. We show the influence of the dwell time during calcination on the particle size and electric conductivity of the films. The particle size within the obtained Anatase layers was characterized with HRTEM. In addition, the film thicknesses after spin-coating with two different speeds were investigated by TEM. The electrical conductivity was investigated via I-U measurements.

9.2 Experimental

All used chemicals were of analytical grade and used without further purification. Fluorine-doped tin oxide conductive glass (Pilkington) with a dimension of 20 x 15 x 2 mm was taken as substrate for the deposition of the TiO₂ films. The FTO was ultrasonicated in a solution of one part extrane and five parts double-distilled water for 15 min. A second ultrasonication was done with ethanol for another 15 min. Afterwards, the substrates were dried with compressed air and treated in an O₂-plasma cleaner for 10 min. For the synthesis of the TiO₂ layers a modified version of the synthesis route of B. Mandlmeier et al.^[19] was used. A highly diluted tetrahydrofuran sol-gel solution was prepared by giving 0.186 ml concentrated hydrochloric acid to 0.275 ml tetraorthoethyltitanate while stirring and diluting the incurred sol-gel solution with 3.5 ml tetrahydrofuran. For the deposition of the TiO₂ layers on the cleaned FTO substrates a spin coater was used. 0.130 ml of the prepared sol-gel solution was given on the FTO substrates. The spin coating parameters were 3000 rpm for 1.5 min leading to thinner films or 1500 rpm for 1.5 min leading to thicker films. After spin coating, the layers were heated to 450 °C within 11.0 h, left at this temperature for 0.5 h, 1.0 h, 1.5 h, 2.0 h and 5.0 h and then cooled to room temperature within 11.0 h. The different calcinations times are shown in Figure 9.1.

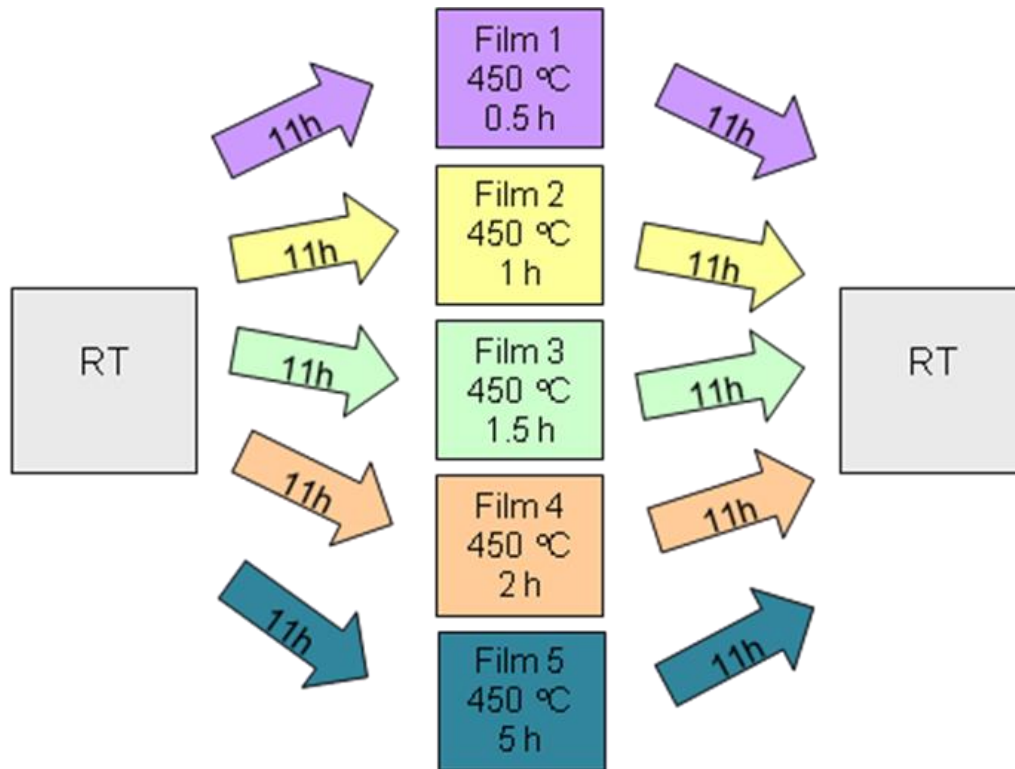


Figure 9.1: Schematic of the different oven programs. The dwell time for synthesis 1 is 0.5 h (purple), synthesis 2 is 1 h (yellow), synthesis 3 is 1.5 h (green) synthesis 4 is 2 h (red), and synthesis 5 is 5 h.

The obtained TiO₂ films showed a homogenous, transparent surface. All films synthesized with different dwell times were prepared with spin coating speeds of 3000 rpm and 1500 rpm.

9.3 Characterization

To characterize the films, different analytical techniques were applied. For the investigation of film thicknesses and crystal grain sizes in the films, a FEI Titan 80–300 (S)TEM, equipped with a Gatan Tridiem image filter and an EDAX EDX detector for analytical measurements, was used. Cross-sectional TEM specimens were prepared as described by Strecker et al.^[20] Electron diffraction experiments were realized to investigate the crystal phase of the film. The data was evaluated using a calibrated camera constant obtained using a Si standard. To investigate the conductivity of the films, I-U curves were measured with a source-meter 2636a from Keithley. The resulting current was measured between two points within an interval of –0.3 to 0.3 V.

9.4 Results and discussion

To investigate the influence of the different dwell times on the structure of the TiO₂ films prepared at 450 °C and to determine the thickness of the films with different spin coating parameters, TEM measurements were done. Figure 9.2 shows exemplary bright field images of two films. The bright field images in Figure 9.2 displays film 4 (a), which was left at 450 °C for 2 h spin coated with 3000 rpm and film 5 (b) left at 450 °C for 5 h and spin coated with 1500 rpm. It can be seen that the films are polycrystalline. Additionally, the films possess a good adhesion to the rough surface of the FTO substrate and have a flat surface. Furthermore, it can be observed that the thinner film 4 only fills the gaps of the rough FTO surface and exhibits a minimum film thickness of about 14 – 20 nm and a maximum thickness of about 100 nm while film 5, which was spin coated with 1500 rpm shows a minimum film thickness of about 70 -75 nm and a maximum film thickness of about 180 nm This can be attributed to higher spin coating speeds resulting in higher centripetal forces, removing excess material.

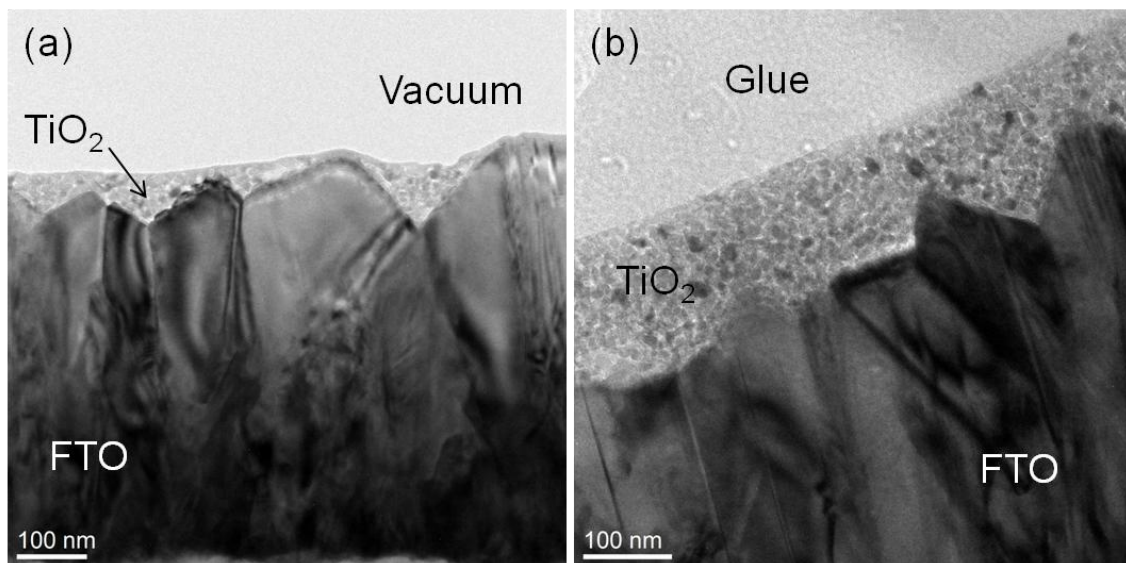


Figure 9.2: (a) shows film 4 which was spin coated with higher speed. The film has a thickness of 14-20 nm at the thinner areas. In (b) film 5 is given which was spin coated with half speed. The film thickness increases to 70-75 nm at the thinner areas.

To investigate the influence of the different dwell times on the grain size in the films HRTEM images were realized. Examples are shown in Figure 9.3. In Figure 9.3(a) film 1, (b) film 2, (c) film 3, (d) film 4 and (e) film 5 is depicted.

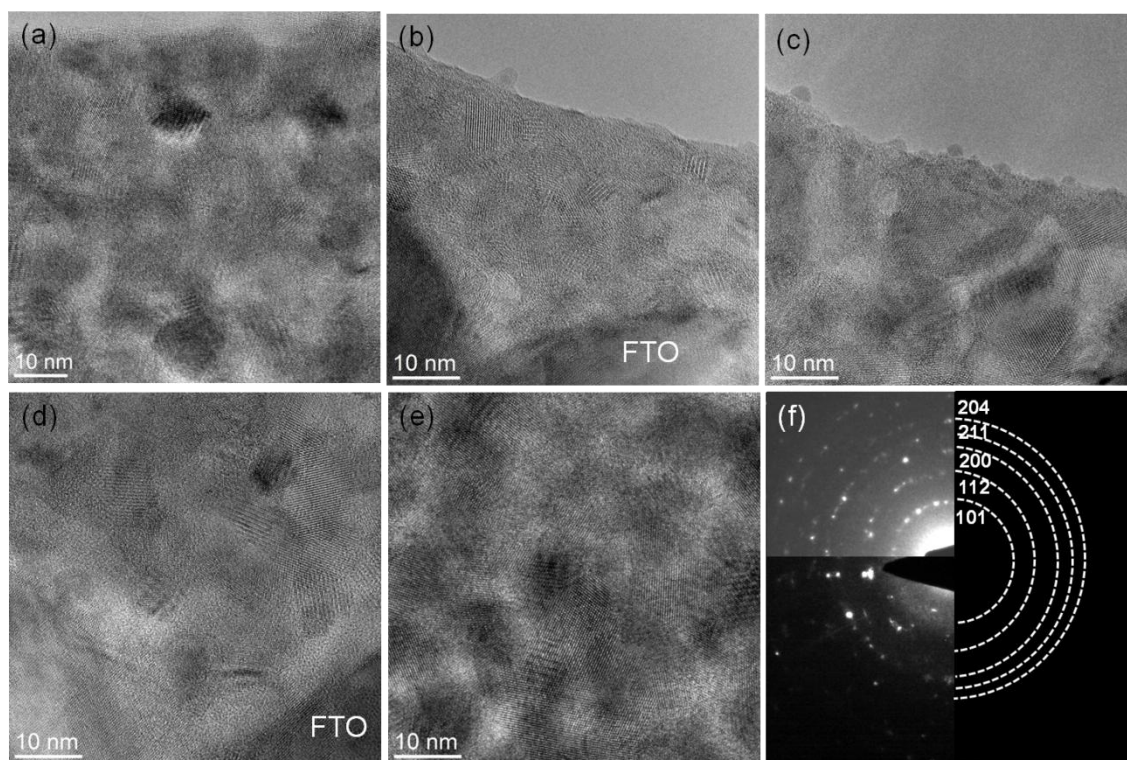


Figure 9.3: High resolution TEM images of (a) film 1, (b) film 2, (c) film 3, (d) film 4 and (e) film 5. (f) shows the diffraction pattern from film 5 (upper part) and film 3 (lower part). Reflections of TiO₂ in Anatase modification belonging to (101), (112), (200), (211) and (204) lattice planes were found.

All films are polycrystalline, with the crystal grains embedded in an amorphous matrix. An orientation relationship with the FTO substrate could not be found. The analysis of the average grain size of the different films is summarized in Table 9.1.

Table 9.1: Average grain size observed in film prepared at different dwell times during calcination.

Film	1	2	3	4	5
Calcination times [h]	0.5	1.0	1.5	2.0	5.0
Average particle size [nm]	8.9 ± 0.5	9.8 ± 0.5	11.7 ± 0.5	12.6 ± 0.5	13.1 ± 0.5

These results indicate that longer calcination times lead to increased grain sizes within the films. In Figure 9.4 the grain sizes are plotted against the calcination temperatures. It can be seen that the grain size in the first four films follows a linear behavior, indicating continuous growth. Film 5 deviates from this as the grain size increase is significantly smaller than expected.

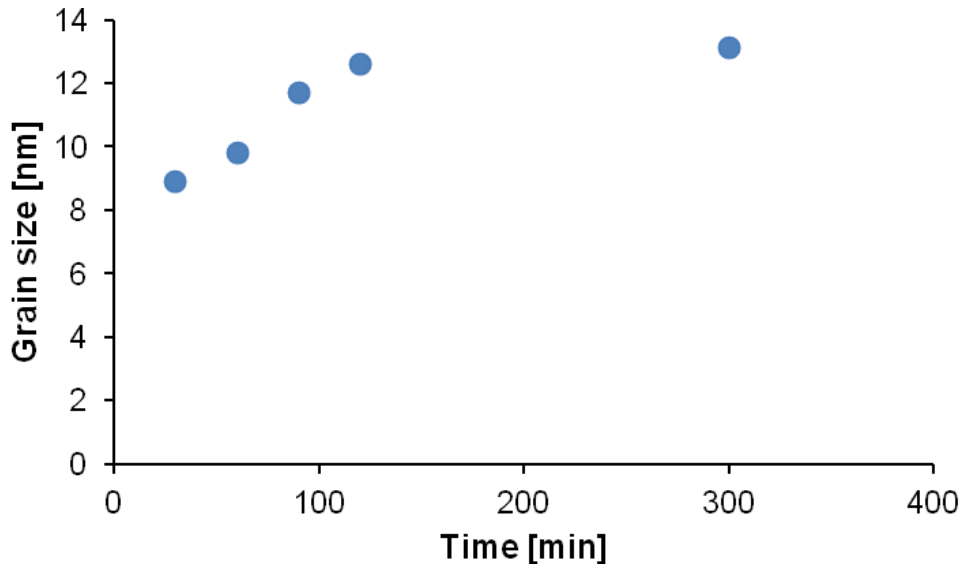


Figure 9.4: Addition of the grain size against the calcination temperatures.

Further investigations of the HRTEM images reveals that the film 1 - 4 show amorphous areas between the grains which cannot be observed in film 5. This indicates that the crystal grains grow into the amorphous area explaining the decrease in the growth speed from a certain growth speed onward.

The diffraction pattern in Figure 9.2(f) was taken at film 5 (upper part) and film 3 (lower part) from an area of about 150 nm². The pattern proves that the film is polycrystalline, without a preferred orientation and shows the (101), (112), (200), (211) and (204) reflections of TiO₂ in the Anatase modification. Beside reflections of the FTO substrate no additional reflections related to impurities were found. The analysis of the diffraction pattern taken from the films 1 - 5 gave the same results. However, a diffuse scattering in the diffraction pattern of film 3 is observed which is due to the amorphous matrix.

To investigate the influence of the dwell time during the calcination and therefore the grain size on the conductivity, I-U curves of films prepared with a spin coating speed of 1500 rpm were measured with a source meter. Several films from each calcination times were measured. Example I-U curves are displayed in Figure 9.5.

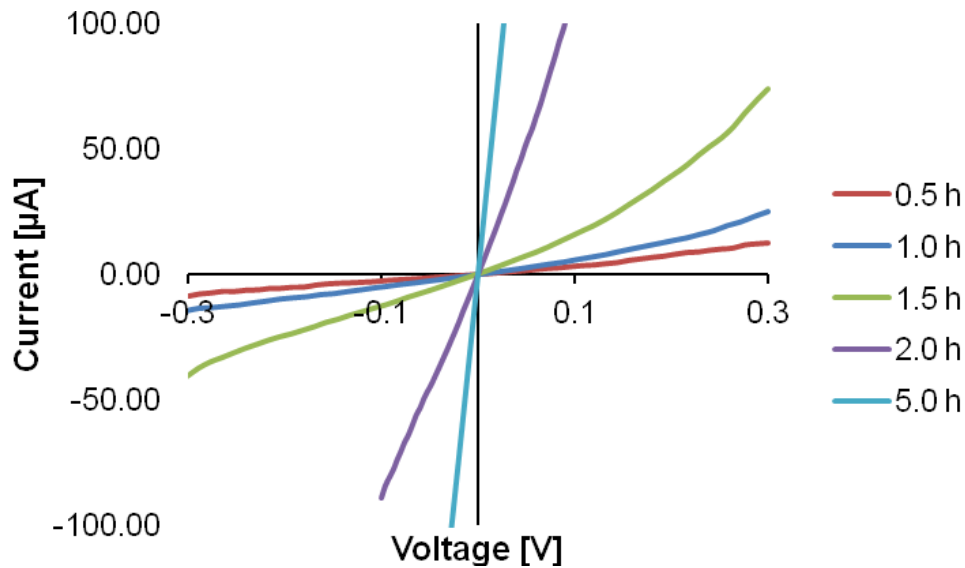


Figure 9.5: I-U curves from the films 1 - 5. The resistance decreases with longer calcination times.

In Figure 9.5 results with the highest values for the current are shown. From these curves, the resistance can be calculated by:

$$R = \frac{U}{I}$$

Here R is the resistance, I the current and U the voltage. The resistance of all five films were calculated in this way and are summarized in Table 9.2

Table 9.2: Resistances of the measured films 1 - 5.

Film	1	2	3	4	5
Calcination time [h]	0.5	1.0	1.5	2.0	5.0
Resistance [kΩ]	33.3 ± 5.3	18.3 ± 2.6	6.6 ± 1.6	1.0 ± 0.2	0.2 ± 0.1

The results show that a longer dwell time at 450 °C during the calcination of the TiO₂ films leads to an increase of the grain size and consequently to an increase of the conductivity. Also the decrease of the amorphous areas in the films can have an influence on the improved conductivity. Our results are in good accordance with quantum mechanical calculations of polycrystalline metallic materials by Reiss et al.^[21]. They showed an exponential decrease of the calculated conductivity with respect to the number of grain boundaries per mean free path. Their calculations are in good agreement with an empirical model proposed by Vancea et al. ^[22, 23] which is based on experimental investigations of Cu, Al, Ag, Au, Ni and Pt films.

Sun et al.^[14] investigated the effect of the film thickness on the power conversion efficiency of TiO₂ blocking layers of organic solar cells. The TiO₂ layers were synthesized by spray pyrolysis at a temperature of 450 °C. Resistance analysis of their films revealed that charge transport is not limited even for 500 nm thick films but that the light intensity limits the device's performance. They found an optimal thickness of 100 nm for their investigated solar cells. In our work, this thickness could be reached with a spin coating speed of 1500 rpm. The conductivity seems not to be influenced by the film thickness but we found that it can be increased by the calcination time. We propose that a higher conductivity of the TiO₂ blocking layers should have a positive influence on the solar cell performance. This should be further investigated in different types of solar cells for example ETA, thin film or organic solar cells.

9.5 Summary and Conclusion

In conclusion, five different TiO₂ films were prepared with a sol-gel synthesis and deposited on FTO substrates by spin coating and calcinating with varying dwell times (0.5 h, 1 h, 1.5 h, 2 h and 5 h) at 450 °C. TEM investigations were realized focusing on the grain size, the crystal phase and adhesion to the FTO. Additionally, investigations on the influence of the spin coating speed on the film thickness were done. Bright field images reveal a thickness of 14-20 nm in the thinnest region for films prepared with a faster spin coating speed (3000 rpm) and 70-75 nm in the thinnest region for films prepared with a slower spin coating speed (1500 rpm). Furthermore these bright field images show a good adaption and adhesion of the TiO₂ films to the rough surface of the FTO substrate and that they have a flat surface. Electron diffraction experiments reveal TiO₂ in Anatase modification for all films. No reflections which indicate impurities were found. Additionally the electron diffraction pattern indicates polycrystallinity. The investigations of the HRTEM images show a random orientation without preference of the grains. The analysis of the HRTEM images regarding the grain size in the films with different dwell times yielded in an increase from 8.9 ± 0.5 nm for film 1 (0.5 h) to 13.1 ± 0.5 nm for film 5 (5 h). Also a decrease of amorphous areas between the grains with longer dwell times can be observed. Following these findings I-U curves were measured to investigate the influence of the grain size on the conductivity of the films. These measurements resulted in an increase of the conductivity for longer calcination times because of bigger grains and less amorphous areas. We propose that the longest calcination time of 5 h can have a positive effect for solar cell efficiencies where such films are applied as blocking layers.

9.6 Chapter references

- [1] Y. U. Ahn, E. J. Kim, H. T. Kim, S. H. Hahn, *Mater. Lett.* **2003**, *57*, 4660-4666.
- [2] H. Yu, S. Zhang, H. Zhao, G. Will, P. Liu, *Electrochim. Acta* **2009**, *54*, 1319-1324.
- [3] K.-I. Jang, E. Hong, J. H. Kim, *Korean J. Chem. Eng.* **2012**, *29*, 356-361.
- [4] F. Lenzmann, M. Nanu, O. Kijatkina, A. Belaidi, *Thin Solid Films* **2004**, *451-452*, 639-643.
- [5] A. Burke, S. Ito, H. Snaith, U. Bach, J. Kwiatkowski, M. Graetzel, *Nano Lett.* **2008**, *8*, 977-981.
- [6] T.-Y. Cho, S.-G. Yoon, S. S. Sekhon, M. G. Kang, C.-H. Han, *Bull. Korean Chem. Soc.* **2011**, *32*, 3629-3633.
- [7] A. Yildiz, S. B. Lisesivdin, M. Kasap, D. Mardare, *J. Non-Cryst. Solids* **2008**, *354*, 4944-4947.
- [8] J. Aarik, A. Aidla, A.-A. Kiisler, T. Uustare, V. Sammelselg, *Thin Solid Films* **1997**, *305*, 270-273.
- [9] P. J. Cameron, L. M. Peter, *J. Phys. Chem. B* **2003**, *107*, 14394-14400.
- [10] B. Peng, G. Jungmann, C. Jager, D. Haarer, H.-W. Schmidt, M. Thelakkat, *Coord. Chem. Rev.* **2004**, *248*, 1479-1489.
- [11] R. Mechiakh, S. N. Ben, R. Chtourou, R. Bensaha, *Appl. Surf. Sci.* **2010**, *257*, 670-676.
- [12] L. H. Chong, K. Mallik, G. C. H. de, R. Kersting, *J. Phys.: Condens. Matter* **2006**, *18*, 645-657.
- [13] C. Jiang, M. Y. Leung, W. L. Koh, Y. Li, *Thin Solid Films* **2011**, *519*, 7850-7854.
- [14] H. Sun, J. Weickert, H. C. Hesse, L. Schmidt-Mende, *Sol. Energy Mater. Sol. Cells* **2011**, *95*, 3450-3454.
- [15] L. Hu, T. Yoko, H. Kozuka, S. Sakka, *Thin Solid Films* **1992**, *219*, 18-23.
- [16] P. Chrysicopoulou, D. Davazoglou, C. Trapalis, G. Kordas, *Thin Solid Films* **1998**, *323*, 188-193.
- [17] C.-C. Chang, L.-P. Cheng, C.-Y. Lin, Y.-Y. Yu, *J. Sol-Gel Sci. Technol.* **2012**, *63*, 30-35.
- [18] Y. Hu, H. L. Tsai, C. L. Huang, *Mater. Sci. Eng., A* **2003**, *A344*, 209-214.
- [19] B. Mandlmeier, J. M. Szeifert, D. Fattakhova-Rohlfing, H. Amenitsch, T. Bein, *J. Am. Chem. Soc.* **2011**, *133*, 17274-17282.
- [20] A. Strecker, U. Salzberger, J. Mayer, *Prakt. Metallogr.* **1993**, *30*, 482-495.
- [21] G. Reiss, J. Vancea, H. Hoffmann, *Phys. Rev. Lett.* **1986**, *56*, 2100-2103.
- [22] J. Vancea, H. Hoffmann, K. Kastner, *Thin Solid Films* **1984**, *121*, 201-216.
- [23] J. Vancea, H. Hoffmann, *Thin Solid Films* **1982**, *92*, 219-225.

10 Conclusion and Outlook

The main focus of this thesis was the development of a simple, low cost and nontoxic synthesis method to prepare reproducible, nanostructured CuInS₂ thin films as absorber material for solar cell application. This was realized by a mild solvothermal synthesis route. The obtained films possess a high surface area and were characterized in terms of their morphology, their crystal structure as well as their chemical composition. For this purpose different analytical methods were used. Besides SEM for the investigation of the morphology, TEM based techniques found implementation, which are useful tools for in-depth analysis at the nanometer scale and important for the characterization of thin films and interfaces used in novel solar cells.

With a solvothermal synthesis route CuInS₂ thin films were prepared on a FTO substrate with different thicknesses and morphologies depending on the reaction parameters. The results in chapter 5 showed the influence of the concentration of the reaction solution and reaction time on the morphology of the films. Two different films, film A heated at 160 °C for 12 h synthesized with higher reaction concentration and film B, heated at 150 °C for 24 h synthesized with lower reaction concentration, were characterized. The synthesized films revealed a compact layer close to the FTO substrate and a structured area in the upper region of the films consisting of nanorods and out growing flakes. Therefore, a high surface area was obtained. Electron diffraction experiments and XRD investigations revealed that the films grow in the, for CuInS₂ typically, Roquesite crystal structure. Studies of the chemical composition using EDX in the TEM revealed that the films are Cu-rich in the compact area, which indicates a p-type semiconductor, and possess a stoichiometric composition in the upper, flaky area. With the higher reaction concentration, microspheres with a diameter of 1 – 3 μm exhibiting a flaky surface were obtained on top of the films.

Further systematic studies of the influence of the reaction concentration and reaction time on the film morphology and thickness were done and are summarized in chapter 6. It was found that the reaction concentration has a large impact on the film thickness but a low influence on the morphology. Films synthesized with a lower reactants concentration showed a maximum thickness of around 400 nm and films synthesized with higher reactants concentration around 900 nm. Whereas, the investigation of the

reaction time, which was varied between 0.5 h up to 24 h, revealed a high influence on the surface structure until 9 h. The structure transforms from small compact flakes to longer and more open flakes. No changes were found for reaction times exceeding 9 h. The investigations of the average chemical composition of the different synthesized films were done by EDX measurements in the SEM. A non stoichiometric Cu-rich or In-rich composition was found for the films synthesized at different reaction times shorter than 18 h. All crystallized in the dominant Roquesite structure of CuInS_2 . Investigations lead to the assumption that the accumulation of Cu_xS and In_2S_3 formed in the reaction solution is successive starting with a Cu_xS phase. In_2S_3 is reacting more slowly and is contributing later in the reaction. With this result it should be possible to adjust CuInS_2 films as p-type or n-type semiconductors. Further in-depth characterization in the TEM of the rods and flakes in the upper region of the films using HRTEM and FFT analysis showed that the rods grow in the hexagonal Wurtzite structure and the flakes in the tetragonal Chalcopyrite structure.

In chapter 7 the microspheres obtained by high reaction concentrations are characterized in detail. Here as well the influences of different reaction conditions were investigated. Three samples (sample 1, 12 h, 160 °C; sample 2, 18 h, 150 °C and sample 3, 24 h, 150 °C) were compared. In all samples different types of microspheres were found with a more compact structure (named microspheres A), and microspheres with a more open, flaky structure (named B). With a longer reaction time microspheres B dominate. ICP-AES measurements for sample 1 and 2 and EDX measurements in the SEM gave an average composition of Cu:In:S for sample 1 of 1:1:2, for sample 2 of 1.5:1:2.5 and for sample 3 of 1.3:1:2.2. Slicing of some of the microspheres in the FIB/SEM microscope to take a look inward, showed that the microspheres are more or less compact in the middle with a flaky shell. Characterization of a TEM lamella of the microspheres showed two different chemical compositions for microspheres B according to the different reaction times. Microspheres B1 obtained for shorter reaction times seem to be compact in the core with a stoichiometric composition and consisting of smaller crystals. Additionally, an In-rich shell was found. Microspheres B2 consist of larger crystals due to the longer reaction time and seem to be porous in the core. A Cu-rich composition in the core, followed by a compact stoichiometric area and also In-rich areas close to the flaky structure was found. The obtained flakes on the shell have a

nearly stoichiometric composition in both cases. XRD and electron diffraction patterns showed, beside CuInS_2 , also reflections from CuS and In_2S_3 . A growth mechanism could be proposed out of these results. Because of the fact, that CuInS_2 is a promising absorber material for solar cells, the microspheres could find application as a paste, which can be deposited on a substrate. With this method a thin film possessing of a high surface area, fillable with a suitable organic or inorganic electron conductor could be obtained to prepare a solar cell.

Aiming at a more non toxic synthesis route, the so far used toxic sulfur source thioacetamide was replaced by the non toxic amino acid L-cysteine. In chapter 8, the in this way successful synthesizes CuInS_2 thin films are presented. Three films, A, B and C synthesized with different concentrations of reactants, showing different morphologies, film thicknesses and structures were characterized. It was found that with the concentration of the reagents the film growth can be strongly modified. With TEM investigations, a mixed structure of a polycrystalline compact layer and plates in the case of film B and rods in the case of film C were observed. All films grow with a stoichiometric composition. These results were obtained by EDX measurements in the SEM and in the STEM mode in the TEM. Electron diffraction experiments and XRD measurements revealed that the films grow in the Roquesite crystal structure. Furthermore it is shown that L-cysteine acts as a reducing species and is sufficient to reduce Cu^{2+} from the used CuSO_4 in aqueous solution to Cu^+ to induce the formation of CuInS_2 . Moreover, all three films A, B and C showed significant absorption over the whole visible spectrum. Therefore the films are viewed as possible candidates for thin absorber layers in solar cell designs. However, a thickness gradient of the films was observed by eye. This means that the films appeared darker at the lower end and brighter on the other end. During this study, variation of the temperature, the reaction time and the positioning of the substrate in the autoclave did not influence the homogeneity, morphology and thickness of the films and are therefore most likely not responsible for the observed thickness gradient. Further efforts were done to obtain homogeneous films. First successes were achieved by using FTO, coated with a thin tungsten oxide film, which can be used as blocking layer in solar cells. It seems that the films synthesized with L-cysteine as sulfur source preferred a more flat surface as the one of WO_3 compared to the rough surface of the FTO. These results are not shown in this thesis and should be characterize in more detail in future.

The synthesized CuInS₂ films generated in this thesis show a high potential for solar cell application because of their high surface area. These films can create a high amount of electron hole pairs when they are combined with a suitable semiconductor. Also the possibility to adjust the semiconductor's properties in p-type or n-type, the film thickness and the film morphology make this developed synthesis method a promising alternative to obtain CuInS₂ thin films. Thus, solar cells based on these CuInS₂ thin films should be developed in future, which may represent a highly attractive alternative solar cell compared to the common Si-based solar cell.

Another aim in this thesis was the optimization of sol-gel synthesized TiO₂ blocking layers used in solar cells regarding their conductivity. This could be reached by an increase of the calcination time of the films spin coated on FTO substrates. In chapter 9, different dwell times (0.5 h, 1 h, 1.5 h, 2 h and 5 h) at 450 °C were investigated. HRTEM measurements showed an increase of the grain size within the films and a decrease of amorphous areas between the grains with longer calcination times. Measurements of I-U curves revealed that the bigger grain size and the less amorphous areas in the film have a positive influence on the conductivity of the films. The best results were obtained with a dwell time of 5 h. We think that a longer calcination time of the sol-gel synthesized TiO₂ blocking layers can have a positive influence for the solar cell performance and this should be investigated in different already existing types of solar cells for example ETA, thin films or organic solar cells in future.

11 Appendix

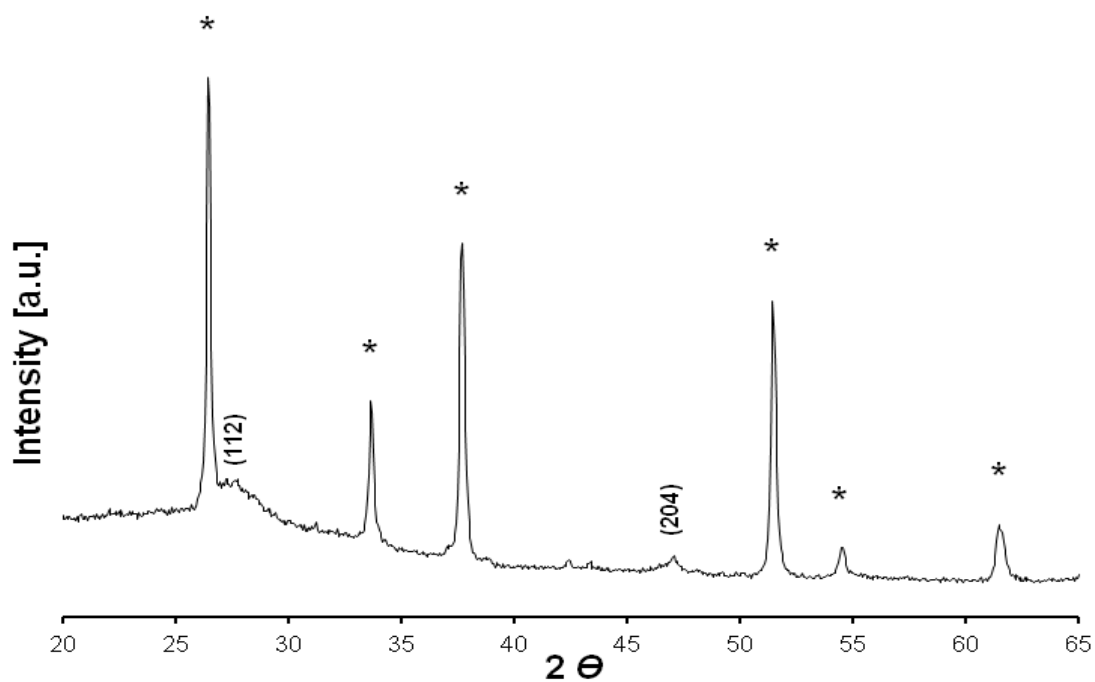


Figure 1A: XRD pattern of film 2B. Beside the reflections of FTO (marked with *) the reflections of CuInS_2 assigned to (110) and (204) are marked.

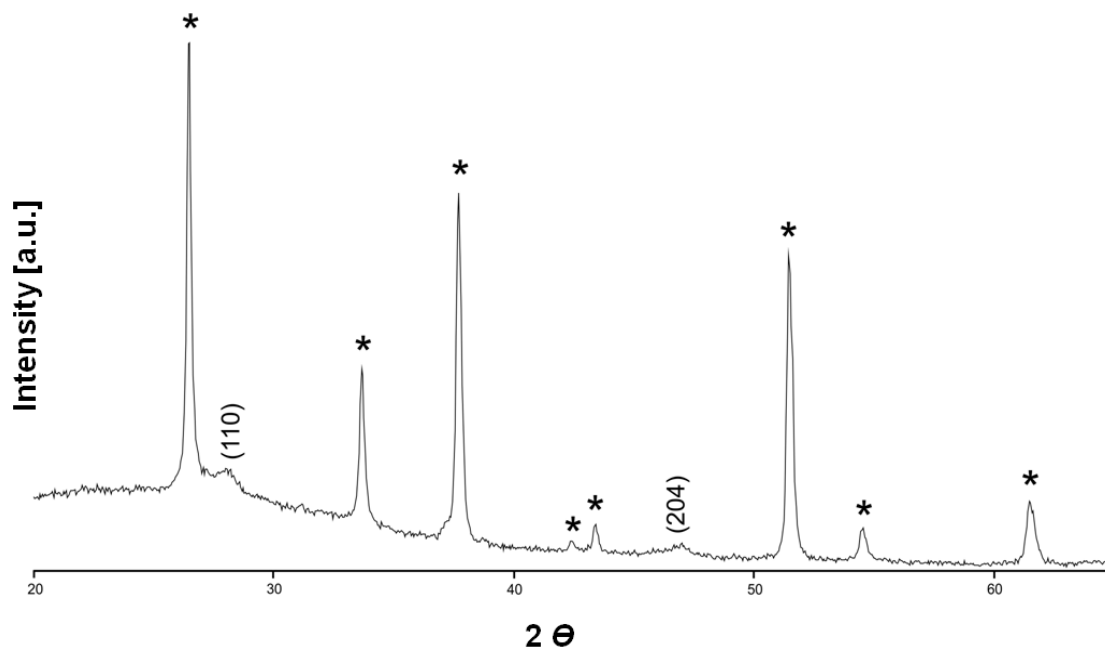


Figure 2A: XRD pattern of film 3A. Beside the reflections of FTO (marked with *) the reflections of CuInS_2 assigned to (110) and (204) are marked.

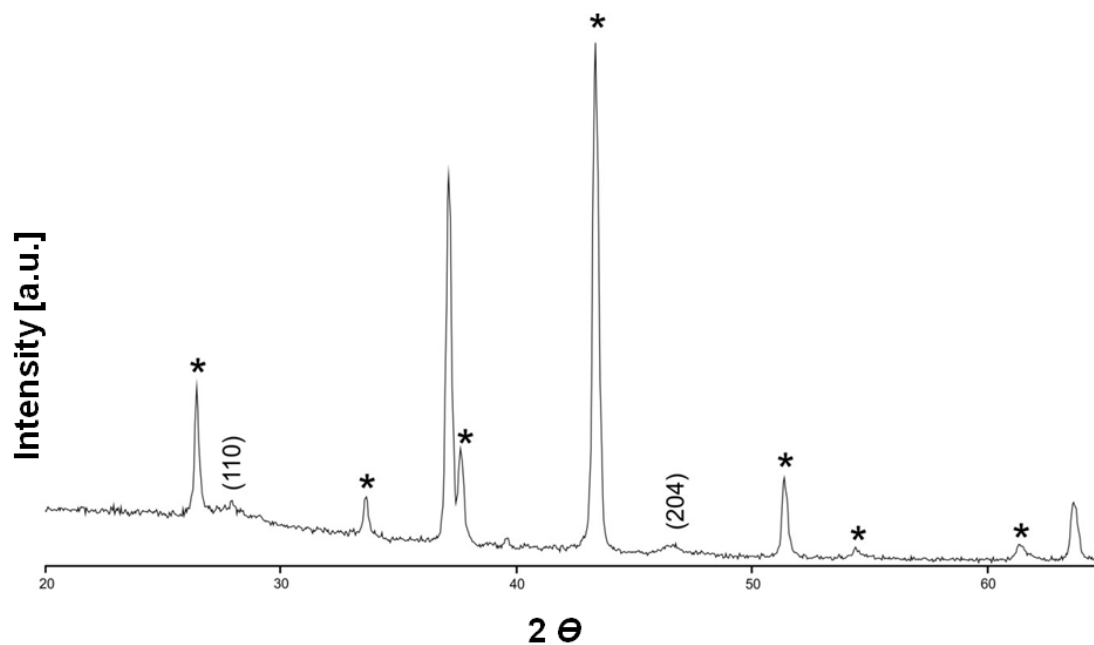


Figure A3: XRD pattern of film 5B. Beside the reflections of FTO (marked with *) the reflections of CuInS_2 assigned to (110) and (204) are marked.

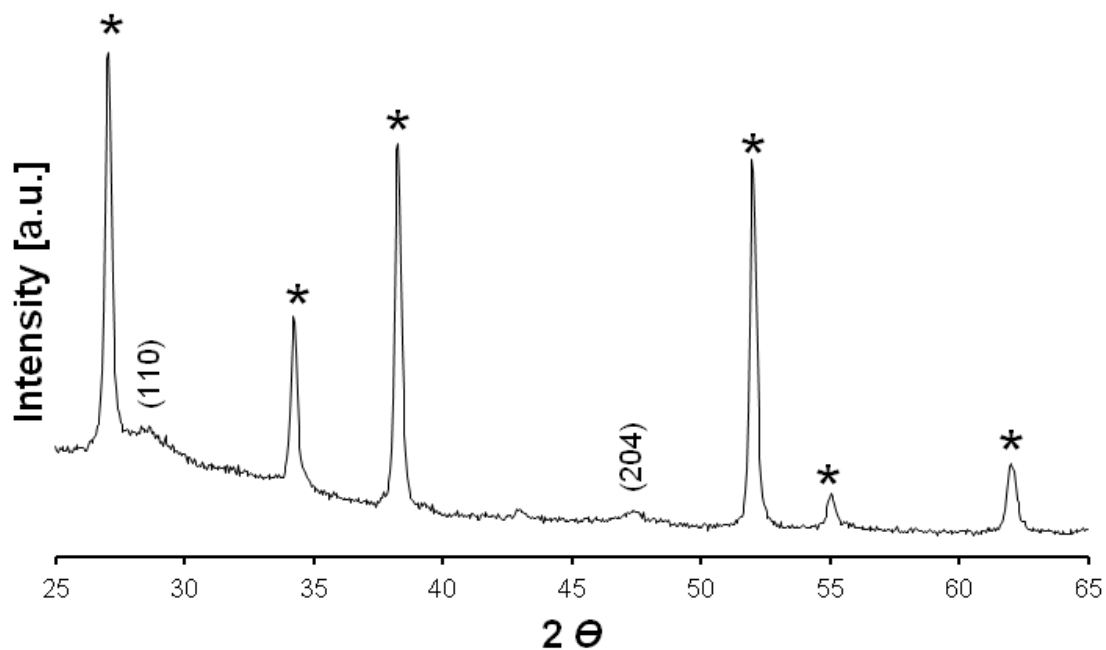


Figure 4A: XRD pattern of film 6A. Beside the reflections of FTO (marked with *) the reflections of CuInS_2 assigned to (110) and (204) are marked.

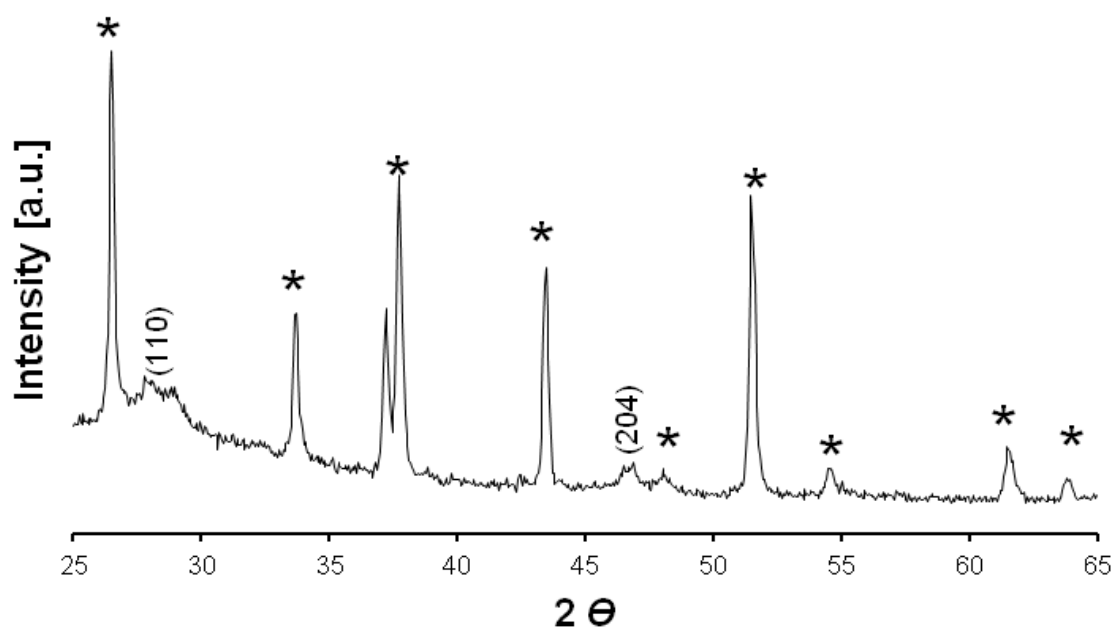


Figure 5A: XRD pattern of film 6B. Beside the reflections of FTO (marked with *) the reflections of CuInS_2 assigned to (110) and (204) are marked.

12 Curriculum Vitae

Personal Information

Name: Angela Wochnik
E-Mail: angela.wochnik@cup.uni-muenchen.de
Nationality: German

University Education

2009-untill now PhD study: Physical Chemistry at Ludwig Maximilians University Munich
2007-2009 Studies of Chemistry and Biochemistry at Ludwig Maximilians University Munich, graduation: Master of Science,
2002-2007 Studies of Chemistry and Biochemistry at Ludwig Maximilians University Munich, graduation: Bachelor of Science

Practical Courses

2009 Master theses at Siemens Munich, Supervisor: Dr. R. Karmazin, Prof. C. Scheu, topic: The thermal resistance in the composite of glass ceramics and cooling elements
2007 Bachelor theses at LMU, Prof. P. Klüfers, topic: Synthesis and characterization of "3+2" rhenium complexes
Practical course at LMU, Prof. B. Weber, topic: Synthesis of polymeric conductors
Practical course at Voit Paper Ravensburg, topic: Analysis of the impact of dispersing agents onto the paper fiber loading with bulking agents

School education and professional qualification

1998-2001 Advanced vocational Extension School, graduation: general qualification for university entrance (Abitur)
1996-1998 Permanent position as photo lab technician at CEWE color in Germering
1994-1996 Vocational education as photo lab technician at CEWE color in Germering
1989-1994 Secondary school in Germering, graduation: certificate of secondary education
1985-1989 Primary school in Germering

ADDITIONAL SKILLS

Since 2009	Experiments in chemical synthesis Autonomous working at the Transmission Electron Microscope (TEM), conventional TEM, electron diffraction, high resolution TEM, HAADF imaging, Energy Electron Loss Spectroscopy (EELS), TEM sample preparation Energy-dispersive X-ray Spectroscopy (EDX), Autonomous working at a Scanning Electron Microscope (SEM)
Since 2009	Training and supervising of Bachelor- and Diploma students. Supervising of practical courses in inorganic and physical chemistry
Languages	German, native speaker English, good in spoken and written French, basic knowledge
EDV	Microsoft Office

13 List of Publications and Presentations

13.1 Publications

Journals

1. Angela S. Wochnik, Christoph Heinzl, Florian Auras, Thomas Bein, Christina Scheu., Synthesis and Characterization of CuInS₂ thin film structures. *Journal of Material Science* **2011**, 47 (4), 1669-1676.
2. Angela S. Wochnik, Anna Frank, Christoph Heinzl, Jonas Häusler, Julian Schneider, Ramona Hoffmann, Sonja Matich, Christina Scheu. Investigation of the growth of CuInS₂ microspheres. *To be submitted*.
3. Angela S. Wochnik, Anna Frank, Thomas Bein and Christina Scheu. L-cysteine assisted growth of CuInS₂ films. *To be submitted*.
4. Melari Davies, Angela Wochnik, Florian Feil, Christophe Jung, Christoph Braeuchle, Christina Scheu, Jens Michaelis. Synchronous emission from nanometric silver particles through plasmonic coupling on silver nanowires. *ACS Nano* **2012**, 6 (7), 6049-6057.

Conference Proceedings

1. Angela Wochnik, Dajana Durach, Christoph Heinzl, Florian Auras, Thomas Bein and Christina Scheu. Electron Microscopy Characterization of TiO₂ and CuInS₂ used in Solar Cells. *Microscopy Conference MC 2011, Kiel, Germany, 28.08.-02.09.2011, Materials Science, M1: Materials for Energy Technology, M1.P510 (CD) 2011*.
2. Ramona Hoffmann, Angela Wochnik, Sonja Matich, Alexander Müller, Erika Griesshaber, Jeremy R. Young, Hartmut Schulz, Michal Kučera, Christina Scheu and Wolfgang.W. Schmahl . TEM Investigations of the Beam Sensitive CaCO₃ Shell of *Emiliana huxleyi*. *Microscopy Conference MC 2011, Kiel, Germany, 28.08 - 02.09.2011, Life sciences, L7: Zoomorphology, L7.P365 (CD) 2011*.

3. Angela Wochnik, Christoph Heinzl, Anna Frank, Jonas Häusler, Ramona Hoffmann, Sonja Matich, Christina Scheu. TEM investigation of the growth of CuInS₂ nanospheres. *15th European Microscopy Congress EMC 2012, Manchester, England, 16.09.-21.09.2012, Towards Sustainable Energy and Environmental Protection, PS1.8 (CD) 2012.*

4. Ramona Hoffmann, Angela Wochnik, Sophia Betzler, Sonja Matich, Erika Griesshaber, Hartmut Schulz, Michal Kucera, Jeremy R. Young, Christina Scheu, Wolfgang W Schmahl. Investigation of the R- and V-unit in the abundant coccolithophore species *Emiliana huxleyi* - an electron diffraction study. *15th European Microscopy Congress EMC 2012, Manchester, England, 16.09.-21.09.2012, Electron Diffraction and crystallography, PS2.6 (CD) 2012.*

13.2 Oral Presentations

1. Angela Wochnik, Christoph Heinzl, Florian Auras, Thomas Bein and Christina Scheu. Electron microscopy characterization of CuInS₂ used in solar cells. *E-MRS spring meeting, Nice, France, 09.-13.05.2011.*

2. Angela Wochnik, Nanoflowers - An Electron Microscopy Characterization, *CENS student's seminar, Munich, Germany, 2011.*

13.3 Poster Presentations

1. Angela Wochnik, Mihaela Nedelcu, Florian Auras, Thomas Bein and Christina Scheu. Microscopic characterization of interfaces in solar cells. *MACAN winter meeting, Berlin, Germany, 14.11. - 17.11.2009.*
2. Angela Wochnik, Mihaela Nedelcu, Florian Auras, Thomas Bein and Christina Scheu. TEM characterization of nano-morphologies in solid state solar cells. *NIM and CENS summer school, Venice, Italy, 19.09. – 25.09.2010.*
3. Angela Wochnik, Christoph Heinzl, Anna Frank, Ramona Hoffmann, Florian Auras, Thomas Bein and Christina Scheu. Synthesis and electron microscopy characterization of CuInS₂ films for photovoltaic application. *NIM Graduate Program, Summer Retreat, Aschau im Chiemgau, Germany, 27.07. - 29.07.2011.*
4. Angela Wochnik, Christoph Heinzl, Anna Frank, Ramona Hoffmann, Florian Auras, Thomas Bein and Christina Scheu. Synthesis and electron microscopy characterization of CuInS₂ films for photovoltaic application. *Microscopy Conference, Kiel, Germany, 28.08. - 02.09.2011.*
5. Angela Wochnik, Christoph Heinzl, Dajana Durach, Mihaela Nedelcu, Florian Auras, Thomas Bein and Christina Scheu. TEM characterization of nano-morphologies in photovoltaics. *NIM winter meeting, Munich, Germany, 2011.*
6. Angela Wochnik, Christoph Heinzl, Anna Frank, Jonas Häusler, Florian Auras, Thomas Bein and Christina Scheu. CuInS₂ thin films for solar cell applications. *MRS Spring meeting, San Francisco, USA, 09.-13.04.2012.*
7. Angela Wochnik, Anna Frank, Christoph Heinzl, Jonas Häusler, Julian Schneider, Ramona Hoffmann, Sonja Matich, Christina Scheu. Investigation of the growth of CuInS₂ microspheres. *15th Electron microscopy conference, Manchester, England, 16.09 - 21.09.2012.*

Danksagung

Mein ganz besonderer Dank gebührt Prof. Christina Scheu für ihre herzliche Aufnahme in ihren Arbeitskreis und für die ausgesprochen tolle Betreuung während meiner Promotion. Durch ihre Geduld, vielen Anregungen und zahlreichen Tipps hat sie mich stets bei der Erstellung meiner Arbeit unterstützt. Durch sie hatte ich die Möglichkeit einen tiefen Einblick in das interessante Gebiet der Elektronenmikroskopie zu bekommen und ein sehr spannendes Forschungsthema zu bearbeiten.

Des Weiteren möchte ich Herrn Prof. Thomas Bein für die nette und hilfsbereite Zweitbetreuung meiner Arbeit danken. Durch seine Unterstützung konnte ich viele neue Ideen in meiner Arbeit umsetzen. Vielen Dank für die erfolgreiche Zusammenarbeit.

Dr. Markus Döblinger möchte ich sehr herzlich für seine Einweisung ins TEM danken. Vielen Dank für die Zeit und Geduld die dafür nötig war und die zahlreichen guten Tipps die sehr zum Erfolg meiner Arbeit beigetragen haben.

Steffen Schmidt möchte ich für die tollen REM Bilder danken. Tina Reuter für die vielen X-ray Messungen. Dem restlichen Arbeitskreis Bein möchte ich für eine angenehme Laboratmosphäre bedanken. Mein ganz besondere Dank gilt Regina Huber für ihre stets offene Tür bei den Verwaltungsangelegenheiten und ihre Hilfe bei den organisatorischen Dingen.

Des Weiteren möchte ich meinen Kollegen im Arbeitskreis danken. Nicht nur für ein Arbeitsklima das seinesgleichen sucht, sondern auch für die Unterstützung in allen Bereichen. Christoph Heinzl möchte ich, neben der frischen morgendlichen Prise und den aufschlussreichen morgendlichen Gesprächen, die den Arbeitstag schon sehr locker starten ließen, für seine Hilfe während seiner Masterarbeit danken, die einen großen Beitrag zum Erfolg meiner Arbeit erbracht hat. Sophia Betzler, Andreas Wisnet und Sriram Venkatesan möchte ich neben einem angenehmen Arbeitsumfeld im Büro, für ihre zahlreiche Hilfe und Unterstützung, sowie für ein stets offenes Ohr in allen Angelegenheiten danken. Bei Teresa Dennenwaldt und Ramona Hoffmann möchte ich mich ganz herzlich für ihre moralische Unterstützung bedanken die mir sehr geholfen hat wenn es mal etwas schwieriger wurde. Euch beiden auch Danke für die tolle Zeit auf Reisen und danke liebe Ramona für die Lamellen und die Untersuchungen meiner

Proben an der FIB. Alexander Müller, der mir durch seine Hilfe am Ende meiner Arbeit eine Menge Stress erspart hat, möchte ich ganz herzlich danken. Vielen Dank lieber Alex für die Kristallstrukturen und die Zeit die du für mich geopfert hast. Meinen Praktikanten: Andrea Hermann, Jonas Häusler, Julian Schneider, Maja Hermann, Dajana Durach, Ruth Boller möchte ich für ihre tolle Arbeit und Hilfe danken. Einen ganz besonderen Dank geht an Anna Frank, die während ihres Praktikums hervorragende Arbeit geleistet hat. Danke liebe Anna auch für deine Hilfe und Unterstützung mit Word und beim Paper schreiben.

Matthias Handloser möchte ich für seine zahlreichen und für meine Arbeit sehr hilfreichen Messungen sowie die aufbauenden Sprüche und die kurzen Pausen danken. Johanna Schulten möchte ich danken für die seelische Unterstützung und die willkommenen Auszeiten während meiner gesamten Studienzzeit.

Besonders möchte ich meinen Eltern und dem Rest meiner Familie für ihre unerschöpfliche moralische Unterstützung und Ermutigungen danken.

Der größte Dank geht an meinen Freund Bernd Gassner der mich während des Studiums und besonders während der Promotion aushielt. Danke für die Geduld die du für mich aufgebracht hast und das du mich immer wieder ermutigt hast weiter zu machen.